SPECIAL ISSUE

ASTROPHYSICAL SPECTROSCOPY
- A&M DATA - MODELLING

Based on lectures presented at
International Meeting on Data for Atomic and Molecular Processes
in Plasmas: Advances in Standards and Modelling

Palić, Serbia, November 12-15, 2024

CONTRIBUTIONS
OF THE ASTRONOMICAL OBSERVATORY
SKALNATÉ PLESO

● VOLUME LV ●

Number 2

February 2025

Editorial Board

CONTENTS

3

The Contributions of the Astronomical Observatory Skalnaté Pleso
are available in a full version
in the frame of ADS Abstract Service
and can be downloaded in a usual way from the URL address:

''http://adsabs.harvard.edu/article_service.html''

as well as from the web-site of
the Astronomical Institute of the Slovak Academy of Sciences
on the URL address:

''http://www.astro.sk/caosp/''

The journal is covered/indexed by:

Web of Science (WoS)

WoS Core Collection: Science Citation Index Expanded

SCOPUS

Index Copernicus International

SPECIAL ISSUE
Astrophysical Spectroscopy
- A&M DATA - Modelling

Edited by

Vladimir A. Srećković, Milan S. Dimitrijević, Aleksandra Kolarski,
Mihailo R. Savić, Nikola B. Veselinović

Based on lectures presented at

International Meeting on Data for
Atomic and Molecular Processes in Plasmas:
Advances in Standards and Modelling

November 12 – 15, 2024, Palić, Serbia

Institute of Physics Belgrade, University of Belgrade

https://asspectro.ipb.ac.rs/2024/

LIST OF PARTICIPANTS

Arnaut, Filip	Institute of Physics Belgrade, Pregrevica 118, 11080 Belgrade, Serbia
Banjanac, Radomir M.	Institute of Physics Belgrade, Pregrevica 118, 11080 Belgrade, Serbia
Bednár, Peter	Technical University of Košice, Faculty of Electrical Engineering and Informatics, Department of Cybernetics and Artificial Intelligence, Letná 1/9, 042 00 Košice, Slovakia
Biagi, Pier F.	Department of Physics, University of Bari, Via Amendola 173, 70125 Bari, Italy
Borka Jovanović, Vesna	Department of Theoretical Physics and Condensed Matter Physics (020), Vinča Institute of Nuclear Sciences - National Institute of the Republic of Serbia
Borka, Duško	Department of Theoretical Physics and Condensed Matter Physics (020), Vinča Institute of Nuclear Sciences - National Institute of the Republic of Serbia
Bošnjaković, Danko V.	Institute of Physics Belgrade, Pregrevica 118, 11080 Belgrade, Serbia
Boudjada, Mohammed Y.	Department of Physics, University of Bari, Via Amendola 173, 70125 Bari, Italy
Bozek, John	Synchrotron SOLEIL, 91190 Saint-Aubin, France
Butka, Peter	Technical University of Košice, Faculty of Electrical Engineering and Informatics, Department of Cybernetics and Artificial Intelligence, Letná 1/9, 042 00 Košice, Slovakia
Capozziello, Salvatore	Scuola Superiore Meridionale, Largo S. Marcellino 10, I-80138, Napoli, Italy
Christova, Magdalena D.	Department of Applied Physics, Technical University of Sofia, 1000 Sofia, Bulgaria
Delibašić Marković, Hristina S.	Faculty of Science, University of Kragujevac, Radoja Domanovića 12, 34000 Kragujevac, Serbia
Dimitrijević, Milan S.	Astronomical Observatory, Volgina 7, 11060 Belgrade, Serbia
Djuissi, E.	Laboratoire Ondes & Milieux Complexes CNRS-UMR-6294, Université du Havre, 76058 Le Havre, France
Dragić, Aleksandar L.	Institute of Physics Belgrade, Pregrevica 118, 11080 Belgrade, Serbia
Dujko, Saša	Institute of Physics Belgrade, Pregrevica 118, 11080 Belgrade, Serbia
Eichelberger, Hans	Space Research Institute, Austrian Academy of Sciences, Schmiedlstrasse 6, 8042 Graz, Austria

Iacob, F.	Physics Faculty, West University of Timişoara, Timişoara, Romania
Ivanović, S. Đ.	Institute of Physics Belgrade, Pregrevica 118, 11080 Belgrade, Serbia
Jevremović, Sreten	Scientific Society Isaac Newton Belgrade, Volgina 7, Belgrade, Republic of Serbia
Joković, Dejan R.	Institute of Physics Belgrade, Pregrevica 118, 11080 Belgrade, Serbia
Jovanović, Predrag	Astronomical Observatory, Volgina 7, 11060 Belgrade, Serbia
Knežević, David	Institute of Physics Belgrade, Pregrevica 118, 11080 Belgrade, Serbia
Kolarski, Aleksandra	Institute of Physics Belgrade, Pregrevica 118, 11080 Belgrade, Serbia
Kopyra, Janina	Faculty of Sciences, Siedlce University, 3 Maja 54, 08-110 Siedlce, Poland
Kounchev, Ognyan	Institute of Mathematics and Informatics, Bulgarian Academy of Sciences
Kovačević, Vesna V.	University of Belgrade – Faculty of Physics, Belgrade, Serbia
Krstić, Ivan B.	University of Belgrade – Faculty of Physics, Belgrade, Serbia
Kuraica, Milorad M.	University of Belgrade – Faculty of Physics, Belgrade, Serbia
Langović, Milica	Institute of Physics Belgrade, Pregrevica 118, 11080 Belgrade, Serbia
Maletić, Dimitrije M.	Institute of Physics Belgrade, Pregrevica 118, 11080 Belgrade, Serbia
Maljković, Jelena B.	Institute of Physics Belgrade, Pregrevica 118, 11080 Belgrade, Serbia
Marić, Dragana	Institute of Physics Belgrade, Pregrevica 118, 11080 Belgrade, Serbia
Marinković, Bratislav P.	Institute of Physics Belgrade, Pregrevica 118, 11080 Belgrade, Serbia
Marjanović, Jelena	Institute of Physics Belgrade, Pregrevica 118, 11080 Belgrade, Serbia
Mezei, J. Zs	Institute for Nuclear Research, Hungarian Academy of Sciences, H-4001 Debrecen, Hungary
Mijić, Zoran R.	Institute of Physics Belgrade, Pregrevica 118, 11080 Belgrade, Serbia
Milosavljevic, Aleksandar R.	Synchrotron SOLEIL, 91190 Saint-Aubin, France

Nico, Giovanni	Institute of Applied Mathematics, Italian National Research Council, Via Giovanni Amendola 122/I, 70126 Bari, Italy
Nicolas, Christophe	Synchrotron SOLEIL, 91190 Saint-Aubin, France
Nina, Aleksandra	Institute of Physics Belgrade, Pregrevica 118, 11080 Belgrade, Serbia
Obradović, Bratislav M.	University of Belgrade – Faculty of Physics, Belgrade, Serbia
Petrović, Ivan D.	Department in Kragujevac, Academy of Professional Studies Šumadija, Kosovska 8, Kragujevac, Serbia
Petrović, Srđan	Institute of Nuclear Sciences - National Institute of the Republic of Serbia, University of Belgrade, P.O. Box 522, 11001 Belgrade, Serbia
Petrović, Vladimir M.	Faculty of Science, University of Kragujevac, Radoja Domanovića 12, 34000 Kragujevac, Serbia
Petrović, Zoran Lj.	School of Engineering, Ulster University, Jordanstown, County Antrim BT37 0QB, United Kingdom
Pop, Nicolina	Department of Physical Foundations of Engineering, Politehnica University of Timisoara 2 Vasile Parvan Blvd, 300223 Timisoara, Romania
Popović, Luka Č.	Astronomical Observatory, Volgina 7, 11060 Belgrade, Serbia
Ranitović, Predrag	University of Belgrade – Faculty of Physics, Belgrade, Serbia
Robert, Emmanuel	Synchrotron SOLEIL, 91190 Saint-Aubin, France
Sakan, Nenad M.	Institute of Physics Belgrade, Pregrevica 118, 11080 Belgrade, Serbia
Sarnovský, Martin	Technical University of Košice, Faculty of Electrical Engineering and Informatics, Department of Cybernetics and Artificial Intelligence
Savić, Mihailo R.	Institute of Physics Belgrade, Pregrevica 118, 11080 Belgrade, Serbia
Schneider, Ioan F.	Laboratoire Aimé Cotton, CNRS, ENS Cachan and Univ. Paris-Sud, 91405 Orsay, France
Simeonov, Georgi	Institute of Mathematics and Informatics, Bulgarian Academy of Sciences
Simonović, Ilija B.	Institute of Physics Belgrade, Pregrevica 118, 11080 Belgrade, Serbia
Sretenović, Goran B.	University of Belgrade – Faculty of Physics, Belgrade, Serbia
Srećković, Vladimir	Institute of Physics Belgrade, Pregrevica 118, 11080 Belgrade, Serbia

Starčević, Nikola	Institute of Nuclear Sciences - National Institute of the Republic of Serbia, University of Belgrade, P.O. Box 522, 11001 Belgrade, Serbia
Tošić, Sanja	Institute of Physics Belgrade, Pregrevica 118, 11080 Belgrade, Serbia
Travar, Miloš	Institute of Physics Belgrade, Pregrevica 118, 11080 Belgrade, Serbia
Udovičić, Vladimir I.	Institute of Physics Belgrade, Pregrevica 118, 11080 Belgrade, Serbia
Uskoković, N.A.	Institute of Physics Belgrade, Pregrevica 118, 11080 Belgrade, Serbia
Veselinović, Nikola B.	Institute of Physics Belgrade, Pregrevica 118, 11080 Belgrade, Serbia
Vujčić, Veljko	Astronomical Observatory, Volgina 7, 11060 Belgrade, Serbia

PREFACE

This Special Issue on Astrophysical Spectroscopy: A&M DATA - Modelling contains selected papers from the International Meeting on Data for Atomic and Molecular Processes in Plasmas: Advances in Standards and Modelling. The conference was held from November 12 to 15, 2024, at a venue near Lake Palić, in northern Serbia. The meeting covered a wide range of topics, from fundamental studies to applications, bringing together scientists from the fields of physics, astro- and geophysics, who are engaged in various aspects of astrophysical spectroscopy, plasma physics, atomic and molecular data, databases, and Earth observation. The latest results were presented and discussed, spanning topics such as plasma physics, astrophysics, geophysics, astronomy, and related fields. The efficiency of theoretical analysis, synthesis, and modeling of various environments depends significantly on atomic data and their sources. For example, the modeling of stellar atmospheres and opacity calculations requires a vast amount of atomic data, especially since the chemical composition of a stellar atmosphere is not known a priori. Similarly, atomic data are crucial for Earth observation. Consequently, the development of databases containing atomic data, as well as advancements in astro-geoinformatics, plays an important role. This meeting provided an opportunity to address the above-mentioned aspects of spectroscopic research in plenary sessions, followed by collaborative work on special mini-projects designed to result in joint publications in international scientific journals. The conference was attended by 51 participants from 14 countries. Participants presented 7 invited lectures, 4 regular talks, 16 poster presentations, and engaged in six mini-sessions. This Special Issue contains 11 articles, covering the main themes of the conference. All papers in this issue have undergone rigorous peer review. Each submission was reviewed by at least two reviewers. The organizers would like to express their gratitude to the Ministry of Science, Technological Development, and Innovation of the Republic of Serbia for their support. We also thank the members of the scientific and local organizing committees for their assistance in planning and running the conference. The editors are particularly grateful to the reviewers for their efforts in evaluating all contributions. Finally, we acknowledge the support of the journal Contributions of the Astronomical Observatory Skalnaté Pleso. Materials from this and previous meetings, including the program, presentations, proceedings, and photos, are available at https://asspectro.ipb.ac.rs/2024/.

D.Sc. V. A. Srećković, D.Sc. M. S. Dimitrijevic, D.Sc. A. Kolarski,
D.Sc. M. R. Savić & D.Sc. N. B. Veselinović
the editors

Standardization framework of ionospheric Very Low Frequency (VLF) signal amplitude classes for machine learning-based anomaly detection: from calm ionospheric conditions to solar activity-induced dynamics

F. Arnaut[ID]**, A. Kolarski**[ID]**, V.A. Srećković**[ID]**, M. Langović**[ID] **and**
S. Jevremović[ID]

Institute of Physics Belgrade, University of Belgrade, Pregrevica 118, 11080
Belgrade, Serbia (E-mail: filip.arnaut@ipb.ac.rs)

Abstract. Machine learning (ML) techniques are extensively employed in the domain of near-Earth physics. An application of ML techniques is the anomaly detection of Very Low Frequency (VLF) ionospheric amplitude data. Prior research focused on the binary classification task, yielding promising results, and the subsequent exploration involves the multi-label classification of a broader spectrum of VLF amplitude signal features. This research paper introduces a standardization framework for labeling multi-class VLF amplitude features, including normal (daytime) signals, solar flare effects, nighttime signals, instrumental errors, and outlier data points. The primary aim of this standardization framework is to define all main VLF amplitude features, specify the conditions under which each VLF amplitude feature can be classified, and outline future initiatives for the development of additional tools to facilitate the labeling process. Future research will focus on developing supplementary tools and software packages for this purpose, with the ultimate objective of establishing a streamlined process from the Worldwide Archive of Low-Frequency Data and Observations (WALDO) database to labeled data and subsequently to ML models.

Key words: Ionosphere – D-region – solar flares – near-Earth physics – space weather

1. Introduction

The classification, notably the detection of various ionospheric Very Low Frequency (VLF) 3-30 kHz signal features, has been the subject of prior research (Arnaut et al., 2023, 2024a,b). The primary aim of the aforementioned research was to establish a data-driven methodology for the automatic detection of various ionospheric VLF signal variations. For those objectives, machine learning

(ML) techniques were the most appropriate. The utilization of ML techniques in near-Earth physics, including the classification of radar returns (Dhande & Dandekar, 2011; Oo, 2018; Ameer Basha et al., 2020; Adhikari et al., 2020), lightning signals (Wang et al., 2020), and auroral images (Shang et al., 2023; Lian et al., 2023), is extensively demonstrated. The prior work on anomaly detection on VLF amplitude signals pertained to a binary ML problem involving two classes: the normal data class, representing the undisturbed VLF signal, and the anomalous data class, encompassing various signal disturbances such as noise, instrumental errors, solar flare effects, nighttime signals, and others.

As the continuation of previously conducted research, the development of a multi-label methodology was proposed wherein each of the previously mentioned VLF signal features would operate independently of one group, unlike the binary classification conducted earlier. This methodology presents several advantages and disadvantages; notably, supervised ML techniques rely on a pre-classified training dataset, necessitating that a researcher perform the classification for model training. Conversely, the advantage lies in the potential creation of a fully automated method for detecting various VLF signal features, which could be developed into a near real-time system for monitoring VLF signal changes.

The quality of the training dataset is crucial for the successful development of supervised ML models, as these methods are data-driven. The largest repository of freely available narrowband VLF datasets is the Worldwide Archive of Low-Frequency Data and Observations (WALDO), which includes open datasets for specific time intervals and VLF transmitter-receiver pairs from 2005 to 2017. This extensive repository suffices for the successful development of the previously presented methodology (Arnaut et al., 2023, 2024a,b); however, for the initial attempt at transitioning from a binary to a multi-class ML problem, the previously employed dataset is adequate.

The primary aim of this research paper is to provide an overview and standardization of various VLF signal features, as data quality is vital; accurate data labeling is the initial step in ensuring satisfactory data quality. The research paper will propose various classifications of ionospheric VLF signal features, potentially covering main VLF signal variations. It will also aim to provide clear definitions for each of the classed of VLF signals, grounded in prior experiences with the binary ML methodology for VLF signal anomaly detection, with the objective of enabling a broader audience to label VLF amplitudes in a standardized way.

The standardization framework and future studies on the topic are important for the interdisciplinary domains of ML and ionospheric physics, and they also aid other researchers in understanding the Sun-Earth connection. The established methodology for automatic anomaly detection of VLF amplitude signals may be advantageous to researchers in various interdisciplinary fields related to the effects of solar flares on the environment, human health, and other domains.

2. Framework for VLF signal class standardization

Figure 1 presents the framework for classifying VLF signal changes. The proposed standardization framework delineates five distinct categories: normal (daytime) signal, nighttime signal, solar flare effects, instrumental error, and outlier data point(s). A comprehensive discussion and examples of each case will be provided for each of the main five classes in the subsequent sections of the paper.
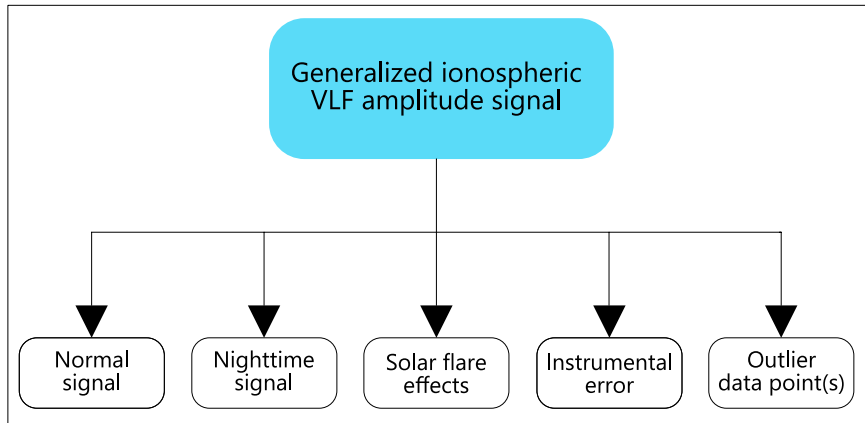
Figure 1. The proposed ionospheric VLF signal multi-label classification framework.

2.1. Normal daytime ionospheric VLF signal

The first and consequently simplest labeling category is the normal i.e., daytime ionospheric VLF signal, which consists of the undisturbed daytime signal. This signal is unaffected by extraterrestrial phenomena, such as solar flares, and is free from instrumental errors or anomalous data points. Figure 2 illustrates a signal in which the daytime readings are largely unaffected by extraterrestrial influences or the previously mentioned factors. The signal exhibits stability after the transitions from nighttime to daytime signal, which corresponds to sunrise, and from daytime to nighttime signal, which corresponds to sunset, stabilizing around 12 o'clock and fluctuating at its characteristic strength, which in presented case is around approximately 25 dB.

Figure 2 depicts an instance in which, despite significant fluctuations in the X-ray parameter, the variation in VLF amplitude is negligible. A decision must be made regarding the classification of these data points as belonging to the solar flare category. In the context of ML classification, such labeling may re-

sult in complications during modeling, as the model could erroneously classify undisturbed VLF amplitude values as solar flares, despite the absence of amplitude disturbances. The relatively undisturbed VLF amplitude signal, despite significant X-ray fluctuations, is not categorized under other classifications but is instead designated as part of the normal data class.
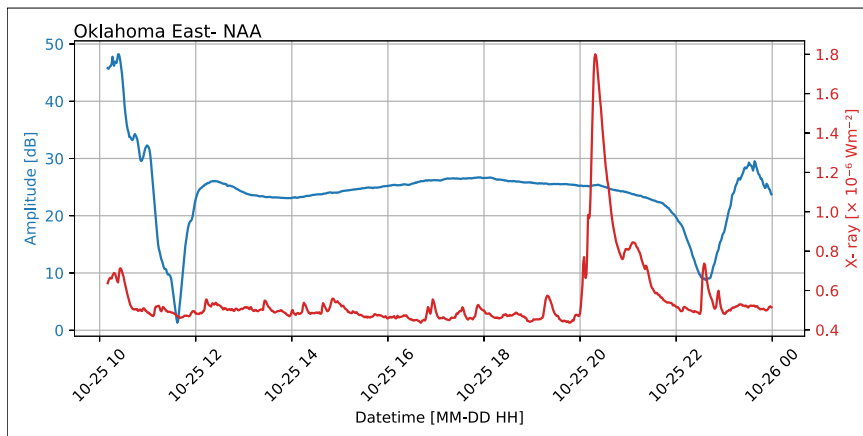
Figure 2. An example of a relatively undisturbed daytime signal on the Oklahoma East- NAA VLF amplitude signal; Blue line- VLF amplitude; Red line- X-ray irradiance data.

2.2. Nighttime signal

The nighttime signal in VLF amplitude appears as significantly elevated values in the VLF amplitude (Figure 3). When datasets correspond to multiple dates, a periodic component of the nighttime signal can be readily visually distinguished due to the characteristic that the nighttime signal exhibits greater values than the daytime signal. The nighttime signal is one of the more easily distinguishable VLF amplitude signal characteristics especially when there are more nighttime signals in a single data file.

The topic of discussion pertains to the appropriate initiation and completion points for labeling the nighttime VLF amplitude signal. Figure 3 illustrates two transitional periods: the transition from daytime to nighttime and the transition from nighttime to daytime (terminators). The terminators exhibit a unique characteristic wherein the transition from daytime to nighttime results in a signal reduction below daytime values, subsequently increasing to exceed daytime levels and stabilizing at a specific threshold. The transition from night to day is inverse, as the signal from the nighttime level decreases below the daytime

level before subsequently rising to the daytime level. The peak-to-peak value appears in both instances, and the labeling could split the peak-to-peak values for both transitional periods. Consequently, during the transition from day to night, the initial reduction of the peak-to-peak value would result in one half being classified as a daytime signal and the other half as a nighttime signal. The inverse is also applicable to the transition from nighttime to daytime.
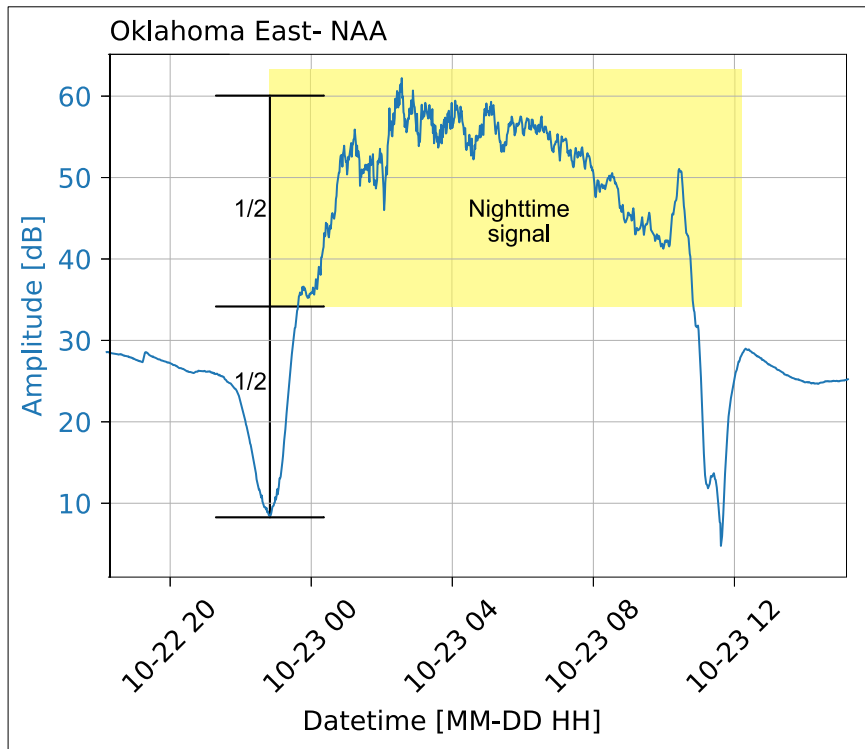
Figure 3. Example of the nighttime signal (yellow rectangle) and the transition of daytime-to-nighttime (marked by 1/2) and nighttime-to-daytime ionospheric VLF amplitude signal from the Oklahoma East- NAA transmitter- receiver pair; Blue line- VLF amplitude.

2.3. Solar flare effects

Solar flares are unique characteristics observable in the VLF amplitude signal. The solar flare effect is typically identifiable visually, characterized by a pronounced increase in the VLF amplitude signal, followed by a relatively gradual

return to pre-flare levels. Furthermore, plotting the X-ray irradiance data alongside the VLF amplitude facilitates a quite straightforward classification of solar flare effects on the VLF amplitude signal.

Figure 4 illustrates the Oklahoma East- NAA daytime signal featuring three distinct solar flare effects (purple rectangles) and a segment of the signal where the X-ray irradiance data suggests a solar flare; however, the VLF signal does not align with the expected increase in VLF amplitude (green rectangle). Labeling the pronounced solar flare effect is relatively straightforward when visual identification is combined with X-ray irradiance data; however, two questions emerge regarding the labeling process: when to initiate the labeling as solar flare effect data class and when to conclude it. For the standardization framework the solar flare class can initiate at the first data point that exhibits notable deviations from the preceding data point, where the overall morphology of the subsequent data points suggests a solar flare, in conjunction with the X-ray irradiance data. The conclusion of the solar flare classification can be determined when the data points revert to approximately pre-flare levels. Furthermore, it is important to acknowledge that the effects of solar flares are indistinguishable in nighttime VLF amplitude signals; thus, solar flare effects should only be identified in daytime signals.

Finally, the green rectangle illustrates a scenario in which the X-ray irradiance data exhibits a significant increase in values, whereas the VLF amplitude data remains unchanged. In the context of multi-label ML modeling, this should be considered a standard daytime signal, as no alterations are indicated in the VLF amplitude data despite a significant rise in the X-ray irradiance data. The primary aim of this standardization is to demonstrate to the model that not all increases in X-ray irradiance data correspond to an increase in VLF amplitude, indicating that the relationship between the two is not a one-to-one correlation. A similar situation can be seen on Figure 2 where the largest increase of X-ray irradiance does not result in an meaningful increase of VLF amplitude.

2.4. Instrumental errors

Instrumental errors in the VLF amplitude signal can manifest in various forms, but they are typically readily visually discernible. Figure 5a illustrates a scenario in which the VLF receiver fails to measure the VLF amplitude as either the transmitter or receiver was not functioning, resulting in the omission of observations. Typically, missing observations in the data file appear as observations lacking a numerical value; however, in Figure 5a, those observations are represented with a value of 0 (or any other constant value that is usually significantly lower than the real measured data values). If there is no measured real value, then the zero values would be absent, and only the signals preceding and succeeding them would be observable with a gap in the middle.

Figure 5b illustrates a scenario in which the signal exhibits erroneous VLF amplitude values, characterized by patterns of rapid increases and decreases in
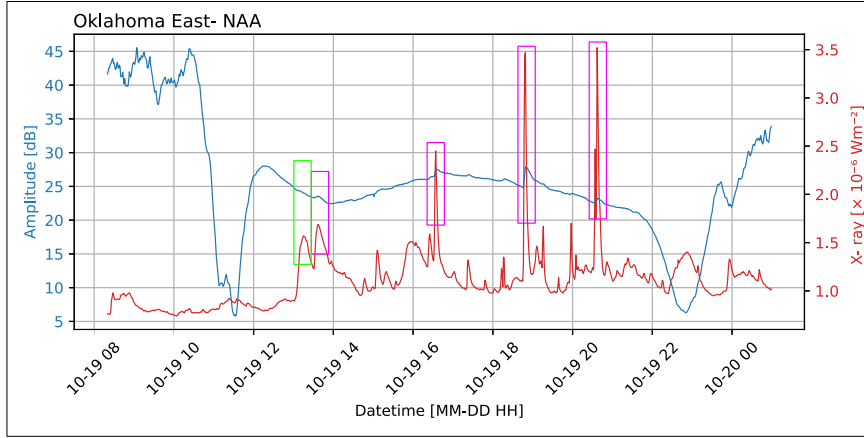
Figure 4. Example of the effects of solar flares on VLF amplitude signal variations and subsequent classification on the Oklahoma East- NAA signal; Blue line- VLF amplitude; Red line- X-ray irradiance data.

the measured values. In both instances, as well as analogous situations where a segment of the signal distinctly differs from the remainder, the signal in question may be classified as belonging to the instrumental error class. In the nighttime and solar flare classes, the topic of discussion pertained to the initiation and conclusion of the labeling process. However, in this instance, the question is clear: the initial data point that distinguishes itself from its predecessor and aligns with the visual pattern of instrumental error constitutes the first instrumental error data class, as does the final point.

2.5. Outlier data point(s)

Finally, the most uncommon data class in the VLF amplitude multi-label classifications consists of the outlier data points. Outlier data points appear to be distinctive data points that are markedly dissimilar from preceding and following data points. When analyzed alongside X-ray irradiance data, they exhibit no correlation, indicating there is no rationale for the elevated value. Figure 6 illustrates four instances in which the data points are notably dissimilar from preceding and subsequent VLF amplitude values and exhibit no correlation with X-ray irradiance data. Three of the values indicate that the outliers exhibit an increased value, while the fourth, as shown in Figure 6, demonstrates that the value can also decrease. The cause of the outlier data points remains unexplained; it may be related to internal instrument malfunctions or other factors, yet they necessitate their own data classification.
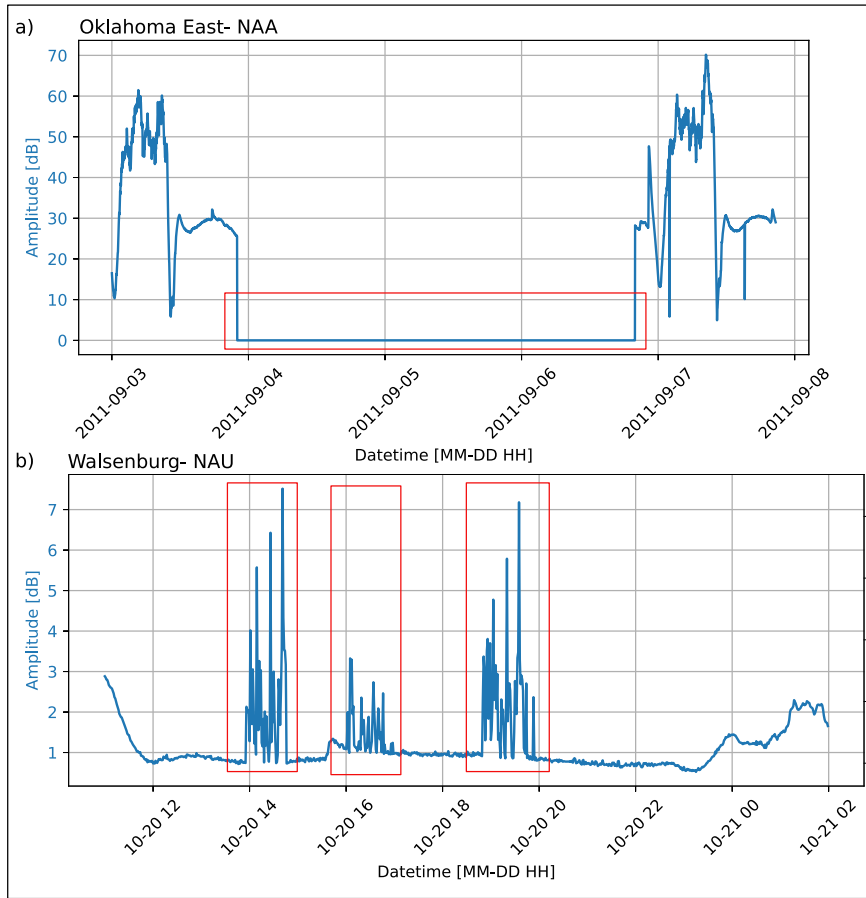
Figure 5. Types of instrumental errors on VLF amplitude signals; (a) Oklahoma East-NAA VLF amplitude signal; (b) Walsenburg- NAU VLF amplitude signal; Blue line-VLF amplitude.

3. Discussion and future prospectives

This paper addressed the standardization framework for labeling various VLF amplitude signal classes; however, the practical aspects also warrant discussion. The WALDO narrowband VLF data is provided in MATLAB data format, which is not the most versatile data format. Regarding the labeling process, rather than manually labeling each data point, our prior experience indicates that tools like TRAINSET (Geocene Inc.), a client-side, free, and open-source graphical tool for data labeling, sufficiently facilitate the laborious and time-
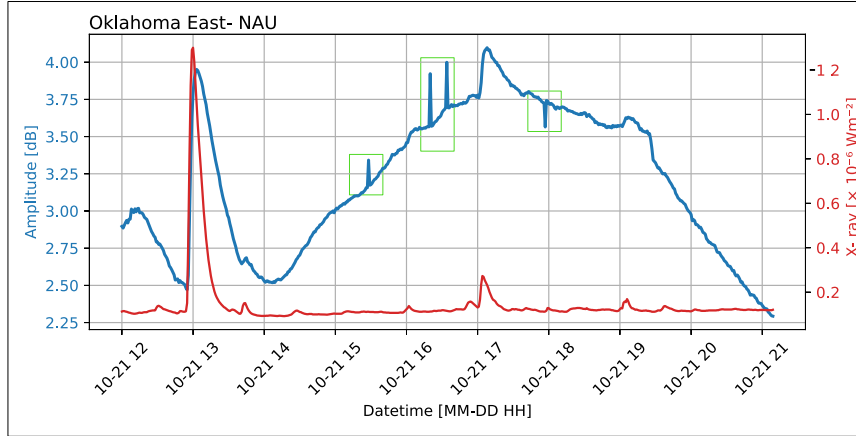
Figure 6. Examples of outlier data points on VLF amplitude signals from the Oklahoma East- NAU VLF amplitude signal; Blue line- VLF amplitude; Red line- X-ray irradiance data.

intensive task of data labeling. Given that TRAINSET requires data in a specific format and WALDO only supplied VLF amplitude and phase data, future research will focus on developing a free and open-source software package to convert MATLAB format into the designated TRAINSET format, incorporating X-ray irradiance data. Thus, data labeling will solely pertain to the labeling process itself, excluding additional issues arising from the manipulation of diverse data sources, formats, and others.

Furthermore, subsequent efforts aim to label an extensive amount of data from the WALDO database, commencing with the dataset utilized in Arnaut et al. (2023). Moreover, the multi-class ML classification can proceed with the objective of creating a model capable of autonomously identifying diverse VLF amplitude features as previously mentioned. The primary advantages of this initiative lie in data processing, as certain researchers aim to eliminate specific components of the VLF amplitude signal, including instrument errors and outliers, without manual intervention. Furthermore, if the model demonstrates adequate predictive power, a (near) real-time pipeline can be established to identify solar flare effects in (near) real-time or to address system malfunctions, among other issues. Further research is required, with the proposed standardization framework being the initial focus. The creation of specialized tools, along with the use of free and open-source resources, allows a diverse group of researchers to participate in the labeling process. Subsequent research will focus on the development of these tools, after which the data labeling process may commence.

4. Conclusion

This paper presents a standardization framework for multi-class labeling of VLF amplitude signals. The paper delineated five primary features of VLF amplitude signals, categorized as: normal (daytime) signal, nighttime signal, solar flare effects, instrumental errors, and outlier data points. A comprehensive explanation was provided for each of the five classes, including examples of the signal's appearance, the initiation of the labeling process, and its conclusion.

The practical aspect was also evaluated, including the most effective tools for this endeavor and future prospects for additional tools that will enhance the labelling process from the WALDO database to labeled data and ultimately to ML models. The primary objective of this model is to facilitate the automatic detection of all main VLF signal features, eliminating the necessity for manual labeling. Additionally, (near) real-time detection of VLF amplitude signal features is a potential outcome, although further research is required for successful implementation. The research area of automatic VLF amplitude signal features holds importance for various interdisciplinary fields related to the Sun-Earth connection, environmental studies, human health, and climate, among others and it will be the topic of more research in the future.

References

Adhikari, S., Thapa, S., & Shah, B. K., Oversampling based Classifiers for Categorization of Radar Returns from the Ionosphere. 2020, in *2020 International Conference on Electronics and Sustainable Communication Systems (ICESC), Coimbatore, India, 2-4 July 2020*

Ameer Basha, G., Lakshmana Gupta, K., & Ramakrishna, K. 2020, *Advances in Data Science and Management; Chapter: Expectation of Radar Returns from Ionosphere Using Decision Tree Technique* (Springer Nature: Singapore), DOI:10.1007/978-981-15-0978-0_20

Arnaut, F., Kolarski, A., & Srećković, V. A., Random Forest Classification and Ionospheric Response to Solar Flares: Analysis and Validation. 2023, *Universe*, **9**, DOI:10.3390/universe9100436

Arnaut, F., Kolarski, A., & Srećković, V. A., Comparative Analysis of Random Forest and XGBoost in Classifying Ionospheric Signal Disturbances During Solar Flares. 2024a, in *EGU General Assembly 2024, Vienna, Austria, 14–19 Apr 2024, EGU24-2046*

Arnaut, F., Kolarski, A., & Srećković, V. A., Machine Learning Classification Workflow and Datasets for Ionospheric VLF Data Exclusion. 2024b, *Data*, **9**, DOI:10.3390/data9010017

Dhande, J. D. & Dandekar, D. R., PSO Based SVM as an Optimal Classifier for Classification of Radar Returns from Ionosphere. 2011, *Int. J. Emerg. Technol.*, **2**, `DOI:-`

Lian, J., Liu, T., & Zhou, Y., Aurora Classification in All-Sky Images via CNN–Transformer. 2023, *Universe*, **9**, `DOI:10.3390/universe9050230`

Oo, A. N., Classification of Radar Returns from Ionosphere Using NB-Tree and CFS. 2018, *Int. J. Trend Sci. Res. Dev.*, **2**, `DOI:10.31142/ijtsrd17126`

Shang, Z., Yao, Z., Liu, J., et al., Automated Classification of Auroral Images with Deep Neural Networks. 2023, *Universe*, **9**, `DOI:10.3390/universe9020096`

Wang, J., Huang, Q., Ma, Q., et al., Classification of VLF/LF Lightning Signals Using Sensors and Deep Learning Methods. 2020, *Sensors*, **20**, `DOI:10.3390/s20041030`

The baryonic Tully-Fisher relation and Fundamental Plane in the light of $f(R)$ gravity

V. Borka Jovanović[1] , **D. Borka**[1] **and P. Jovanović**[2]

[1] *Department of Theoretical Physics and Condensed Matter Physics (020), Vinča Institute of Nuclear Sciences - National Institute of the Republic of Serbia, University of Belgrade, P.O. Box 522, 11001 Belgrade, Serbia (E-mail: vborka@vinca.rs, dusborka@vinca.rs)*

[2] *Astronomical Observatory, Volgina 7, P.O. Box 74, 11060 Belgrade, Serbia (E-mail: pjovanovic@aob.rs)*

Abstract. Here we use the samples of spiral and elliptical galaxies, in order to investigate theoretically some of their properties and to test the empirical relations, in the light of modified gravities. We show that the baryonic Tully-Fisher relation can be described in the light of $f(R)$ gravity, without introducing the dark matter. Also, it is possible to explain the features of fundamental plane of elliptical galaxies without the dark matter hypothesis.

Key words: gravitation – cosmology: observations – cosmology: theory – galaxies: fundamental parameters – methods: data analysis

1. Introduction

In this review we want to make a comparison between ΛCDM, MOND and the modified gravities regarding some empirical relations connecting the properties of galaxies. For these investigations, the samples of many galaxies, spiral as well as elliptical, are used. As we were able to explain some features of galaxies in the light of modified gravities, our investigations are showing that we do not need any dark matter hypothesis.

The modified theories of gravity have been proposed like alternative approaches to Einstein theory of gravity: (Fischbach, 2004; Capozziello & De Laurentis, 2011; Nojiri & Odintsov , 2011; Nojiri et al., 2017; Borka et al., 2021). In this work we consider $f(R)$ gravity, specifically power-law fourth-order theories of gravity (Capozziello et al., 2007). $f(R)$ gravity is a straightforward extension of General Relativity (GR) where, instead of the Hilbert-Einstein action, linear in the Ricci scalar R, one considers a power-law $f(R) = f_{0n}R^n$ in the gravity Lagrangian (Zakharov et al., 2006, 2007; Capozziello et al., 2007; Capozziello & De Laurentis, 2011; Borka et al., 2012; Zakharov et al., 2014). In the weak field limit, a gravitational potential is of the form (Capozziello et al., 2007):

$$\Phi\left(r\right) = -\frac{GM}{2r}\left[1 + \left(\frac{r}{r_c}\right)^{\beta}\right],$$ (1)

where r_c is the scale-length parameter and it is related to the boundary conditions and the mass of the system and β is a universal parameter related to the power n. It is possible to demonstrate that the relation:

$$\beta = \frac{12n^2 - 7n - 1 - \sqrt{36n^4 + 12n^3 - 83n^2 + 50n + 1}}{6n^2 - 4n + 2}.$$ (2)

holds (Capozziello et al., 2007). For the case $n = 1$ and $\beta = 0$ the Newtonian potential is recovered.

Being n any real number, it is always possible to recast the $f(R)$ power-law function as

$$f(R) \propto R^{1+\epsilon}.$$ (3)

If we assume small deviation with respect to GR, that is $|\epsilon| \ll 1$, it is possible to re-write a first-order Taylor expansion as

$$R^{1+\epsilon} \simeq R + \epsilon R \log R + O(\epsilon^2).$$ (4)

2. Observed empirical relations of galaxies

Galaxies can commonly be divided into four main types (Binney & Tremaine, 2007):

– Spiral galaxies;

– Elliptical galaxies;

– Lenticular galaxies;

– Irregular galaxies.

In this work we will study main global observables of spiral and elliptical galaxies.

2.1. Main global observables of spiral galaxies

Most spiral galaxies consist of a central concentration of stars, known as the bulge, flat rotating stellar disk (with gas and dust) and surrounding near-spherical halo of stars. Main global observables of spiral galaxies are total luminosity L, its flat rotational velocity v_c, the mass of the stars M^* and mass of the gas Mg. Typical circular speeds of spirals are between 100 and 300 km/s.

The rotation rate of spirals in the flat part of the circular-speed curve is related to their luminosity by the Tully-Fisher law (Said, 2023).

Let us here mention the ratio of the mass of a galaxy to its total luminosity, i.e. mass-to-light ratio ($\Upsilon = M/L$). This is an important concept of spiral galaxies which shows us what kind of matter makes up most of the luminous population of the galaxy. A high Υ may indicate presence of dark matter, while a low Υ indicates that most of the matter is in the form of baryonic matter, stars and stellar remnants plus gas.

2.2. Main global observables of elliptical galaxies

Main sources of luminosity in elliptical galaxies would be: stellar plasma, hot gas, accreting black holes in the cores of galaxy bulges (see e.g. Sparke & Gallagher (2007) and references therein).

Surface brightness I is flux F within angular area Ω^2 on the sky ($\Omega = D/d$, where D is side of a small patch in a galaxy located at a distance d). I is independent of distance d: $I = F/\Omega^2 = L/(4\pi d^2) \times (d/D)^2 = L/(4\pi D^2)$, where L is luminosity (see e.g. § 1.3.1 in Sparke & Gallagher (2007)).

According to luminosity, their classification is the following:

1. Massive/luminous ellipticals ($L > 2 \times 10^{10} L_\odot$). They have lots of hot X-ray emitting gas, very old stars, lots of globular clusters, and are characterized by little rotation.

2. Intermediate mass/luminosity ellipticals ($L > 3 \times 10^9 L_\odot$). Their characteristic is power law central brightness distribution. They have little cold gas and moderate rotation.

3. Dwarf ellipticals ($L < 3 \times 10^9 L_\odot$). Their surface brightness is exponential. There is no rotation (Borka Jovanović et al., 2019).

Surface brightness of most elliptical galaxies, measured along the major axis of a galaxy's image, can be fit by de Vaucouleurs profile: $I(r) = I_e \times 10^{-3.33\left((r/r_e)^{1/4}-1\right)}$. De Vaucouleurs profile is a particularly good description of the surface brightness of giant and midsized elliptical galaxies (Ciotti, 1996; Cardone, 2004). The Sersic $r^{1/n}$ profile: $I(r) = I_e \times 10^{-b_n\left((r/r_e)^{1/n}-1\right)}$ (the constant b_n is chosen such that half of the luminosity comes from $r < r_e$), which generalizes the de Vaucouleurs profile, is also well suited to describe the surface brightness distribution of dwarf ellipticals for $n = 1$ (Ciotti, 1996; Cardone, 2004).

2.3. Data

In order to compare theoretical results with observations, we use data reported in Table I of Ref. Burstein et al. (1997). We used effective radii, effective luminosities and characteristic velocities of galaxies, galaxy groups, galaxy clusters

and globular clusters. For circular velocity v_c from that table in case of ellipticals is $v_c = \sigma_0$. The total number of galaxies that we take into account is 1150, while among them there are 400 elliptical galaxies.

We also used the data for the observed Baryonic Tully-Fisher relation of gas rich galaxies obtained by McGaugh (2011), and listed in Table 1 of our Ref. Capozziello et al. (2017).

3. Tully-Fisher relations in the light of R^n modified gravity

There are several different forms of the Tully-Fisher relation, depending on which properties are related: the measurements of mass, luminosity or rotation velocity.

3.1. The Tully-Fisher relation

The Tully-Fisher relation (TFR) is the following empirical relation that correlates the intrinsic brightness of a spiral galaxy, measured by its total luminosity L, and its dynamical properties, measured by its maximum rotational velocity $V_{\rm rot}$ (Said, 2023):

$$L \propto V_{\rm rot}^4. \tag{5}$$

Tully & Fisher (1977) proposed the use TFR as a distance indicator to measure the distances of spiral galaxies independent of their cosmological redshifts. Tully and Fisher applied their TFR to derive distances to the Virgo and Ursa Major clusters and they obtained a Hubble constant of $H_0 = 84$ km s^{-1} Mpc^{-1} for Virgo and $H_0 = 75$ km s^{-1} Mpc^{-1} for Ursa Major (Tully & Fisher, 1977). Since then TFR plays an important role in the Hubble constant measurements, and this methodology typically involves the following steps (Said, 2023): the first step is to select a sample of galaxies with well-measured rotational velocities and luminosities; the second step is to calibrate the TFR for this sample of galaxies (measuring the slope, intercept, and scatter of the relation for the sample), and in that way calibrated TFR can be used to infer the distances to other galaxies with similar properties; the final step is to plot the derived distances against redshift in order to measure H_0. TFR is also used for measuring the peculiar velocities of galaxies, and thus it represents an important tool in observational cosmology.

Although the physical origin of TFR is still not fully understood, it is widely accepted that TFR is a direct consequence of gravitational physics and the dynamics of galactic rotation. In addition, the standard ΛCDM cosmological model predicts that rotational velocities of spiral galaxies are in large part determined by gravitational attraction of their dark matter halos. Thus, in ΛCDM cosmology TFR is a consequence of both visible and dark matter mass.

3.2. The Baryonic Tully-Fisher relation

Another important and closely related scaling relation is **the Baryonic Tully-Fisher relation (BTFR)** which connects galaxy's baryonic mass M_b (M_b being the sum of its stellar and gas masses: $M_b = M_* + M_{\mathrm{gas}}$) with its rotation velocity V_{rot}. BTFR follows from TFR due to the fact that luminosity L traces baryonic mass M_b through the mass-to-light ratio, and thus it takes the following form (McGaugh et al., 2000):

$$M_b \propto V_{\mathrm{rot}}^4. \tag{6}$$

BTFR has a smaller intrinsic scatter than the original TFR and poses a challenge to the standard ΛCDM model since, as illustrated in Figure 1, this model predicts a higher intrinsic scatter of ~ 0.15 dex and a lower slope of ~ 3 compared to the observed scatter of ~ 0.10 dex and slope of ~ 4 (Lelli et al., 2016). This discrepancy imposes the need for further investigation of galaxy dynamics and mass distribution.
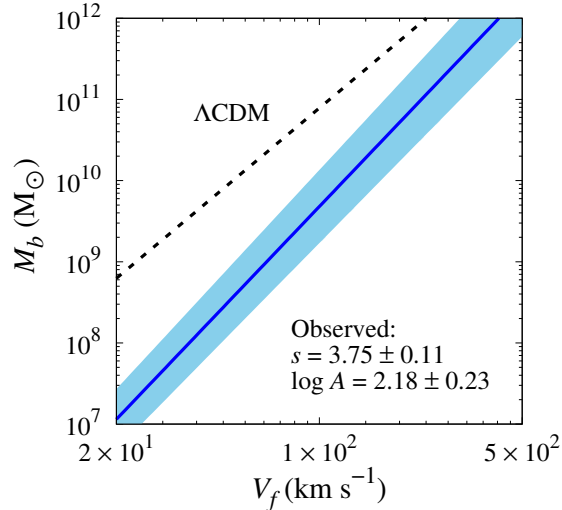
Figure 1. Comparison between the BTFR obtained by error-weighted fits from a sample of the galaxies with accurate distances from Lelli et al. (2016) (blue solid line with light blue band denoting the intrisic scatter of 0.1 dex), and BTFR in ΛCDM cosmology (black dashed line). Observed BTFR and BTFR in ΛCDM cosmology are plotted using the Eqs. (6) and (8) from Lelli et al. (2016), respectively.

On the other hand, a more robust prediction for BTFR is obtained in the frame of the Modified Newtonian Dynamics (MOND), a modified theory of gravity proposed by Milgrom (1983) which modifies the Newtonian dynamics at low acceleration in order to provide an alternative to dark matter. In MOND,

galaxy's baryonic mass is at the same time its total mass, and BTFR with power-law exponent exactly equal to 4 is a direct consequence of the modification of gravitational force law at low acceleration (McGaugh, 2011, 2012).

4. The fundamental plane in the light of R^n modified gravity

The analogue empirical relation to TFR in the case of elliptical galaxies is known as **the Faber-Jackson relation** which, together with the virial theorem, results in a more general correlation between their effective radii, average surface brightnesses and central velocity dispersions known as **the fundamental plane (FP)**. When written in logarithmic form, FP describes a plane in the three-dimensional phase space of these galaxy properties which appears to be tilted by an angle of $\sim 15°$ with respect to the expected plane predicted by the virial theorem (see e.g. Borka Jovanović et al., 2016, and references therein). This discrepancy, together with small thickness of FP, represents a puzzle, and it is usually assumed to be caused by the non-homology in the dynamical structures of the systems and mainly driven by the dark matter.
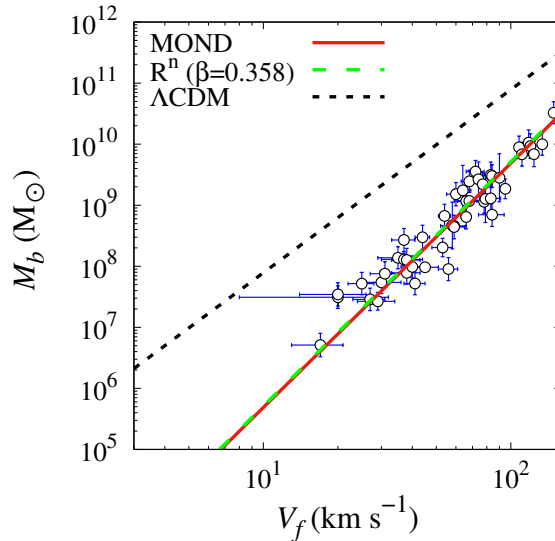
Figure 2. Comparison between best fit BTFRs of gas-rich galaxies (for a sample of galaxies used in (McGaugh, 2011)), in MOND, R^n gravity for $n = 1.25$ (corresponding β is 0.358) and ΛCDM. All values we calculated, except for open circles which are observed data from (McGaugh, 2011).

In case of elliptical galaxies there are three main global observables: the central projected velocity dispersion σ_0, the effective radius r_e, and the mean
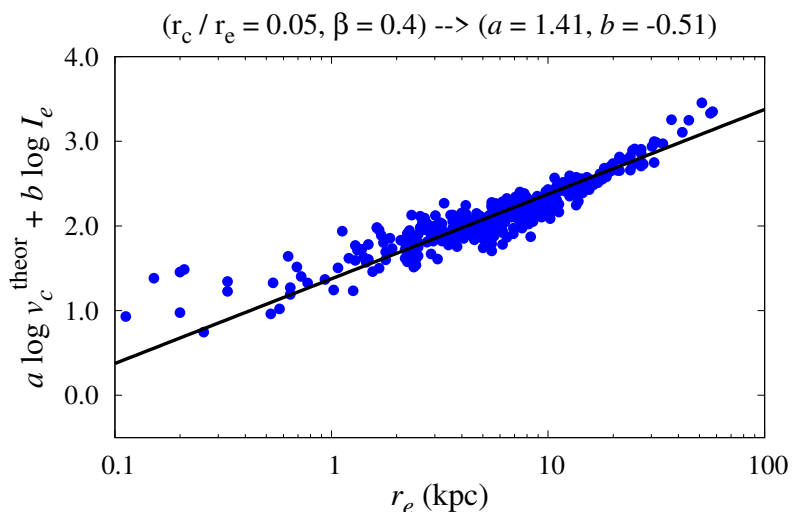
Figure 3. Fundamental plane (log scale for x-axes) of elliptical galaxies with calculated circular velocity v_c^{theor}, and observed effective radius r_e and mean surface brightness (within the effective radius) I_e, for $r_c/r_e = 0.05$ and $\beta = 0.4$. Black solid line is result of 3D fit of FP (the obtained calculated FP coefficients are $a = 1.41$ and $b = $ -0.51).

effective surface brightness (within r_e) I_e. The empirical fact tell us that some global properties of normal elliptical galaxies are correlated and this correlated plane is referred to as the FP (Bender et al., 1992, 1993; Busarello et al., 1997):

$$log(r_e) = a \times log(\sigma_0) + b \times log(I_e) + c. \qquad (7)$$

We want to recover FP using $f(R)$ gravity, which means to find connection between the parameters of FP equation and parameters of the $f(R)$ gravity potential (Borka Jovanović et al., 2016, 2019):

– r_e is in correlation with r_c;

– σ_0 is in correlation with v_{vir} (virial velocity in $f(R)$), and

– I_e is in correlation with r_c (through the r_c/r_e ratio).

However, some recent studies demonstrated that both BTFR of spiral galaxies and FP of ellipticals could be also recovered in the frame of the modified $f(R)$ theories of gravity without need for the dark matter hypothesis (see e.g. Borka Jovanović et al., 2016; Capozziello et al., 2017, 2018, 2020, and references therein). The comparison between the observed and best fit baryonic Tully-Fisher relations of gas-rich galaxies in MOND, R^n gravity and ΛCDM, we show

in Figure 2. Fundamental plane (log scale for x-axes) of elliptical galaxies with calculated circular velocity v_c^{theor}, and observed effective radius r_e and mean surface brightness (within the effective radius) I_e, for $r_c/r_e = 0.05$ and $\beta = 0.4$ are given in Figure 3. The obtained calculated FP coefficients are $a = 1.41$ and $b = $ -0.51.

5. Discussion and conclusions

In this paper we use $f(R)$ theories of gravity, particularly power-law R^n gravity, and demonstrate that the missing matter problem in galaxies can be addressed by power-law R^n gravity. Using this approach, it is possible to explain the Fundamental Plane of elliptical galaxies and the baryonic Tully-Fisher relation of spiral galaxies without the DM hypothesis. Also, we can claim that the effective radius is led by gravity and the whole galactic dynamics can be addressed by $f(R)$ theories. Also, $f(R)$ gravity can give a theoretical foundation for rotation curve of galaxies (Yegorova et al., 2012; Cattaneo et al., 2014). We have to stress that obtained value for parameter β from galactic rotation curves or BTF differs from parameter β obtained using observational data at planetary or star orbit scales (Borka et al., 2012). The reason for this result is that gravity is not a scale-invariant interaction and then it differs at galactic scales with respect to local scales.

Also, we investigated some forms of TFR in the light of $f(R)$ gravities. These investigations are leading to the following conclusions:
- $f(R)$ gravity can give a theoretical foundation for the empirical BTFR,
- MOND is a particular case of $f(R)$ gravity in the weak field limit,
- ΛCDM is not in satisfactory agreement with observations,
- FP can be recovered by R^n gravity.

References

Bender, R., Burstein, D., Faber, S. M., Dynamically hot galaxies. I. Structural properties. 1992, *Astrophys. J.* **399**, 462

Bender, R., Burstein, D., Faber, S. M., Dynamically hot galaxies. I. Global stellar populations. 1993, *Astrophys. J.* **411**, 153

Binney, J., Tremaine, S., "Galactic Dynamics", second eddition, Princeton University Press, 2007, US.

Borka, D., Jovanović, P., Borka Jovanović, V., Zakharov, A. F., Constraints on R^n gravity from precession of orbits of S2-like stars. 2012, *Phys. Rev. D* **85**, 124004

Borka, D., Borka Jovanović, V., Capozziello, S., Zakharov, A. F., Jovanović, P., Estimating the Parameters of Extended Gravity Theories with the Schwarzschild Precession of S2 Star. 2021, *Universe* **7**, 407.

Borka Jovanović, V., Capozziello, S., Jovanović, P., Borka, D., Recovering the fundamental plane of galaxies by $f(R)$ gravity. 2016, *Phys. Dark Universe* **14**, 73

Borka Jovanović, V., Jovanović, P., Borka, D., Capozziello, S., Fundamental plane of elliptical galaxies in $f(R)$ gravity: the role of luminosity. 2019, *Atoms* **7**, 4

Burstein, B., Bender, R., Faber, S. M., Nolthenius, R., Global relationships among the physical properties of stellar systems. 1997, *Astron. J.* **114**, 1365

Busarello, G., Capaccioli, M., Capozziello, S., Longo, G., Puddu, E., The relation between the virial theorem and the fundamental plane of elliptical galaxies. 1997, *Astron. Astrophys.* **320**, 415

Capozziello, S., Cardone, V. F., Troisi, A., Low surface brightness galaxy rotation curves in the low energy limit of R^n gravity: no need for dark matter? 2007, *Mon. Not. R. Astron. Soc.* **375**, 1423

Capozziello, S., De Laurentis, M., Extended theories of gravity. 2011, *Phys. Rep.* **509**, 167

Capozziello, S., Jovanović, P., Borka Jovanović, V., Borka, D., Addressing the missing matter problem in galaxies through a new fundamental gravitational radius. 2017, *J. Cosmol. Astropart. P.* **2017**, No. 06, 044

Capozziello, S., Borka, D., Borka Jovanović, V., Jovanović, P., Galactic Structures from Gravitational Radii. 2018, *Galaxies* **6**, 22

Capozziello, S., Borka Jovanović, V., Borka, D., Jovanović, P., Constraining theories of gravity by fundamental plane of elliptical galaxies. 2020, *Phys. Dark Universe* **29**, 100573

Cardone, V. F., The lensing properties of the Sersic model. 2004, *Astron. Astrophys.* **415**, 839

Cattaneo A., Salucci, P., Papastergis, E., Galaxy luminosity function and Tully-Fisher relation: reconciled through rotation-curve studies. 2014, *Astrophys. J.* **783**, 66

Ciotti, L., Lanzoni, B., Renzini, A., The tilt of the fundamental plane of elliptical galaxies - I. Exploring dynamical and structural effects. 1996, *Mon. No. R. Astron. Soc.* **282**, 1

Fischbach, E., Talmadge, C. L., The Search for Non-Newtonian Gravity, Springer: Heidelberg, Germany; New York, NY, USA, 1999; 305p.

Lelli, F. et al., The Small Scatter of the Baryonic Tully-Fisher Relation. 2016, *Astrophys. J. Lett.* **816(1)**, L14

McGaugh, S. S. et al., The Baryonic Tully-Fisher Relation. 2000, *Astrophys. J. Lett.* **533**, L99

McGaugh, S. S., Novel Test of Modified Newtonian Dynamics with Gas Rich Galaxies. 2011, *Phys. Rev. Lett.* **106**, 121303

McGaugh, S. S., The Baryonic Tully-Fisher Relation of Gas-rich Galaxies as a Test of ΛCDM and MOND. 2012, *Astron. J.* **143(2)**, 40

Milgrom, M., A modification of the Newtonian dynamics as a possible alternative to the hidden mass hypothesis. 1983, *Astrophys. J.* **270**, 365

Nojiri, S., Odintsov, S. D., Unified cosmic history in modified gravity: from $F(R)$ theory to Lorentz non-invariant models. 2011, *Phys. Rept.* **505**, 59

Nojiri, S., Odintsov, S. D., Oikonomou, V. K., Modified Gravity Theories on a Nutshell: Inflation, Bounce and Late-time Evolution. 2017, *Phys. Rept.* **692**, 1

Said, K., Tully-Fisher relation, 2023, arXiv:2310.16053

Sparke, L. S., Gallagher, J. S., Galaxies in the Universe: An Introduction, Cambridge University Press, 2007, ISBN: 9780521671866

Tully, R. B., Fisher, J. R., A new method of determining distances to galaxies. 1977, *Astron. Astrophys.* **54**, 661

Yegorova, I. A., Babic, A., Salucci P., Spekkens, K., Pizzella, A., Rotation curves of luminous spiral galaxies. 2012, *Astron. Astrophys. Trans.* **27**, 335

Zakharov, A. F., Nucita, A. A., Paolis, F. D., Ingrosso, G., Solar system constraints on R^n gravity. 2006, *Phys. Rev. D* **74**, 107101

Zakharov, A. F., Nucita, A. A., Paolis, F. D., Ingrosso, G., Apoastron shift constraints on dark matter distribution at the Galactic Center. 2007, *Phys. Rev. D* **76**, 062001

Zakharov, A. F., Borka, D., Borka Jovanović, V., Jovanović, P., Constraints on R^n gravity from precession of orbits of S2-like stars: A case of a bulk distribution of mass. 2014, *Adv. Space Res.* **54**, 1108

On the Stark broadening of N II spectral lines

M.S. Dimitrijević[1,2] , **M.D. Christova**[3]

and S. Sahal-Bréchot[2]

[1] *Astronomical Observatory, Volgina 7, 11060 Belgrade, Serbia (E-mail: mdimitrijevic@aob.rs)*

[2] *Sorbonne Université, Observatoire de Paris, Université PSL, CNRS, LUX, F-92190, Meudon, France*

[3] *Department of Applied Physics, Technical University of Sofia, 1000 Sofia, Bulgaria*

Abstract. Stark broadening parameters, widths and shifts, for spectral lines within 45 N II multiplets, have been calculated for collisions with He III, B II; B III and B IV ions, by using the semiclassica perturbation method. The obtained data are of particular interest for proton-boron fusion experiments where boron nitride (BN) targets are used.

Key words: Stark broadening – N II – spectral lines – line profiles – proton-boron fusion

1. Introduction

Stark broadening is successfully implemented for spectroscopy diagnostics of astrophysical and laboratory plasma, as well as for laser, industrial, technological and fusion plasma. Recently, many experimental and theoretical efforts are oriented to the new direction of nuclear fusion, proton-boron fusion. Proton-boron fusion reaction is potentially promising for production of energy with several considerable advantages (Belloni, 2022). There are no radioactive species and neutrons in the reaction. Regarding the reactants, they are stable, cheap and abundant in nature. The fact that the production of neutrons is very low during the fusion process means that there is no induced activation of the environment surrounding the fuel. Clean fusion energy is a very important advantage. The proton-boron fusion produces three alpha particles and releases about 8.7 MeV. Three papers (Yoon et al., 2014; Giuffrida et al., 2016; Cirrone et al., 2018) report that α-particle generation during proton-boron fusion could be a valuable source for medical and industrial applications. According to the measurements and results presented by Schollmeier et al. (2022), boron-nitride (BN) nanotube targets are more efficient than regular foils and previously published nanostructured targets, so that in some experiments BN targets are used. Hegelich et al.

(2023) underline that in order to optimize the fusion yield, a plasma diagnostic is needed. Consequently, Stark broadening data for N II may be useful for determination of conditions in fusion plasma.

Our aim here is to calculate Stark broadening parameters for 45 multiplets of singly charged nitrogen (N II), for collisions with He III (alpha particles), B II, B III and B IV ions, in order to provide the data needed for proton-boron fusion experiments with BN targets.

2. Theory

In order to calculate Stark broadening parameters for spectral lines within the considered multiplets of singly charged nitrogen, the semiclassical perturbation theory (Sahal-Bréchot, 1969a,b; Sahal-Bréchot, Dimitrijević, & Ben Nessib, 2014) has been used. Since it has been described in detail in above mentioned references, only basic formulas will be given here, in order to understand the method of calculations. The full width at half maximum (FWHM - W) and shift (d) of an isolated spectral line of a non-hydrogenic ion is given as:

$$W = N \int vf(v)dv \left(\sum_{i' \neq i} \sigma_{ii'}(v) + \sum_{f' \neq f} \sigma_{ff'}(v) + \sigma_{el} \right)$$

$$d = N \int vf(v)dv \int_{R_3}^{R_D} 2\pi\rho d\rho \sin(2\varphi_p). \tag{1}$$

where i and f denote the initial and final level of the corresponding transition; i' and f' are perturbing levels; N perturber density; v perturber velocity, and $f(v)$ is the Maxwellian distribution of electron velocities. The inelastic cross sections $\sigma_{kk'}(v)$, $k = i, f$ are presented here by an integration of the transition probability $P_{kk'}(\rho, v)$, over the impact parameter ρ as:

$$\sum_{k' \neq k} \sigma_{kk'}(v) = \frac{1}{2}\pi R_1^2 + \int_{R_1}^{R_D} 2\pi\rho d\rho \sum_{k' \neq k} P_{kk'}(\rho, v). \tag{2}$$

The cross section for elastic collisions is given as:

$$\sigma_{el} = 2\pi R_2^2 + \int_{R_2}^{R_D} 2\pi\rho d\rho \sin^2 \delta + \sigma_r,$$

$$\delta = (\varphi_p^2 + \varphi_q^2)^{\frac{1}{2}}. \tag{3}$$

Here, δ denotes the phase shift with components φ_p (r^{-4}) and φ_q (r^{-3}), describing contributions due to polarization and quadrupole potentials, respectively. The method of symmetrization and calculation of cut-off parameters R_1, R_2, R_3, and the Debye cut-off R_D is explained in Sahal-Bréchot (1969b). The calculation of the contribution of Feshbach resonances (σ_r), is explained in detail in Fleurier et al. (1977) and Sahal-Bréchot (2021).

3. Results and discussion

We calculated Stark broadening parameters, full width at half intensity maximum (FWHM - W) and shift (d) by empoying the semiclassical perturbation theory (Sahal-Bréchot, 1969a,b; Sahal-Bréchot, Dimitrijević, & Ben Nessib, 2014). The electron density is 10^{16} cm^{-3} and temperatures 5 000 K, 10 000 K, 30 000 K, 50 000 K, 100 000 K, and 200 000 K. Atomic energy levels needed for present calculations have been taken from Moore (1993) and Kramida et al. (2021).

The results, for Stark Full Width at Half intensity Maximum (FWHM) and shift for 45 N II multiplets broadened by collisions with He III and B II ions are presented in Table 1, and broadened by collisions with B III and B IV in Table 2.

Since the wavelengths are calculated from atomic energy levels, they are not identical with wavelengths in NIST databases (Kramida et al., 2021).

From the quantity C (Dimitrijević & Sahal-Bréchot, 1984), presented in Tables 1 and 2, one can obtain the maximal perturber density for which the line may be considered as isolated, if it is divided by the corresponding width (W). Namely, a line is isolated if nondegenerate energy levels, broadened by collisions, do not overlap. This is satisfied if the width of a line is smaller or equal to the energy distance to the nearest perturbing level, represented by the quantity C. So the density limit is density where the values of C and the corresponding width are equal.

Additionally, we checked the validity of impact approximation calculating the value of NV, where V is the collision volume and N the perturber density. If $NV < 0.1$, the impact approximation is valid. We excluded from tables the cases when $NV > 0.5$, since than the impact approximation is not valid. In the case when the violation of impact approximation is more or less tolerable, for $0.1 < NV \leq 0.5$ we put an asterisk before the corresponding Stark broadening parameter in order to draw attention that this value is on the limit of validity of impact approximation

In order to obtain the line profile $F(\omega)$ (where ω is angular frequency) from the values given in Tables 1 and 2, we can use the expression:

$$F(\omega) = \frac{W/(2\pi)}{(\omega - \omega_{if} - d)^2 + (W/2)^2}. \tag{4}$$

Here

$$\omega_{if} = \frac{E_i - E_f}{\hbar}$$

where E_i, E_f are the energies of initial and final atomic energy level, respectively.

4. Conclusions

The Stark broadening parameters, FWHM and shifts, determining Lorentzian profile of a spectral line, have been calculated for 45 multiplets of singly charged nitrogen ion (N II), with the help of the impact semiclassical perturbation theory (Sahal-Bréchot, 1969a,b; Sahal-Bréchot, Dimitrijević, & Ben Nessib, 2014). The calculations have been performed for broadening by collisions of N II ion with He III, B II, B III and B IV ions. Such results are of interest for investigation of proton-boron fusion, since in some experimental devices boron nitride (BN) targets are used, so that broadening of N II by collisions with different boron ions is of interest for diagnostic purposes and for optimization, modeling and investigation of created plasma. The presented Stark broadening parameters will also be implemented in STARK-B database (http://stark-b.obspm.fr/ - Sahal-Bréchot et al. (2015)), which is also a part of Virtual Atomic and Molecular Data Center (VAMDC) (http://www.vamdc.org/ - Dubernet et al. (2010, 2016); Albert et al. (2020)).

M.S. Dimitrijević, M.D. Christova and S. Sahal-Bréchot

Table 1. This table gives He III-, and B II-impact broadening parameters for N II multiplets, Stark FWHM W and shift d, expressed in Å. Calculated wavelength of the transitions (in Å) and parameter C are also given. This parameter, when divided with the corresponding Stark width, gives an estimate for the maximal pertuber density for which the line may be treated as isolated. Results are for perturber density of 10^{16} cm^{-3} and temperatures are from 5 000 K to 200 000 K. A positive shift is towards the red part of the spectrum. An asterisk before a value indicates that this value is on the limit of validity of impact approximation.

		He III		B II	
TRANSITION	T[K]	W[Å]	d[Å]	W[Å]	d[Å]
N II 3s^{1}P^o-3p^{1}P	5000.	0.452E-02	-0.145E-02	0.379E-02	-0.717E-03
6483.8 Å	10000.	0.776E-02	-0.269E-02	0.532E-02	-0.118E-02
C=0.65 10^{20}	30000.	0.121E-01	-0.493E-02	0.667E-02	-0.184E-02
	50000.	0.135E-01	-0.570E-02	0.722E-02	-0.211E-02
	100000.	0.153E-01	-0.682E-02	0.765E-02	-0.252E-02
	200000.	0.164E-01	-0.806E-02	0.802E-02	-0.289E-02
N II 3s^{1}P^o-3p^{1}D	5000.	0.274E-02	0.363E-03	0.214E-02	0.183E-03
3996.1 Å	10000.	0.432E-02	0.702E-03	0.288E-02	0.316E-03
C=0.21 10^{20}	30000.	0.626E-02	0.134E-02	0.350E-02	0.518E-03
	50000.	0.686E-02	0.160E-02	0.374E-02	0.592E-03
	100000.	0.758E-02	0.192E-02	0.388E-02	0.708E-03
	200000.	0.793E-02	0.230E-02	0.405E-02	0.813E-03
N II 3s^{1}P^o-3p^{1}S	5000.	0.324E-02	0.281E-02	0.213E-02	0.120E-02
3438.1 Å	10000.	0.519E-02	0.429E-02	0.286E-02	0.174E-02
C=0.14 10^{20}	30000.	0.800E-02	0.640E-02	0.373E-02	0.236E-02
	50000.	0.915E-02	0.729E-02	0.416E-02	0.270E-02
	100000.	0.112E-01	0.858E-02	0.442E-02	0.301E-02
	200000.	0.119E-01	0.939E-02	0.498E-02	0.348E-02
N II 3s^{1}P^o-4p^{1}P	5000.	0.333E-02	0.587E-04	0.217E-02	0.300E-04
1887.4 Å	10000.	0.438E-02	0.117E-03	0.248E-02	0.532E-04
C=0.15 10^{19}	30000.	0.530E-02	0.232E-03	0.283E-02	0.916E-04
	50000.	0.561E-02	0.285E-03	0.291E-02	0.105E-03
	100000.	0.583E-02	0.341E-03	0.300E-02	0.126E-03
	200000.	0.600E-02	0.409E-03	0.302E-02	0.149E-03
N II 3s^{1}P^o-4p^{1}D	5000.	0.400E-02	0.142E-02	0.242E-02	0.616E-03
1780.6 Å	10000.	0.508E-02	0.215E-02	0.278E-02	0.825E-03
C=0.15 10^{19}	30000.	0.635E-02	0.304E-02	0.315E-02	0.113E-02
	50000.	0.679E-02	0.343E-02	0.330E-02	0.122E-02
	100000.	0.751E-02	0.405E-02	0.339E-02	0.141E-02
	200000.	0.751E-02	0.434E-02	0.374E-02	0.171E-02
N II 3s^{1}P^o-4p^{1}S	5000.	*0.640E-02	*0.457E-02	*0.315E-02	*0.183E-02
1732.4 Å	10000.	*0.827E-02	*0.631E-02	0.377E-02	0.248E-02
C=0.13 10^{19}	30000.	*0.113E-01	*0.915E-02	0.469E-02	0.328E-02
	50000.	0.123E-01	0.102E-01	0.485E-02	0.359E-02
	100000.	0.145E-01	0.112E-01	0.533E-02	0.427E-02
	200000.	0.164E-01	0.124E-01	0.687E-02	0.472E-02

Table 1. Continued.

		He III		B II	
TRANSITION	T[K]	W[Å]	d[Å]	W[Å]	d[Å]
N II 2p^{21}D-3s^{1}P^o	5000.	0.663E-05	0.291E-04	0.534E-05	0.140E-04
747.0 Å	10000.	0.243E-04	0.526E-04	0.138E-04	0.218E-04
C=0.86 10^{18}	30000.	0.741E-04	0.907E-04	0.305E-04	0.335E-04
	50000.	0.971E-04	0.104E-03	0.374E-04	0.386E-04
	100000.	0.122E-03	0.124E-03	0.493E-04	0.453E-04
	200000.	0.160E-03	0.145E-03	0.559E-04	0.511E-04
N II 2p^{21}S-3s^{1}P^o	5000.	0.899E-05	0.384E-04	0.729E-05	0.185E-04
858.4 Å	10000.	0.325E-04	0.695E-04	0.185E-04	0.288E-04
C=0.11 10^{19}	30000.	0.984E-04	0.120E-03	0.406E-04	0.442E-04
	50000.	0.129E-03	0.137E-03	0.498E-04	0.510E-04
	100000.	0.162E-03	0.164E-03	0.655E-04	0.598E-04
	200000.	0.212E-03	0.192E-03	0.741E-04	0.675E-04
N II 2p^{21}D-3d^{1}D^o	5000.	0.528E-04	-0.130E-04	0.418E-04	-0.641E-05
582.2 Å	10000.	0.850E-04	-0.241E-04	0.570E-04	-0.104E-04
C=0.30 10^{18}	30000.	0.126E-03	-0.435E-04	0.695E-04	-0.161E-04
	50000.	0.139E-03	-0.500E-04	0.750E-04	-0.185E-04
	100000.	0.155E-03	-0.605E-04	0.788E-04	-0.217E-04
	200000.	0.164E-03	-0.702E-04	0.802E-04	-0.251E-04
N II 2p^{21}D-3d^{1}F^o	5000.	0.611E-04	0.773E-05	0.474E-04	0.390E-05
574.7 Å	10000.	0.955E-04	0.149E-04	0.631E-04	0.670E-05
C=0.50 10^{18}	30000.	0.137E-03	0.284E-04	0.765E-04	0.110E-04
	50000.	0.150E-03	0.338E-04	0.815E-04	0.125E-04
	100000.	0.164E-03	0.407E-04	0.852E-04	0.148E-04
	200000.	0.173E-03	0.488E-04	0.877E-04	0.171E-04
N II 2p^{21}D-3d^{1}P^o	5000.	0.655E-04	0.198E-04	0.498E-04	0.942E-05
572.1 Å	10000.	0.102E-03	0.352E-04	0.661E-04	0.145E-04
C=0.39 10^{18}	30000.	0.148E-03	0.594E-04	0.805E-04	0.219E-04
	50000.	0.163E-03	0.679E-04	0.859E-04	0.250E-04
	100000.	0.181E-03	0.812E-04	0.891E-04	0.295E-04
	200000.	0.191E-03	0.934E-04	0.957E-04	0.337E-04
N II 2p^{21}S-3d^{1}P^o	5000.	0.811E-04	0.244E-04	0.616E-04	0.116E-04
635.2 Å	10000.	0.126E-03	0.435E-04	0.817E-04	0.179E-04
C=0.48 10^{18}	30000.	0.183E-03	0.733E-04	0.994E-04	0.271E-04
	50000.	0.202E-03	0.837E-04	0.106E-03	0.309E-04
	100000.	0.224E-03	0.100E-03	0.110E-03	0.364E-04
	200000.	0.236E-03	0.115E-03	0.118E-03	0.416E-04
N II 3p^{1}P-3d^{1}P^o	5000.	0.443E-02	0.663E-03	0.326E-02	0.323E-03
3920.1 Å	10000.	0.659E-02	0.122E-02	0.406E-02	0.516E-03
C=0.18 10^{20}	30000.	0.885E-02	0.216E-02	0.489E-02	0.795E-03
	50000.	0.963E-02	0.249E-02	0.515E-02	0.910E-03
	100000.	0.105E-01	0.295E-02	0.530E-02	0.108E-02
	200000.	0.109E-01	0.347E-02	0.563E-02	0.126E-02

Table 1. Continued.

TRANSITION	T[K]	He III W[Å]	d[Å]	B II W[Å]	d[Å]
N II $3p^1P$-$3d^1D^o$	5000.	0.494E-02	-0.111E-02	0.367E-02	-0.530E-03
4448.3 Å	10000.	0.747E-02	-0.199E-02	0.469E-02	-0.822E-03
C=0.17 10^{20}	30000.	0.104E-01	-0.340E-02	0.569E-02	-0.126E-02
	50000.	0.113E-01	-0.387E-02	0.599E-02	-0.143E-02
	100000.	0.123E-01	-0.468E-02	0.618E-02	-0.168E-02
	200000.	0.130E-01	-0.524E-02	0.660E-02	-0.193E-02
N II $3p^1D$-$3d^1D^o$	5000.	0.189E-01	-0.615E-02	0.136E-01	-0.288E-02
7764.4 Å	10000.	0.281E-01	-0.102E-01	0.168E-01	-0.425E-02
C=0.53 10^{20}	30000.	0.380E-01	-0.164E-01	0.205E-01	-0.611E-02
	50000.	0.418E-01	-0.188E-01	0.215E-01	-0.696E-02
	100000.	0.454E-01	-0.221E-01	0.224E-01	-0.799E-02
	200000.	0.498E-01	-0.256E-01	0.227E-01	-0.901E-02
N II $3p^1D$-$3d^1F^o$	5000.	0.146E-01	-0.225E-02	0.106E-01	-0.108E-02
6612.4 Å	10000.	0.214E-01	-0.408E-02	0.129E-01	-0.169E-02
C=0.56 10^{20}	30000.	0.281E-01	-0.704E-02	0.155E-01	-0.259E-02
	50000.	0.307E-01	-0.805E-02	0.162E-01	-0.299E-02
	100000.	0.329E-01	-0.961E-02	0.170E-01	-0.354E-02
	200000.	0.341E-01	-0.113E-01	0.171E-01	-0.394E-02
N II $3p^1D$-$3d^1P^o$	5000.	0.136E-01	-0.531E-03	0.983E-02	-0.274E-03
6286.1 Å	10000.	0.198E-01	-0.107E-02	0.119E-01	-0.491E-03
C=0.47 10^{20}	30000.	0.257E-01	-0.217E-02	0.143E-01	-0.870E-03
	50000.	0.279E-01	-0.272E-02	0.149E-01	-0.101E-02
	100000.	0.299E-01	-0.326E-02	0.154E-01	-0.121E-02
	200000.	0.307E-01	-0.393E-02	0.159E-01	-0.139E-02
N II $3p^1S$-$3d^1P^o$	5000.	0.272E-01	-0.390E-02	0.194E-01	-0.187E-02
8441.1 Å	10000.	0.393E-01	-0.702E-02	0.233E-01	-0.290E-02
C=0.84 10^{20}	30000.	0.507E-01	-0.120E-01	0.279E-01	-0.446E-02
	50000.	0.549E-01	-0.137E-01	0.290E-01	-0.508E-02
	100000.	0.591E-01	-0.165E-01	0.304E-01	-0.593E-02
	200000.	0.621E-01	-0.187E-01	0.305E-01	-0.683E-02
N II $3d^1D^o$-$4p^1P$	5000.	0.456E-01	0.437E-02	0.292E-01	0.205E-02
6631.6 Å	10000.	0.588E-01	0.728E-02	0.333E-01	0.303E-02
C=0.19 10^{20}	30000.	0.713E-01	0.117E-01	0.379E-01	0.434E-02
	50000.	0.750E-01	0.134E-01	0.391E-01	0.496E-02
	100000.	0.785E-01	0.157E-01	0.397E-01	0.579E-02
	200000.	0.801E-01	0.182E-01	0.405E-01	0.636E-02
N II $3d^1D^o$-$4p^1D$	5000.	0.409E-01	0.148E-01	0.244E-01	0.638E-02
5476.8 Å	10000.	0.514E-01	0.222E-01	0.281E-01	0.856E-02
C=0.14 10^{20}	30000.	0.647E-01	0.320E-01	0.321E-01	0.115E-01
	50000.	0.699E-01	0.365E-01	0.337E-01	0.130E-01
	100000.	0.735E-01	0.408E-01	0.361E-01	0.148E-01
	200000.	0.784E-01	0.471E-01	0.374E-01	0.170E-01

Table 1. Continued.

TRANSITION	T[K]	He III W[Å]	d[Å]	B II W[Å]	d[Å]
N II 3d^{1}F^o-4p^{1}D	5000.	0.536E-01	0.180E-01	0.320E-01	0.783E-02
6244.1 Å	10000.	0.670E-01	0.273E-01	0.368E-01	0.105E-01
C=0.18 10^{20}	30000.	0.837E-01	0.387E-01	0.416E-01	0.144E-01
	50000.	0.897E-01	0.443E-01	0.437E-01	0.157E-01
	100000.	0.965E-01	0.513E-01	0.451E-01	0.179E-01
	200000.	0.101	0.567E-01	0.485E-01	0.213E-01
N II 3d^{1}P^o-4p^{1}P	5000.	0.731E-01	0.407E-02	0.466E-01	0.194E-02
8298.5 Å	10000.	0.939E-01	0.726E-02	0.532E-01	0.299E-02
C=0.30 10^{20}	30000.	0.114	0.123E-01	0.604E-01	0.453E-02
	50000.	0.120	0.140E-01	0.623E-01	0.518E-02
	100000.	0.124	0.168E-01	0.629E-01	0.611E-02
	200000.	0.127	0.191E-01	0.644E-01	0.704E-02
N II 3d^{1}P^o-4p^{1}D	5000.	0.596E-01	0.204E-01	0.355E-01	0.883E-02
6566.0 Å	10000.	0.746E-01	0.308E-01	0.409E-01	0.119E-01
C=0.20 10^{20}	30000.	0.937E-01	0.439E-01	0.466E-01	0.162E-01
	50000.	0.999E-01	0.503E-01	0.489E-01	0.178E-01
	100000.	0.105	0.576E-01	0.506E-01	0.203E-01
	200000.	0.113	0.647E-01	0.535E-01	0.240E-01
N II 3d^{1}P^o-4p^{1}S	5000.	*0.786E-01	*0.545E-01	*0.391E-01	*0.219E-01
5955.9 Å	10000.	*0.102	*0.756E-01	0.464E-01	0.295E-01
C=0.16 10^{20}	30000.	*0.137	*0.109	0.574E-01	0.391E-01
	50000.	0.149	0.121	0.596E-01	0.432E-01
	100000.	0.173	0.135	0.650E-01	0.511E-01
	200000.	0.194	0.145	0.820E-01	0.556E-01
N II 3s^{3}P^o-3p^{3}D	5000.	0.379E-02	-0.910E-03	0.315E-02	-0.455E-03
5680.9 Å	10000.	0.639E-02	-0.172E-02	0.438E-02	-0.765E-03
C=0.57 10^{20}	30000.	0.977E-02	-0.324E-02	0.544E-02	-0.122E-02
	50000.	0.108E-01	-0.377E-02	0.589E-02	-0.140E-02
	100000.	0.121E-01	-0.456E-02	0.617E-02	-0.168E-02
	200000.	0.131E-01	-0.533E-02	0.639E-02	-0.197E-02
N II 3s^{3}P^o-3p^{3}S	5000.	0.332E-02	-0.502E-03	0.270E-02	-0.255E-03
5030.2 Å	10000.	0.546E-02	-0.985E-03	0.373E-02	-0.446E-03
C=0.45 10^{20}	30000.	0.817E-02	-0.191E-02	0.458E-02	-0.746E-03
	50000.	0.901E-02	-0.231E-02	0.494E-02	-0.852E-03
	100000.	0.100E-01	-0.277E-02	0.522E-02	-0.102E-02
	200000.	0.107E-01	-0.325E-02	0.535E-02	-0.119E-02
N II 3s^{3}P^o-3p^{3}P	5000.	0.304E-02	-0.143E-03	0.246E-02	-0.750E-04
4624.5 Å	10000.	0.494E-02	-0.300E-03	0.337E-02	-0.143E-03
C=0.36 10^{20}	30000.	0.729E-02	-0.678E-03	0.411E-02	-0.274E-03
	50000.	0.799E-02	-0.861E-03	0.440E-02	-0.332E-03
	100000.	0.884E-02	-0.108E-02	0.462E-02	-0.398E-03
	200000.	0.927E-02	-0.129E-02	0.479E-02	-0.472E-03

Table 1. Continued.

TRANSITION	T[K]	He III W[Å]	d[Å]	B II W[Å]	d[Å]
N II 3s^{3}P^o-4p^{3}D	5000.	0.344E-02	0.797E-03	0.221E-02	0.343E-03
1859.2 Å	10000.	0.450E-02	0.122E-02	0.252E-02	0.497E-03
C=0.21 10^{19}	30000.	0.550E-02	0.183E-02	0.290E-02	0.677E-03
	50000.	0.591E-02	0.206E-02	0.296E-02	0.773E-03
	100000.	0.613E-02	0.246E-02	0.312E-02	0.867E-03
	200000.	0.633E-02	0.265E-02	0.318E-02	0.994E-03
N II 3s^{3}P^o-4p^{3}P	5000.	0.351E-02	0.842E-03	0.224E-02	0.359E-03
1844.6 Å	10000.	0.455E-02	0.128E-02	0.255E-02	0.520E-03
C=0.22 10^{19}	30000.	0.559E-02	0.192E-02	0.291E-02	0.700E-03
	50000.	0.593E-02	0.218E-02	0.298E-02	0.785E-03
	100000.	0.619E-02	0.253E-02	0.319E-02	0.900E-03
	200000.	0.642E-02	0.284E-02	0.320E-02	0.103E-02
N II 3s^{3}P^o-4p^{3}S	5000.	0.359E-02	0.109E-02	0.226E-02	0.466E-03
1834.0 Å	10000.	0.466E-02	0.165E-02	0.259E-02	0.646E-03
C=0.21 10^{19}	30000.	0.576E-02	0.239E-02	0.296E-02	0.884E-03
	50000.	0.617E-02	0.273E-02	0.311E-02	0.987E-03
	100000.	0.661E-02	0.323E-02	0.317E-02	0.115E-02
	200000.	0.720E-02	0.376E-02	0.316E-02	0.129E-02
N II 2p^{23}P-4s^{3}P^o	5000.	0.926E-04	0.129E-03	0.427E-04	0.560E-04
508.7 Å	10000.	0.168E-03	0.195E-03	0.696E-04	0.749E-04
C=0.16 10^{18}	30000.	0.277E-03	0.279E-03	0.105E-03	0.100E-03
	50000.	0.327E-03	0.318E-03	0.120E-03	0.113E-03
	100000.	0.396E-03	0.357E-03	0.133E-03	0.131E-03
	200000.	0.453E-03	0.408E-03	0.164E-03	0.150E-03
N II 2p^{23}P-3d^{3}D^o	5000.	0.454E-04	0.722E-05	0.359E-04	0.363E-05
533.7 Å	10000.	0.725E-04	0.138E-04	0.487E-04	0.618E-05
C=0.44 10^{18}	30000.	0.106E-03	0.261E-04	0.592E-04	0.100E-04
	50000.	0.116E-03	0.308E-04	0.634E-04	0.114E-04
	100000.	0.129E-03	0.370E-04	0.660E-04	0.136E-04
	200000.	0.136E-03	0.446E-04	0.686E-04	0.157E-04
N II 2p^{23}P-3d^{3}P^o	5000.	0.506E-04	0.139E-04	0.391E-04	0.671E-05
529.7 Å	10000.	0.797E-04	0.253E-04	0.524E-04	0.105E-04
C=0.39 10^{18}	30000.	0.117E-03	0.438E-04	0.638E-04	0.161E-04
	50000.	0.128E-03	0.501E-04	0.680E-04	0.184E-04
	100000.	0.144E-03	0.593E-04	0.720E-04	0.222E-04
	200000.	0.153E-03	0.706E-04	0.739E-04	0.249E-04
N II 3p^{3}D-3d^{3}F^o	5000.	0.629E-02	-0.280E-03	0.470E-02	-0.145E-03
5005.9 Å	10000.	0.946E-02	-0.573E-03	0.598E-02	-0.264E-03
C=0.41 10^{20}	30000.	0.129E-01	-0.118E-02	0.720E-02	-0.479E-03
	50000.	0.140E-01	-0.151E-02	0.762E-02	-0.556E-03
	100000.	0.152E-01	-0.181E-02	0.793E-02	-0.670E-03
	200000.	0.158E-01	-0.217E-02	0.801E-02	-0.789E-03

Table 1. Continued.

TRANSITION	T[K]	He III W[Å]	d[Å]	B II W[Å]	d[Å]
N II 3p^{3}D-3d^{3}D^o	5000.	0.602E-02	-0.886E-03	0.447E-02	-0.435E-03
4794.8 Å	10000.	0.904E-02	-0.164E-02	0.566E-02	-0.704E-03
C=0.35 10^{20}	30000.	0.123E-01	-0.296E-02	0.683E-02	-0.109E-02
	50000.	0.134E-01	-0.340E-02	0.718E-02	-0.126E-02
	100000.	0.145E-01	-0.411E-02	0.749E-02	-0.147E-02
	200000.	0.155E-01	-0.477E-02	0.767E-02	-0.170E-02
N II 3p^{3}D-3d^{3}P^o	5000.	0.562E-02	0.715E-04	0.416E-02	0.377E-04
4490.7 Å	10000.	0.836E-02	0.153E-03	0.520E-02	0.749E-04
C=0.28 10^{20}	30000.	0.112E-01	0.381E-03	0.626E-02	0.154E-03
	50000.	0.122E-01	0.489E-03	0.658E-02	0.197E-03
	100000.	0.132E-01	0.649E-03	0.682E-02	0.240E-03
	200000.	0.137E-01	0.777E-03	0.692E-02	0.287E-03
N II 3p^{3}S-3d^{3}P^o	5000.	0.730E-02	0.723E-03	0.536E-02	0.362E-03
5002.2 Å	10000.	0.108E-01	0.137E-02	0.666E-02	0.606E-03
C=0.35 10^{20}	30000.	0.145E-01	0.256E-02	0.803E-02	0.961E-03
	50000.	0.157E-01	0.296E-02	0.840E-02	0.111E-02
	100000.	0.170E-01	0.358E-02	0.876E-02	0.132E-02
	200000.	0.178E-01	0.423E-02	0.893E-02	0.154E-02
N II 3p^{3}P-3d^{3}D^o	5000.	0.101E-01	-0.144E-02	0.740E-02	-0.704E-03
5940.2 Å	10000.	0.150E-01	-0.265E-02	0.923E-02	-0.113E-02
C=0.54 10^{20}	30000.	0.201E-01	-0.474E-02	0.111E-01	-0.175E-02
	50000.	0.219E-01	-0.544E-02	0.117E-01	-0.202E-02
	100000.	0.238E-01	-0.651E-02	0.121E-01	-0.236E-02
	200000.	0.250E-01	-0.754E-02	0.127E-01	-0.274E-02
N II 3p^{3}P-3d^{3}P^o	5000.	0.906E-02	-0.477E-03	0.664E-02	-0.244E-03
5480.3 Å	10000.	0.134E-01	-0.955E-03	0.820E-02	-0.434E-03
C=0.42 10^{20}	30000.	0.177E-01	-0.190E-02	0.987E-02	-0.751E-03
	50000.	0.193E-01	-0.234E-02	0.103E-01	-0.866E-03
	100000.	0.208E-01	-0.281E-02	0.108E-01	-0.103E-02
	200000.	0.214E-01	-0.334E-02	0.109E-01	-0.120E-02
N II 3d^{3}F^o-4p^{3}D	5000.	0.416E-01	0.965E-02	0.262E-01	0.411E-02
6169.8 Å	10000.	0.534E-01	0.147E-01	0.299E-01	0.593E-02
C=0.23 10^{20}	30000.	0.653E-01	0.218E-01	0.340E-01	0.802E-02
	50000.	0.691E-01	0.250E-01	0.348E-01	0.902E-02
	100000.	0.725E-01	0.283E-01	0.369E-01	0.104E-01
	200000.	0.737E-01	0.327E-01	0.370E-01	0.118E-01
N II 3d^{3}D^o-4p^{3}D	5000.	0.467E-01	0.108E-01	0.294E-01	0.460E-02
6523.6 Å	10000.	0.600E-01	0.164E-01	0.336E-01	0.664E-02
C=0.26 10^{20}	30000.	0.734E-01	0.243E-01	0.382E-01	0.898E-02
	50000.	0.776E-01	0.280E-01	0.391E-01	0.101E-01
	100000.	0.815E-01	0.316E-01	0.414E-01	0.116E-01
	200000.	0.827E-01	0.366E-01	0.416E-01	0.132E-01

M.S. Dimitrijević, M.D. Christova and S. Sahal-Bréchot

Table 1. Continued.

		He III		B II	
TRANSITION	T[K]	W[Å]	d[Å]	W[Å]	d[Å]
N II 3d^{3}D^o-4p^{3}P	5000.	0.456E-01	0.109E-01	0.285E-01	0.462E-02
6347.6 Å	10000.	0.583E-01	0.165E-01	0.327E-01	0.661E-02
C=0.26 10^{20}	30000.	0.719E-01	0.242E-01	0.372E-01	0.893E-02
	50000.	0.759E-01	0.277E-01	0.385E-01	0.101E-01
	100000.	0.796E-01	0.317E-01	0.397E-01	0.117E-01
	200000.	0.826E-01	0.363E-01	0.398E-01	0.130E-01
N II 3d^{3}P^o-4p^{3}D	5000.	0.572E-01	0.126E-01	0.360E-01	0.537E-02
7185.8 Å	10000.	0.733E-01	0.192E-01	0.411E-01	0.778E-02
C=0.32 10^{20}	30000.	0.896E-01	0.287E-01	0.467E-01	0.105E-01
	50000.	0.945E-01	0.327E-01	0.478E-01	0.118E-01
	100000.	0.983E-01	0.382E-01	0.509E-01	0.135E-01
	200000.	0.102	0.421E-01	0.508E-01	0.154E-01
N II 3d^{3}P^o-4p^{3}P	5000.	0.555E-01	0.126E-01	0.347E-01	0.538E-02
6972.8 Å	10000.	0.708E-01	0.192E-01	0.397E-01	0.774E-02
C=0.32 10^{20}	30000.	0.870E-01	0.285E-01	0.450E-01	0.105E-01
	50000.	0.916E-01	0.326E-01	0.465E-01	0.118E-01
	100000.	0.963E-01	0.365E-01	0.485E-01	0.134E-01
	200000.	0.982E-01	0.426E-01	0.483E-01	0.155E-01
N II 3d^{3}P^o-4p^{3}S	5000.	0.550E-01	0.156E-01	0.340E-01	0.666E-02
6824.0 Å	10000.	0.700E-01	0.236E-01	0.389E-01	0.922E-02
C=0.29 10^{20}	30000.	0.863E-01	0.340E-01	0.443E-01	0.125E-01
	50000.	0.918E-01	0.388E-01	0.466E-01	0.140E-01
	100000.	0.978E-01	0.454E-01	0.463E-01	0.165E-01
	200000.	0.106	0.530E-01	0.464E-01	0.178E-01

Table 2. Same as in Table 1 but for B III-, and B IV-impact broadening of N II spectral lines.

TRANSITION	T[K]	B III		B IV	
		W[Å]	d[Å]	W[Å]	d[Å]
N II 3s^{1}P^o-3p^{1}P	5000.	0.452E-02	-0.145E-02	0.379E-02	-0.717E-03
6483.8 Å	10000.	0.776E-02	-0.269E-02	0.532E-02	-0.118E-02
C=0.65 10^{20}	30000.	0.121E-01	-0.493E-02	0.667E-02	-0.184E-02
	50000.	0.135E-01	-0.570E-02	0.722E-02	-0.211E-02
	100000.	0.153E-01	-0.682E-02	0.765E-02	-0.252E-02
	200000.	0.164E-01	-0.806E-02	0.802E-02	-0.289E-02
N II 3s^{1}P^o-3p^{1}D	5000.	0.274E-02	0.363E-03	0.214E-02	0.183E-03
3996.1 Å	10000.	0.432E-02	0.702E-03	0.288E-02	0.316E-03
C=0.21 10^{20}	30000.	0.626E-02	0.134E-02	0.350E-02	0.518E-03
	50000.	0.686E-02	0.160E-02	0.374E-02	0.592E-03
	100000.	0.758E-02	0.192E-02	0.388E-02	0.708E-03
	200000.	0.793E-02	0.230E-02	0.405E-02	0.813E-03
N II 3s^{1}P^o-3p^{1}S	5000.	0.324E-02	0.281E-02	0.213E-02	0.120E-02
3438.1 Å	10000.	0.519E-02	0.429E-02	0.286E-02	0.174E-02
C=0.14 10^{20}	30000.	0.800E-02	0.640E-02	0.373E-02	0.236E-02
	50000.	0.915E-02	0.729E-02	0.416E-02	0.270E-02
	100000.	0.112E-01	0.858E-02	0.442E-02	0.301E-02
	200000.	0.119E-01	0.939E-02	0.498E-02	0.348E-02
N II 3s^{1}P^o-4p^{1}P	5000.	0.333E-02	0.587E-04	0.217E-02	0.300E-04
1887.4 Å	10000.	0.438E-02	0.117E-03	0.248E-02	0.532E-04
C=0.15 10^{19}	30000.	0.530E-02	0.232E-03	0.283E-02	0.916E-04
	50000.	0.561E-02	0.285E-03	0.291E-02	0.105E-03
	100000.	0.583E-02	0.341E-03	0.300E-02	0.126E-03
	200000.	0.600E-02	0.409E-03	0.302E-02	0.149E-03
N II 3s^{1}P^o-4p^{1}D	5000.	0.400E-02	0.142E-02	0.242E-02	0.616E-03
1780.6 Å	10000.	0.508E-02	0.215E-02	0.278E-02	0.825E-03
C=0.15 10^{19}	30000.	0.635E-02	0.304E-02	0.315E-02	0.113E-02
	50000.	0.679E-02	0.343E-02	0.330E-02	0.122E-02
	100000.	0.751E-02	0.405E-02	0.339E-02	0.141E-02
	200000.	0.751E-02	0.434E-02	0.374E-02	0.171E-02
N II 3s^{1}P^o-4p^{1}S	5000.	*0.640E-02	*0.457E-02	*0.315E-02	*0.183E-02
1732.4 Å	10000.	*0.827E-02	*0.631E-02	0.377E-02	0.248E-02
C=0.13 10^{19}	30000.	*0.113E-01	*0.915E-02	0.469E-02	0.328E-02
	50000.	0.123E-01	0.102E-01	0.485E-02	0.359E-02
	100000.	0.145E-01	0.112E-01	0.533E-02	0.427E-02
	200000.	0.164E-01	0.124E-01	0.687E-02	0.472E-02
N II 2p^{21}D-3s^{1}P^o	5000.	0.663E-05	0.291E-04	0.534E-05	0.140E-04
747.0 Å	10000.	0.243E-04	0.526E-04	0.138E-04	0.218E-04
C=0.86 10^{18}	30000.	0.741E-04	0.907E-04	0.305E-04	0.335E-04
	50000.	0.971E-04	0.104E-03	0.374E-04	0.386E-04
	100000.	0.122E-03	0.124E-03	0.493E-04	0.453E-04
	200000.	0.160E-03	0.145E-03	0.559E-04	0.511E-04

Table 2. Continued.

		B III		B IV	
TRANSITION	T[K]	W[Å]	d[Å]	W[Å]	d[Å]
N II 2p^2^{1}S-3s^{1}P^o	5000.	0.899E-05	0.384E-04	0.729E-05	0.185E-04
858.4 Å	10000.	0.325E-04	0.695E-04	0.185E-04	0.288E-04
C=0.11 10^{19}	30000.	0.984E-04	0.120E-03	0.406E-04	0.442E-04
	50000.	0.129E-03	0.137E-03	0.498E-04	0.510E-04
	100000.	0.162E-03	0.164E-03	0.655E-04	0.598E-04
	200000.	0.212E-03	0.192E-03	0.741E-04	0.675E-04
N II 2p^2^{1}D-3d^{1}D^o	5000.	0.528E-04	-0.130E-04	0.418E-04	-0.641E-05
582.2 Å	10000.	0.850E-04	-0.241E-04	0.570E-04	-0.104E-04
C=0.30 10^{18}	30000.	0.126E-03	-0.435E-04	0.695E-04	-0.161E-04
	50000.	0.139E-03	-0.500E-04	0.750E-04	-0.185E-04
	100000.	0.155E-03	-0.605E-04	0.788E-04	-0.217E-04
	200000.	0.164E-03	-0.702E-04	0.802E-04	-0.251E-04
N II 2p^2^{1}D-3d^{1}F^o	5000.	0.611E-04	0.773E-05	0.474E-04	0.390E-05
574.7 Å	10000.	0.955E-04	0.149E-04	0.631E-04	0.670E-05
C=0.50 10^{18}	30000.	0.137E-03	0.284E-04	0.765E-04	0.110E-04
	50000.	0.150E-03	0.338E-04	0.815E-04	0.125E-04
	100000.	0.164E-03	0.407E-04	0.852E-04	0.148E-04
	200000.	0.173E-03	0.488E-04	0.877E-04	0.171E-04
N II 2p^2^{1}D-3d^{1}P^o	5000.	0.655E-04	0.198E-04	0.498E-04	0.942E-05
572.1 Å	10000.	0.102E-03	0.352E-04	0.661E-04	0.145E-04
C=0.39 10^{18}	30000.	0.148E-03	0.594E-04	0.805E-04	0.219E-04
	50000.	0.163E-03	0.679E-04	0.859E-04	0.250E-04
	100000.	0.181E-03	0.812E-04	0.891E-04	0.295E-04
	200000.	0.191E-03	0.934E-04	0.957E-04	0.337E-04
N II 2p^2^{1}S-3d^{1}P^o	5000.	0.811E-04	0.244E-04	0.616E-04	0.116E-04
635.2 Å	10000.	0.126E-03	0.435E-04	0.817E-04	0.179E-04
C=0.48 10^{18}	30000.	0.183E-03	0.733E-04	0.994E-04	0.271E-04
	50000.	0.202E-03	0.837E-04	0.106E-03	0.309E-04
	100000.	0.224E-03	0.100E-03	0.110E-03	0.364E-04
	200000.	0.236E-03	0.115E-03	0.118E-03	0.416E-04
N II 3p^{1}P-3d^{1}P^o	5000.	0.443E-02	0.663E-03	0.326E-02	0.323E-03
3920.1 Å	10000.	0.659E-02	0.122E-02	0.406E-02	0.516E-03
C=0.18 10^{20}	30000.	0.885E-02	0.216E-02	0.489E-02	0.795E-03
	50000.	0.963E-02	0.249E-02	0.515E-02	0.910E-03
	100000.	0.105E-01	0.295E-02	0.530E-02	0.108E-02
	200000.	0.109E-01	0.347E-02	0.563E-02	0.126E-02
N II 3p^{1}P-3d^{1}D^o	5000.	0.494E-02	-0.111E-02	0.367E-02	-0.530E-03
4448.3 Å	10000.	0.747E-02	-0.199E-02	0.469E-02	-0.822E-03
C=0.17 10^{20}	30000.	0.104E-01	-0.340E-02	0.569E-02	-0.126E-02
	50000.	0.113E-01	-0.387E-02	0.599E-02	-0.143E-02
	100000.	0.123E-01	-0.468E-02	0.618E-02	-0.168E-02
	200000.	0.130E-01	-0.524E-02	0.660E-02	-0.193E-02

Table 2. Continued.

TRANSITION	T[K]	B III W[Å]	d[Å]	B IV W[Å]	d[Å]
N II 3p^{1}D-3d^{1}D^o	5000.	0.189E-01	-0.615E-02	0.136E-01	-0.288E-02
7764.4 Å	10000.	0.281E-01	-0.102E-01	0.168E-01	-0.425E-02
C=0.53 10^{20}	30000.	0.380E-01	-0.164E-01	0.205E-01	-0.611E-02
	50000.	0.418E-01	-0.188E-01	0.215E-01	-0.696E-02
	100000.	0.454E-01	-0.221E-01	0.224E-01	-0.799E-02
	200000.	0.498E-01	-0.256E-01	0.227E-01	-0.901E-02
N II 3p^{1}D-3d^{1}F^o	5000.	0.146E-01	-0.225E-02	0.106E-01	-0.108E-02
6612.4 Å	10000.	0.214E-01	-0.408E-02	0.129E-01	-0.169E-02
C=0.56 10^{20}	30000.	0.281E-01	-0.704E-02	0.155E-01	-0.259E-02
	50000.	0.307E-01	-0.805E-02	0.162E-01	-0.299E-02
	100000.	0.329E-01	-0.961E-02	0.170E-01	-0.354E-02
	200000.	0.341E-01	-0.113E-01	0.171E-01	-0.394E-02
N II 3p^{1}D-3d^{1}P^o	5000.	0.136E-01	-0.531E-03	0.983E-02	-0.274E-03
6286.1 Å	10000.	0.198E-01	-0.107E-02	0.119E-01	-0.491E-03
C=0.47 10^{20}	30000.	0.257E-01	-0.217E-02	0.143E-01	-0.870E-03
	50000.	0.279E-01	-0.272E-02	0.149E-01	-0.101E-02
	100000.	0.299E-01	-0.326E-02	0.154E-01	-0.121E-02
	200000.	0.307E-01	-0.393E-02	0.159E-01	-0.139E-02
N II 3p^{1}S-3d^{1}P^o	5000.	0.272E-01	-0.390E-02	0.194E-01	-0.187E-02
8441.1 Å	10000.	0.393E-01	-0.702E-02	0.233E-01	-0.290E-02
C=0.84 10^{20}	30000.	0.507E-01	-0.120E-01	0.279E-01	-0.446E-02
	50000.	0.549E-01	-0.137E-01	0.290E-01	-0.508E-02
	100000.	0.591E-01	-0.165E-01	0.304E-01	-0.593E-02
	200000.	0.621E-01	-0.187E-01	0.305E-01	-0.683E-02
N II 3d^{1}D^o-4p^{1}P	5000.	0.456E-01	0.437E-02	0.292E-01	0.205E-02
6631.6 Å	10000.	0.588E-01	0.728E-02	0.333E-01	0.303E-02
C=0.19 10^{20}	30000.	0.713E-01	0.117E-01	0.379E-01	0.434E-02
	50000.	0.750E-01	0.134E-01	0.391E-01	0.496E-02
	100000.	0.785E-01	0.157E-01	0.397E-01	0.579E-02
	200000.	0.801E-01	0.182E-01	0.405E-01	0.636E-02
N II 3d^{1}D^o-4p^{1}D	5000.	0.409E-01	0.148E-01	0.244E-01	0.638E-02
5476.8 Å	10000.	0.514E-01	0.222E-01	0.281E-01	0.856E-02
C=0.14 10^{20}	30000.	0.647E-01	0.320E-01	0.321E-01	0.115E-01
	50000.	0.699E-01	0.365E-01	0.337E-01	0.130E-01
	100000.	0.735E-01	0.408E-01	0.361E-01	0.148E-01
	200000.	0.784E-01	0.471E-01	0.374E-01	0.170E-01
N II 3d^{1}F^o-4p^{1}D	5000.	0.536E-01	0.180E-01	0.320E-01	0.783E-02
6244.1 Å	10000.	0.670E-01	0.273E-01	0.368E-01	0.105E-01
C=0.18 10^{20}	30000.	0.837E-01	0.387E-01	0.416E-01	0.144E-01
	50000.	0.897E-01	0.443E-01	0.437E-01	0.157E-01
	100000.	0.965E-01	0.513E-01	0.451E-01	0.179E-01
	200000.	0.101	0.567E-01	0.485E-01	0.213E-01

Table 2. Continued.

		B III		B IV	
TRANSITION	T[K]	W[Å]	d[Å]	W[Å]	d[Å]
N II 3d^{1}P^o-4p^{1}P	5000.	0.731E-01	0.407E-02	0.466E-01	0.194E-02
8298.5 Å	10000.	0.939E-01	0.726E-02	0.532E-01	0.299E-02
C=0.30 10^{20}	30000.	0.114	0.123E-01	0.604E-01	0.453E-02
	50000.	0.120	0.140E-01	0.623E-01	0.518E-02
	100000.	0.124	0.168E-01	0.629E-01	0.611E-02
	200000.	0.127	0.191E-01	0.644E-01	0.704E-02
N II 3d^{1}P^o-4p^{1}D	5000.	0.596E-01	0.204E-01	0.355E-01	0.883E-02
6566.0 Å	10000.	0.746E-01	0.308E-01	0.409E-01	0.119E-01
C=0.20 10^{20}	30000.	0.937E-01	0.439E-01	0.466E-01	0.162E-01
	50000.	0.999E-01	0.503E-01	0.489E-01	0.178E-01
	100000.	0.105	0.576E-01	0.506E-01	0.203E-01
	200000.	0.113	0.647E-01	0.535E-01	0.240E-01
N II 3d^{1}P^o-4p^{1}S	5000.	*0.786E-01	*0.545E-01	*0.391E-01	*0.219E-01
5955.9 Å	10000.	*0.102	*0.756E-01	0.464E-01	0.295E-01
C=0.16 10^{20}	30000.	*0.137	*0.109	0.574E-01	0.391E-01
	50000.	0.149	0.121	0.596E-01	0.432E-01
	100000.	0.173	0.135	0.650E-01	0.511E-01
	200000.	0.194	0.145	0.820E-01	0.556E-01
N II 3s^{3}P^o-3p^{3}D	5000.	0.379E-02	-0.910E-03	0.315E-02	-0.455E-03
5680.9 Å	10000.	0.639E-02	-0.172E-02	0.438E-02	-0.765E-03
C=0.57 10^{20}	30000.	0.977E-02	-0.324E-02	0.544E-02	-0.122E-02
	50000.	0.108E-01	-0.377E-02	0.589E-02	-0.140E-02
	100000.	0.121E-01	-0.456E-02	0.617E-02	-0.168E-02
	200000.	0.131E-01	-0.533E-02	0.639E-02	-0.197E-02
N II 3s^{3}P^o-3p^{3}S	5000.	0.332E-02	-0.502E-03	0.270E-02	-0.255E-03
5030.2 Å	10000.	0.546E-02	-0.985E-03	0.373E-02	-0.446E-03
C=0.45 10^{20}	30000.	0.817E-02	-0.191E-02	0.458E-02	-0.746E-03
	50000.	0.901E-02	-0.231E-02	0.494E-02	-0.852E-03
	100000.	0.100E-01	-0.277E-02	0.522E-02	-0.102E-02
	200000.	0.107E-01	-0.325E-02	0.535E-02	-0.119E-02
N II 3s^{3}P^o-3p^{3}P	5000.	0.304E-02	-0.143E-03	0.246E-02	-0.750E-04
4624.5 Å	10000.	0.494E-02	-0.300E-03	0.337E-02	-0.143E-03
C=0.36 10^{20}	30000.	0.729E-02	-0.678E-03	0.411E-02	-0.274E-03
	50000.	0.799E-02	-0.861E-03	0.440E-02	-0.332E-03
	100000.	0.884E-02	-0.108E-02	0.462E-02	-0.398E-03
	200000.	0.927E-02	-0.129E-02	0.479E-02	-0.472E-03
N II 3s^{3}P^o-4p^{3}D	5000.	0.344E-02	0.797E-03	0.221E-02	0.343E-03
1859.2 Å	10000.	0.450E-02	0.122E-02	0.252E-02	0.497E-03
C=0.21 10^{19}	30000.	0.550E-02	0.183E-02	0.290E-02	0.677E-03
	50000.	0.591E-02	0.206E-02	0.296E-02	0.773E-03
	100000.	0.613E-02	0.246E-02	0.312E-02	0.867E-03
	200000.	0.633E-02	0.265E-02	0.318E-02	0.994E-03

Table 2. Continued.

TRANSITION	T[K]	B III W[Å]	d[Å]	B IV W[Å]	d[Å]
N II 3s^{3}P^o-4p^{3}P	5000.	0.351E-02	0.842E-03	0.224E-02	0.359E-03
1844.6 Å	10000.	0.455E-02	0.128E-02	0.255E-02	0.520E-03
C=0.22 10^{19}	30000.	0.559E-02	0.192E-02	0.291E-02	0.700E-03
	50000.	0.593E-02	0.218E-02	0.298E-02	0.785E-03
	100000.	0.619E-02	0.253E-02	0.319E-02	0.900E-03
	200000.	0.642E-02	0.284E-02	0.320E-02	0.103E-02
N II 3s^{3}P^o-4p^{3}S	5000.	0.359E-02	0.109E-02	0.226E-02	0.466E-03
1834.0 Å	10000.	0.466E-02	0.165E-02	0.259E-02	0.646E-03
C=0.21 10^{19}	30000.	0.576E-02	0.239E-02	0.296E-02	0.884E-03
	50000.	0.617E-02	0.273E-02	0.311E-02	0.987E-03
	100000.	0.661E-02	0.323E-02	0.317E-02	0.115E-02
	200000.	0.720E-02	0.376E-02	0.316E-02	0.129E-02
N II 2p^{23}P-4s^{3}P^o	5000.	0.926E-04	0.129E-03	0.427E-04	0.560E-04
508.7 Å	10000.	0.168E-03	0.195E-03	0.696E-04	0.749E-04
C=0.16 10^{18}	30000.	0.277E-03	0.279E-03	0.105E-03	0.100E-03
	50000.	0.327E-03	0.318E-03	0.120E-03	0.113E-03
	100000.	0.396E-03	0.357E-03	0.133E-03	0.131E-03
	200000.	0.453E-03	0.408E-03	0.164E-03	0.150E-03
N II 2p^{23}P-3d^{3}D^o	5000.	0.454E-04	0.722E-05	0.359E-04	0.363E-05
533.7 Å	10000.	0.725E-04	0.138E-04	0.487E-04	0.618E-05
C=0.44 10^{18}	30000.	0.106E-03	0.261E-04	0.592E-04	0.100E-04
	50000.	0.116E-03	0.308E-04	0.634E-04	0.114E-04
	100000.	0.129E-03	0.370E-04	0.660E-04	0.136E-04
	200000.	0.136E-03	0.446E-04	0.686E-04	0.157E-04
N II 2p^{23}P-3d^{3}P^o	5000.	0.506E-04	0.139E-04	0.391E-04	0.671E-05
529.7 Å	10000.	0.797E-04	0.253E-04	0.524E-04	0.105E-04
C=0.39 10^{18}	30000.	0.117E-03	0.438E-04	0.638E-04	0.161E-04
	50000.	0.128E-03	0.501E-04	0.680E-04	0.184E-04
	100000.	0.144E-03	0.593E-04	0.720E-04	0.222E-04
	200000.	0.153E-03	0.706E-04	0.739E-04	0.249E-04
N II 3p^{3}D-3d^{3}F^o	5000.	0.629E-02	-0.280E-03	0.470E-02	-0.145E-03
5005.9 Å	10000.	0.946E-02	-0.573E-03	0.598E-02	-0.264E-03
C=0.41 10^{20}	30000.	0.129E-01	-0.118E-02	0.720E-02	-0.479E-03
	50000.	0.140E-01	-0.151E-02	0.762E-02	-0.556E-03
	100000.	0.152E-01	-0.181E-02	0.793E-02	-0.670E-03
	200000.	0.158E-01	-0.217E-02	0.801E-02	-0.789E-03
N II 3p^{3}D-3d^{3}D^o	5000.	0.602E-02	-0.886E-03	0.447E-02	-0.435E-03
4794.8 Å	10000.	0.904E-02	-0.164E-02	0.566E-02	-0.704E-03
C=0.35 10^{20}	30000.	0.123E-01	-0.296E-02	0.683E-02	-0.109E-02
	50000.	0.134E-01	-0.340E-02	0.718E-02	-0.126E-02
	100000.	0.145E-01	-0.411E-02	0.749E-02	-0.147E-02
	200000.	0.155E-01	-0.477E-02	0.767E-02	-0.170E-02

Table 2. Continued.

TRANSITION	T[K]	B III		B IV	
		W[Å]	d[Å]	W[Å]	d[Å]
N II 3p^{3}D-3d^{3}P^o	5000.	0.562E-02	0.715E-04	0.416E-02	0.377E-04
4490.7 Å	10000.	0.836E-02	0.153E-03	0.520E-02	0.749E-04
C=0.28 10^{20}	30000.	0.112E-01	0.381E-03	0.626E-02	0.154E-03
	50000.	0.122E-01	0.489E-03	0.658E-02	0.197E-03
	100000.	0.132E-01	0.649E-03	0.682E-02	0.240E-03
	200000.	0.137E-01	0.777E-03	0.692E-02	0.287E-03
N II 3p^{3}S-3d^{3}P^o	5000.	0.730E-02	0.723E-03	0.536E-02	0.362E-03
5002.2 Å	10000.	0.108E-01	0.137E-02	0.666E-02	0.606E-03
C=0.35 10^{20}	30000.	0.145E-01	0.256E-02	0.803E-02	0.961E-03
	50000.	0.157E-01	0.296E-02	0.840E-02	0.111E-02
	100000.	0.170E-01	0.358E-02	0.876E-02	0.132E-02
	200000.	0.178E-01	0.423E-02	0.893E-02	0.154E-02
N II 3p^{3}P-3d^{3}D^o	5000.	0.101E-01	-0.144E-02	0.740E-02	-0.704E-03
5940.2 Å	10000.	0.150E-01	-0.265E-02	0.923E-02	-0.113E-02
C=0.54 10^{20}	30000.	0.201E-01	-0.474E-02	0.111E-01	-0.175E-02
	50000.	0.219E-01	-0.544E-02	0.117E-01	-0.202E-02
	100000.	0.238E-01	-0.651E-02	0.121E-01	-0.236E-02
	200000.	0.250E-01	-0.754E-02	0.127E-01	-0.274E-02
N II 3p^{3}P-3d^{3}P^o	5000.	0.906E-02	-0.477E-03	0.664E-02	-0.244E-03
5480.3 Å	10000.	0.134E-01	-0.955E-03	0.820E-02	-0.434E-03
C=0.42 10^{20}	30000.	0.177E-01	-0.190E-02	0.987E-02	-0.751E-03
	50000.	0.193E-01	-0.234E-02	0.103E-01	-0.866E-03
	100000.	0.208E-01	-0.281E-02	0.108E-01	-0.103E-02
	200000.	0.214E-01	-0.334E-02	0.109E-01	-0.120E-02
N II 3d^{3}F^o-4p^{3}D	5000.	0.416E-01	0.965E-02	0.262E-01	0.411E-02
6169.8 Å	10000.	0.534E-01	0.147E-01	0.299E-01	0.593E-02
C=0.23 10^{20}	30000.	0.653E-01	0.218E-01	0.340E-01	0.802E-02
	50000.	0.691E-01	0.250E-01	0.348E-01	0.902E-02
	100000.	0.725E-01	0.283E-01	0.369E-01	0.104E-01
	200000.	0.737E-01	0.327E-01	0.370E-01	0.118E-01
N II 3d^{3}D^o-4p^{3}D	5000.	0.467E-01	0.108E-01	0.294E-01	0.460E-02
6523.6 Å	10000.	0.600E-01	0.164E-01	0.336E-01	0.664E-02
C=0.26 10^{20}	30000.	0.734E-01	0.243E-01	0.382E-01	0.898E-02
	50000.	0.776E-01	0.280E-01	0.391E-01	0.101E-01
	100000.	0.815E-01	0.316E-01	0.414E-01	0.116E-01
	200000.	0.827E-01	0.366E-01	0.416E-01	0.132E-01
N II 3d^{3}D^o-4p^{3}P	5000.	0.456E-01	0.109E-01	0.285E-01	0.462E-02
6347.6 Å	10000.	0.583E-01	0.165E-01	0.327E-01	0.661E-02
C=0.26 10^{20}	30000.	0.719E-01	0.242E-01	0.372E-01	0.893E-02
	50000.	0.759E-01	0.277E-01	0.385E-01	0.101E-01
	100000.	0.796E-01	0.317E-01	0.397E-01	0.117E-01
	200000.	0.826E-01	0.363E-01	0.398E-01	0.130E-01

Table 2. Continued.

TRANSITION	T[K]	B III		B IV	
		W[Å]	d[Å]	W[Å]	d[Å]
N II 3d^{3}P^o-4p^{3}D	5000.	0.572E-01	0.126E-01	0.360E-01	0.537E-02
7185.8 Å	10000.	0.733E-01	0.192E-01	0.411E-01	0.778E-02
C=0.32 10^{20}	30000.	0.896E-01	0.287E-01	0.467E-01	0.105E-01
	50000.	0.945E-01	0.327E-01	0.478E-01	0.118E-01
	100000.	0.983E-01	0.382E-01	0.509E-01	0.135E-01
	200000.	0.102	0.421E-01	0.508E-01	0.154E-01
N II 3d^{3}P^o-4p^{3}P	5000.	0.555E-01	0.126E-01	0.347E-01	0.538E-02
6972.8 Å	10000.	0.708E-01	0.192E-01	0.397E-01	0.774E-02
C=0.32 10^{20}	30000.	0.870E-01	0.285E-01	0.450E-01	0.105E-01
	50000.	0.916E-01	0.326E-01	0.465E-01	0.118E-01
	100000.	0.963E-01	0.365E-01	0.485E-01	0.134E-01
	200000.	0.982E-01	0.426E-01	0.483E-01	0.155E-01
N II 3d^{3}P^o-4p^{3}S	5000.	0.550E-01	0.156E-01	0.340E-01	0.666E-02
6824.0 Å	10000.	0.700E-01	0.236E-01	0.389E-01	0.922E-02
C=0.29 10^{20}	30000.	0.863E-01	0.340E-01	0.443E-01	0.125E-01
	50000.	0.918E-01	0.388E-01	0.466E-01	0.140E-01
	100000.	0.978E-01	0.454E-01	0.463E-01	0.165E-01
	200000.	0.106	0.530E-01	0.464E-01	0.178E-01

References

Albert, D., Antony, B. K., Ba, Y. A., et al., A Decade with VAMDC: Results and Ambitions. 2020, *Atoms*, **8**, 76, `DOI:10.3390/atoms8040076`

Belloni, F., Multiplication Processes in High-Density H-^{11}B Fusion Fuel. 2022, *Laser and Particle Beams*, **2022**, 3952779, `DOI:10.1155/2022/3952779`

Cirrone, G. A. P., Manti, L., Margarone, D., et al., First experimental proof of Proton Boron Capture Therapy (PBCT) to enhance proton therapy effectiveness. 2018, *Scientific Reports*, **8**, 1141, `DOI:10.1038/s41598-018-19258-5`

Dimitrijević, M. S. & Sahal-Bréchot, S., Stark broadening of neutral helium lines. 1984, *Journal of Quantitiative Spectroscopy and Radiative Transfer*, **31**, 301, `DOI:10.1016/0022-4073(84)90092-X`

Dubernet, M. L., Antony, B. K., Ba, Y. A., et al., The virtual atomic and molecular data centre (VAMDC) consortium. 2016, *Journal of Physics B Atomic Molecular Physics*, **49**, 074003, `DOI:10.1088/0953-4075/49/7/074003`

Dubernet, M. L., Boudon, V., Culhane, J. L., et al., Virtual atomic and molecular data centre. 2010, *Journal of Quantitiative Spectroscopy and Radiative Transfer*, **111**, 2151, `DOI:10.1016/j.jqsrt.2010.05.004`

Fleurier, C., Sahal-Bréchot, S., & Chapelle, J., Stark profiles of some ion lines of alkaline earth elements. 1977, *Journal of Quantitiative Spectroscopy and Radiative Transfer*, **17**, 595, `DOI:10.1016/0022-4073(77)90019-X`

Giuffrida, L., Margarone, D., Cirrone, G. A. P., et al., Prompt gamma ray diagnostics and enhanced hadron-therapy using neutron-free nuclear reactions. 2016, *AIP Advances*, **6**, 105204, `DOI:10.1063/1.4965254`

Hegelich, B. M., Labun, L., Labun, O. Z., Mehlhorn, T. A., & Batani, D., Photon and Neutron Production as In Situ Diagnostics of Proton-Boron Fusion. 2023, *Laser and Particle Beams*, **2023**, 6924841, `DOI:10.1155/2023/6924841`

Kramida, A., Yu. Ralchenko, Reader, J., & and NIST ASD Team. 2021, NIST Atomic Spectra Database (ver. 5.9), [Online]. Available: `https://physics.nist.gov/asd` [2022, September 7]. National Institute of Standards and Technology, Gaithersburg, MD.

Moore, C. E. 1993, *Tables of Spectra of Hydrogen, Carbon, Nitrogen, and Oxygen Atoms and Ions*

Sahal-Bréchot, S., Impact Theory of the Broadening and Shift of Spectral Lines due to Electrons and Ions in a Plasma. 1969a, *Astronomy and Astrophysics*, **1**, 91

Sahal-Bréchot, S., Impact Theory of the Broadening and Shift of Spectral Lines due to Electrons and Ions in a Plasma (Continued). 1969b, *Astronomy and Astrophysics*, **2**, 322

Sahal-Bréchot, S., The Semiclassical Limit of the Gailitis Formula Applied to Electron Impact Broadening of Spectral Lines of Ionized Atoms. 2021, *Atoms*, **9**, 29, DOI: 10.3390/atoms9020029

Sahal-Bréchot, S., Dimitrijević, M., & Ben Nessib, N., Widths and Shifts of Isolated Lines of Neutral and Ionized Atoms Perturbed by Collisions With Electrons and Ions: An Outline of the Semiclassical Perturbation (SCP) Method and of the Approximations Used for the Calculations. 2014, *Atoms*, **2**, 225, DOI: 10.3390/atoms2020225

Sahal-Bréchot, S., Dimitrijević, M. S., Moreau, N., & Ben Nessib, N., The STARK-B database VAMDC node: a repository for spectral line broadening and shifts due to collisions with charged particles. 2015, *Physica Scripta*, **90**, 054008, DOI:10.1088/0031-8949/90/5/054008

Schollmeier, M. S., Shirvanyan, V., Capper, C., et al., Investigation of Proton Beam-Driven Fusion Reactions Generated by an Ultra-Short Petawatt-Scale Laser Pulse. 2022, *Laser and Particle Beams*, **2022**, 2404263, DOI:10.1155/2022/2404263

Yoon, D.-K., Jung, J.-Y., & Suh, T. S., Application of proton boron fusion reaction to radiation therapy: A Monte Carlo simulation study. 2014, *Applied Physics Letters*, **105**, 223507, DOI:10.1063/1.4903345

Electron energy loss spectra of magnesium in autoionization region

M.S. Rabasović[1] , **B. Predojević**[2], **D. Šević**[1] and

B.P. Marinković[1]

[1] *Institute of Physics Belgrade, Pregrevica 118, 11080 Belgrade, Serbia*
(E-mail: bratislav.marinkovic@ipb.ac.rs)
[2] *Faculty of Natural Sciences, University of Banja Luka, 78000 Banja Luka,*
Republic of Srpska, Bosnia and Herzegovina

Abstract. An experimental study of the autoionization spectra of magnesium by electron impact is given. Electron impact excitation of neutral magnesium atoms above the ionization limit leads to the states that auto-ionize. Energy loss spectra up to 12 eV are recorded at impact electron energies of 30 and 40 eV and scattering angles of 6 and 10 degrees. The two features at 10.09 and 10.46 eV we assigned to the 3s3d $^1D_2$ and 3s3d $^3D_{1,2,3}$ states.
Key words: Electronic spectroscopy – Autoionization – Electron impact excitation – Atomic data

1. Introduction

Magnesium is an element of significant astrophysical importance. Its significant abundance, combined with its array of spectral features across the UV, visual, and IR spectrum, means that it is observable in stars of all spectral types and even in the most metal-poor stars. The abundances of magnesium and other elements were reviewed by Suess & Urey (1956) who also gave the constraints based on different theories of the formation of the elements. The cosmic evolution of magnesium with its three stable isotopes (^{24}Mg, ^{25}Mg, ^{26}Mg) and their evolution after production in massive and intermediate-mass stars was followed by Vangioni & Olive (2019). Magnesium abundance measured in stars have, in recent years, served as a key tracer of Galactic chemical evolution (Fuhrmann (1998); Weinberg et al. (2019)), benefiting from data for hundreds of thousands of stars from the Apache Point Observatory Galactic Evolution Experiment (APOGEE - Abdurro'uf et al. (2022)) and Galactic Archelogy with Hermes (GALAH - Buder et al. (2021)) surveys.

For the particular study, spectral lines are selected based on the spectral type of the star. The optically thin Mg emission line at 880.7 nm from the transition 3s3p $^1P_1 \leftarrow$ 3s3d $^1D_2$ is utilized to track the level of chromospheric

activity in active pre-main sequence stars Yamashita et al. (2024). Infrared Mg lines are used for precise observations of polarization in Solar emission Chang (1987). Esteva & Mehlman (1974) identified 24 resonances in neutral magnesium absorption spectra that belong to autoionization lines.

In the Laboratory for Atomic Collisions Processes at the Institute of Physics Belgrade there have been many studies of electron interactions with metal atom vapors Marinković et al. (2007) and in particular with Mg atom. Studies include elastic electron scattering Predojević et al. (2007), differential cross sections for excitations of the 3s3p $^1P_1$ Filipović et al. (2006), the 3s3p $^3P_1$ Predojević et al. (2011) and the 3s4s $^1S_0$, 3s3d $^1D_2$ and 3s4p $^1P_1$ Predojević et al. (2008) states. Autoionizing levels have been studied for Zn atom Predojević B. et al. (2004) and for Bi atom Marinković et al. (2008).

Most recently, the study of elastic electron scattering from magnesium atom below 1 keV impact energy have been done by Adibzadeh et al. (2024). They employed a semi-empirical approach in order to calculate elastic differential cross sections, integrated and momentum transfer cross sections. The comprehensive calculations of excitation cross sections of states below the first ionization limit have been performed by Gedeon et al. (1999). Calculations for the electron impact ionization of the Mg ground state leading to $Mg^+(3s)$ and $Mg^+(3p)$ were performed by Bartschat et al. (2007). Fung & Yih (2001) have measured the absolute photoabsorption cross sections in the wide spectral range that also covers the autoionizing series $3pns$ $^{1,3}P_1$ and $3pnd$ $^1P_1$.

Here we present autoionizing energy loss spectra of the magnesium atom at electron impact energies of $E_0 = 30$ and 40 eV and scattering angles of 6°and 10°. The first ionization limit of Mg is 7.646 eV with the ground cation state 3s $^2S_{1/2}$. The autoionizing spectra are presented from the ionization limit up to 12 eV energy loss.

2. Experimental method

For the experiments of electron collisions with metal atom vapors we have used a specially designed electron spectrometer that is presented elsewhere in greater detail Panajotović et al. (2004); Marinković et al. (2007), so here it will be just briefly presented. It consists of thoroughly covered units of the monochromator and analyzer based on hemispherical energy selectors. The source of electrons is a thoriated hairpin cathode that is brought to the potential of the desired electron impact energy with respect to the grounded vacuum chamber and the last exit electrode. All electrodes are made of oxygen-free high-conductivity gold-plated copper making three or four electrode electrostatic lenses. The hemispheres are made of molybdenum with the mean radius of 49.8 mm. A single channeltron is used as an electron detector. The angular range of the rotating analyzer is from −30° to +150°.

An effusive beam of magnesium atom vapor is produced by non-magnetic stainless steel oven of Knudsen type. It ends with the cylindrical channel that has an aspect ratio of $\gamma = 0.075$. The oven is filled with 99.9% pure magnesium granules. The oven bottom temperature was about 780 K, while the exit nozzle was 50 K higher. This temperature is higher than that used for measurements of magnesium spectra below ionization limit due to requirements for high-intensity atomic beam. That results in the occurrence of the double scattering features in the spectra.

The energy resolution of the energy loss spectra was 65 meV. The energy scale is calibrated by the position of the most pronounced peak in the spectrum, i.e. the $3s3p\,^1P_1$ state excitation at 4.346 eV.

3. Results and discussion

In Figure 1 we present the energy loss spectra of the neutral magnesium atom at the impact electron energy $E_0 = 30$ eV and the scattering angle $10°$, and in Figure 2 at $E_0 = 40$ eV and $6°$. This covers the region of autoionization states, from the ionization threshold up to 12 eV. The observerd autoionizing states are presented in Table 1 together with the energy level list from NIST database Kramida et al. (2024). All these autoionizing states come from the simultaneous excitation of two s electrons to the higher orbitals. The first observed state is assigned as $3p^2\,^1S_0$ states, while the other states are of the $3pnl$ symmetry where l orbitals are s, p, d and n=3-7. The second ionization Mg^+ limit is doublet $3p$ $^2P_{1/2,3/2}$ at 12.069 and 12.080, respectively.

All autoionizing states that come from the excitation of the inner-shell orbital, $2p$, may be shown in the electron energy loss spectra above 54.8 eV. In the absorption spectrum, they have first been identified by Newsom (1971) and calculated by Mansfield & Connerade (1972). Kim & Tayal (2000) have calculated the photoionization cross sections and resonances of the ground state atomic magnesium to the $Mg^+(3s)$ and $Mg^+(4p)$ thresholds using the variational R-matrix method and the multichannel quantum defect theory. Their values for the $Mg^+(3s)$ levels are also presented in Table 1.

Mg autoionizing levels and Auger transitions were measured by Pejčev et al. (1977) using ejected electron spectroscopy. They exploited electrons of incident energy from 62 to 400 eV and observed ejected electrons at $75°$ with respect to an incident electron beam. The autoionizing states of neutral magnesium were recorded in the energy range from 35 to 50 eV, while for the Mg cation the excited ion state energies were from 57 to 74 eV. Rassi et al. (1977) also measured with high resolution ejected electron spectra of magnesium autoionizing levels that come from the two-electron excitation assigned as $1s^2 2s^2 2p^6 3pnl$ by low-energy electron impact. They were able to identify eight levels assigned as $3pns\,^1P$ n=4-11, two levels $3pnd\,^1P$ n=3,4, five levels $3pns\,^3P$ n=4-8, five levels $3pnd\,^1F$ n=3-7, three levels $3pnd\,^1D$ n=3-5, six levels $3pnp\,^1S$ n=3-8, nine lev-
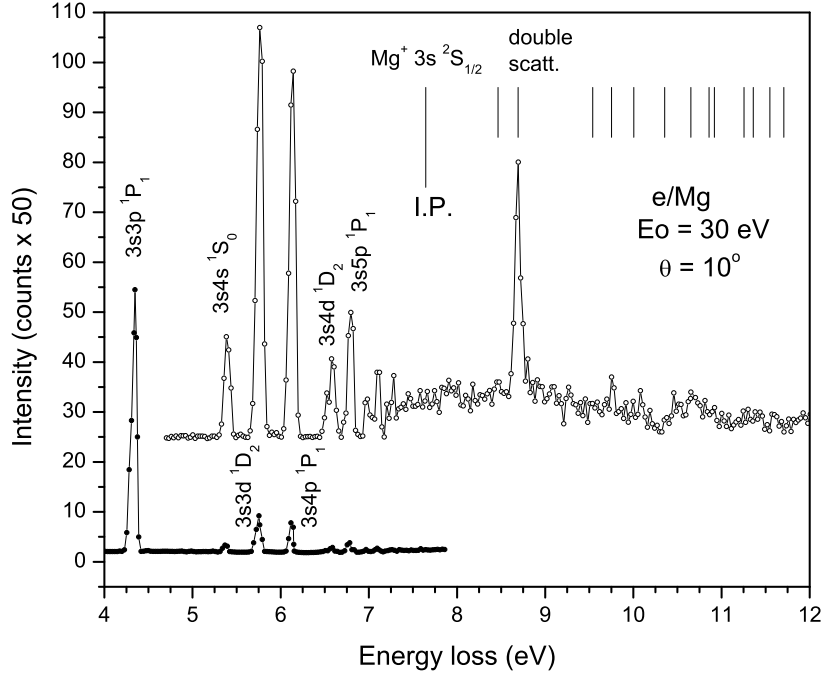
Figure 1. Energy loss at impact energy of $E_0 = 30$ eV and scattering angle of $10°$. Vertical lines designate positions of autoionization energies according Kramida et al. (2024) and values are listed in Table 1.

els $3pnp$ ^1D n=4-12 and two levels $3pnp$ ^3P n=4,5. Tabulated energies of these series of autoionizing states from 8.45 eV to the ionizing limit Mg^+ $3p$ $^2P_{1/2}$ can be found in Rassi et al. (1977). The same group of authors has extended the measurements of autoionizing states up to the next ionization limit $Mg^+(4s$ $^2S_{1/2})$ at 16.3 eV.

Trajmar & Williams (1976) provided a series of metal atom cross sections and also examined the autoionization region of the Mg atom. They made a comprehensive review of many atomic metals and gave trends in energy dependencies of cross sections. The energy range of the Mg energy loss spectrum is given from 5 to 19 eV, thus covering both regions, below and above the first ionization limit.

In the spectrum at $E_0 = 40$ eV and the scattering angle of $6°$ two features are distinctive and we attribute them as $^1D_2$ and $^3D_{1,2,3}$ states. The energies of these states are 10.09 and 10.46 eV, respectively, while the NIST data are 10.005 and 10.355 eV. The singlet-triplet splitting is in both cases the same, 350 meV. The assignment of the spectral features is obscured by the presence
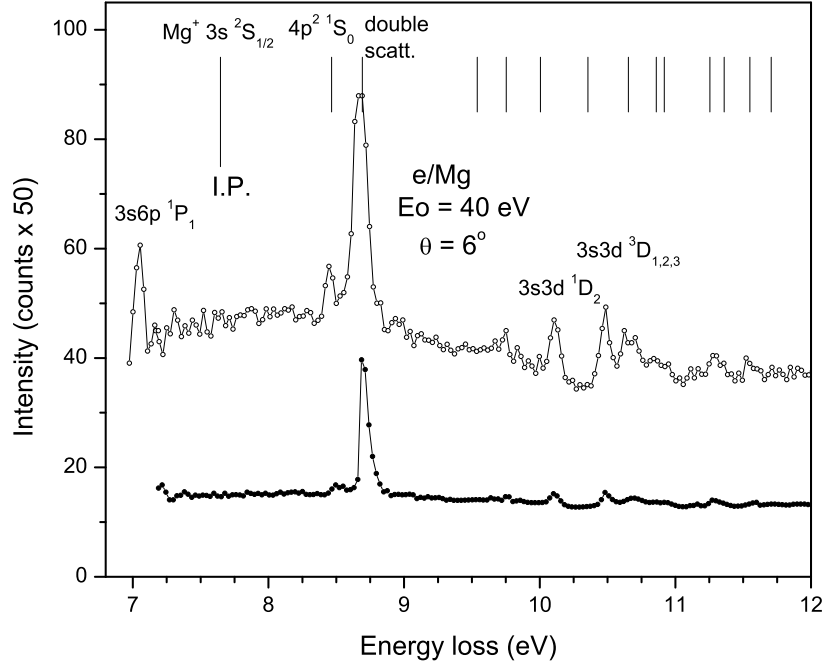
Figure 2. Energy loss at impact energy of $E_0 = 40$ eV and scattering angle of $6°$.

of the 3p3d ^1F and 3p4d ^1F levels found by Rassi et al. (1977) at 10.03 and 10.44 eV, respectively. The levels of F symmetry have not been recorded in the NIST data tables. The sum of the ionization energy and the energy of ejected electrons found by Rassi et al. (1977) correspond to the observed energies of the autoionizing states in our energy loss spectra.

4. Conclusions

The Mg autoionizing states between two ionization limits, the $Mg^+(3s\ ^2S_{1/2})$ at 7.646 eV and $Mg^+(3p\ ^2P_{1/2})$ at 12.069 eV have been recorded by electron energy loss spectroscopy at $E_0 = 30$ eV and the scattering angle $10°$, and $E_0 = 40$ eV and $6°$. The autoionizing states are identified as two-electron excited states of the type $3pnl$. In all spectra the double scattering feature of the most intense peak in magnesium energy loss, 3s3p $^1P_1$, is recorded at 8.69 eV. The two features at 10.09 and 10.46 eV we assigned to the 3s3d $^1D_2$ and 3s3d $^3D_{1,2,3}$ states. This assignment needs further studies in order to resolve the contributions of the 3p3d ^1F and 3p4d ^1F levels observed previously by Rassi et al. (1977).

Table 1. Observed energies of autoionization states, their energies in NIST table Kramida et al. (2024), calculated resonances by Kim & Tayal (2000) and assignment.

energy present	energy NIST	energy Kim & Tayal (2000)	assignment
8.45 ± 0.03	8.465	-	$3p^2 \ ^1S_o$
8.79	-	-	double scattering
-	9.539	-	$3p4s \ ^3P_1$
9.74 ± 0.03	9.753	9.706	$3p4s \ ^1P_1$
10.09 ± 0.03	10.005	-	$3p3d \ ^1D_2$
10.46 ± 0.03	10.354, 10.355, 10.357	-	$3p3d \ ^3D_{1,2,3}$
10.65 ± 0.03	10.653	10.651	$3p3d \ ^1P_1$
10.83 ± 0.03	10.859	-	$3p5s \ ^3P_1$
10.91 ± 0.03	10.918	10.922	$3p5s \ ^1P_1$
11.26 ± 0.03	11.255	11.247	$3p4d \ ^1P_1$
11.36 ± 0.03	11.359, 11.387	-	$3p4d \ ^{3,1}P_1$
11.57 ± 0.03	11.549	11.538	$3p5d \ ^1P_1$
-	11.597, 11.615	11.610	$3p7s \ ^{3,1}P_1$
11.70 ± 0.03	11.707	11.698	$3p6d \ ^1P_1$

Presented data is of interest for astrophysical and plasma communities as well as for our fundamental knowledge of autoionization processes and atomic energy level structure.

References

Abdurro'uf, Accetta, K., Aerts, C., et al., The Seventeenth Data Release of the Sloan Digital Sky Surveys: Complete Release of MaNGA, MaStar, and APOGEE-2 Data. 2022, *The Astrophysical Journal Supplement Series*, **259**, 35, DOI:10.3847/1538-4365/ac4414

Adibzadeh, M., Theodosiou, C. E., & Harmon, N. J., Elastic Electron Scattering from Be, Mg, and Ca. 2024, *Atoms*, **12**, DOI:10.3390/atoms12060033

Bartschat, K., Weflen, D., & Guan, X., Electron-impact ionization of magnesium. 2007, *Journal of Physics B: Atomic, Molecular and Optical Physics*, **40**, 3231, DOI: 10.1088/0953-4075/40/16/004

Buder, S., Sharma, S., Kos, J., et al., The GALAH+ survey: Third data release. 2021, *Monthly Notices of the Royal Astronomical Society*, **506**, 150, DOI:10.1093/mnras/stab1242

Chang, E. S., Solar Emission Lines Revisited: Extended Study of Magnesium. 1987, *Physica Scripta*, **35**, 792, DOI:10.1088/0031-8949/35/6/006

Esteva, J. M. & Mehlman, G., Autoionization Spectra of Magnesium (Mg i, MG ii, and MG Iii) in the 50- to 110-eV Energy Range. 1974, *Astrophysical Journal*, **193**, 747, DOI:10.1086/153214

Filipović, D. M., Predojević, B., Pejčev, V., et al., Electron scattering by magnesium: excitation of the 3s3p $^1P_1$ state. 2006, *Journal of Physics B: Atomic, Molecular and Optical Physics*, **39**, 2583, DOI:10.1088/0953-4075/39/11/021

Fuhrmann, K., Nearby stars of the Galactic disk and halo. 1998, *Astronomy and Astrophysics*, **338**, 161

Fung, H.-S. & Yih, T.-S., The absolute photoabsorption cross section measurement of magnesium in the 75 nm to 162 nm spectral range. 2001, *Nuclear Physics A*, **684**, 696, DOI:10.1016/S0375-9474(01)00465-1, few-Body Problems in Physics

Gedeon, V., Lengyel, V., Zatsarinny, O., & Kocher, C. A., Electron-impact excitation of the Mg atom from the ground and metastable states: R-matrix calculation with pseudostates. 1999, *Phys. Rev. A*, **59**, 2016, DOI:10.1103/PhysRevA.59.2016

Kim, D.-S. & Tayal, S. S., Autoionizing resonances in the photoionization of ground state atomic magnesium. 2000, *Journal of Physics B: Atomic, Molecular and Optical Physics*, **33**, 3235, DOI:10.1088/0953-4075/33/17/306

Kramida, A., Ralchenko, Y., Reader, J., & *etal.*. 2024, NIST atomic spectra database, NIST standard reference database (version 5.12), https://physics.nist.gov/asd, Accessed: 2024-12-29

Mansfield, M. W. D. & Connerade, J. P., Hartree-Fock Calculations of the Mg I Spectrum in the Extreme Ultraviolet. 1972, *Physica Scripta*, **6**, 191, DOI:10.1088/0031-8949/6/4/003

Marinković, B., Filipović, D., Pejčev, V., & Šević, D., Electron-impact excitations of the autoionizing states of bismuth. 2008, *International Journal of Mass Spectrometry*, **271**, 76, DOI:10.1016/j.ijms.2007.09.017, Yong-Ki Kim Honour Issue

Marinković, B., Pejčev, V., Filipović, D., et al., Electron collisions by metal atom vapours. 2007, *Radiation Physics and Chemistry*, **76**, 455, DOI:10.1016/j.radphyschem.2006.01.018, Proceedings of the 3rd International Conference on Elementary Processes in Atomic Systems

Newsom, G. H., Inner-Shell Absorption in the Spectra of the Alkaline Earths. I. Magnesium (Mg I). 1971, *Astrophysical Journal*, **166**, 243, DOI:10.1086/150953

Panajotović, R., Šević, D., Pejčev, V., Filipović, D., & Marinković, B., The ^{1}S–^{1}P electron excitations of Zn at small scattering angles. 2004, *International Journal of Mass Spectrometry*, **233**, 253, DOI:10.1016/j.ijms.2003.12.025, Special Issue: In honour of Tilmann Märk

Pejčev, V., Ottley, T. W., Rassi, D., & Ross, K. J., Ejected-electron spectrum of Mg I and Mg II autoionising levels between 20 and 53 eV excited by low-energy electron impact on magnesium vapour. 1977, *Journal of Physics B: Atomic and Molecular Physics*, **10**, 2389, DOI:10.1088/0022-3700/10/12/018

Predojević B., Šević Dragutin M., Pejčev Vladimir M., Marinković Bratislav P., & Filipović Dušan M., Electron energy-loss spectroscopy of autoionizing states of zinc. 2004, *Serbian Astronomical Journal*, 53, DOI:10.2298/SAJ0469053P

Predojević, B., Pejčev, V., Filipović, D. M., Šević, D., & Marinković, B. P., Elastic electron scattering by a magnesium atom. 2007, *Journal of Physics B: Atomic, Molecular and Optical Physics*, **40**, 1853, DOI:10.1088/0953-4075/40/10/019

Predojević, B., Pejčev, V., Filipović, D. M., Šević, D., & Marinković, B. P., Electron scattering by magnesium: excitation of the 3s4s $^1S_0$, 3s3d $^1D_2$ and 3s4p $^1P_1$ states. 2008, *Journal of Physics B: Atomic, Molecular and Optical Physics*, **41**, 015202, DOI:10.1088/0953-4075/41/1/015202

Predojević, B., Pejčev, V., Filipović, D. M., et al., Electron impact excitation of the 3s3p ^3P state of magnesium from the ground state. 2011, *Journal of Physics B: Atomic, Molecular and Optical Physics*, **44**, 055208, DOI:10.1088/0953-4075/44/5/055208

Rassi, D., Pejcev, V., Ottley, T. W., & Ross, K. J., High-resolution ejected-electron spectrum of magnesium autoionising levels following two-electron excitation by low-energy electron impact. 1977, *Journal of Physics B: Atomic and Molecular Physics*, **10**, 2913, DOI:10.1088/0022-3700/10/14/023

Suess, H. E. & Urey, H. C., Abundances of the Elements. 1956, *Rev. Mod. Phys.*, **28**, 53, DOI:10.1103/RevModPhys.28.53

Trajmar, S. & Williams, W., Electron-metal atom collision cross sections. 1976, in Yugoslav Symposium and Summer School on the Physics of Ionized Gases, Vol. **8**, *Physics of Ionized Gases 1976: Proceedings of Invited Lectures Given at the VIII. International Summer School on the Physics of Ionized Gases, Dubrovnik, Yugoslavia, Aug. 27-Sept. 3, 1976*, ed. B. Navinšek (J. Stefan Institute, University of Ljubljana), 199–215

Vangioni, E. & Olive, K. A., The cosmic evolution of magnesium isotopes. 2019, *Monthly Notices of the Royal Astronomical Society*, **484**, 3561, DOI:10.1093/mnras/stz210

Weinberg, D. H., Holtzman, J. A., Hasselquist, S., et al., Chemical Cartography with APOGEE: Multi-element Abundance Ratios. 2019, *The Astrophysical Journal*, **874**, 102, DOI:10.3847/1538-4357/ab07c7

Yamashita, M., Itoh, Y., & Takagi, Y., Chromospheric Mg I emission lines of pre-main-sequence stars. 2024, *Astronomy and Astrophysics*, **691**, A304, DOI:10.1051/0004-6361/202452025

Modeling optical processes in dense astrophysical and laboratory plasmas: dipole moment and pseudo potential

N.M. Sakan[1] , **V.A. Srećković**[1] , **Z. Simić**[2] **and M. Dechev**[3]

[1] *University of Belgrade, Institute of Physics Belgrade, PO Box 57 (E-mail: nsakan@ipb.ac.rs, vlada@ipb.ac.rs)*

[2] *Astronomical Observatory, Volgina 7, 11060 Belgrade, Serbia (E-mail: zsimic@aob.rs)*

[3] *Institute of Astronomy and National Astronomical Observatory, Bulgarian Academy of Sciences, 72, Tsarigradsko chaussee Blvd. Sofia, Bulgaria (E-mail: mdechev@nao-rozhen.org)*

Abstract. This manuscript deals with aspects of dense plasma behavior and modeling in a cut-off pseudo-potential figure. The method of cut-off pseudo potentials, both Coulomb and Hartree-Fock ones, has been used e.g. in a description of dense astrophysical plasma. Here are presented some of the aspects of the model and analysis of the behavior of dipole moments. The presented results are important for the estimation of the optical properties of moderate and high density hydrogen astrophysical plasma. The behavior of such plasma is also of interest in fusion experiments and various laboratory research.
Key words: astrophysical plasma – fusion plasma – dense plasma – optical characteristics – modeling – stellar atmospheres – dipole approximation

1. Introduction

Both theoretical and experimental studies are interested in the issues of radiative transfer, energy transport, and plasma opacity under moderate and strong non-ideality (van Horn, 1991; Treumann & Baumjohann, 1997; Rogers & Iglesias, 1998; Vitel, 2004; Mihajlov et al., 2011a; Khrapak & Khrapak, 2020). In recent decades, a large number of theoretical and experimental investigations have focused on the strong coupling and density effects in plasma radiation (Kobzev & Popovich, 2013; Remington, 2005; Uzdensky & Rightley, 2014). Moreover, Machine learning (ML) was used in order to estimate plasma parameters and characteristics of such systems (Akçay et al., 2021; Trieschmann et al., 2023). The plasma of the inner layers of the solar atmosphere and partially ionized layers of other stellar atmospheres, such as the atmospheres of DA white dwarfs are taken into consideration (Bodmer & Bochsler, 2000; Srećković et al., 2017; Chabrier et al., 2006; Somov, 2006).

In many-particle systems it is common to make a switch from a variety of particles in a system toward a model particle, the so-called pseudo particle, (Fortov et al., 2006; Mihajlov et al., 2011b; Douis & Meftah, 2013; Srećković et al., 2018). The virtual particle that possesses the average behavior of all of the system particles in a form of averaged one. That behavior is described with the help of averaged, pseudo-potential (see e.g. Ignjatović et al., 2017, and references therein). The usage of pseudo-potentials relaxes a numerical requirement, since the solution methods are simpler than for the system of particles and as such code is capable of running on a desktop computer, e.g. it does not need extensive computing power.

It is well known that Coulomb collisions between charged particles have the ability to transfer energy and cause the plasma to heat or cool. The control of the electron heat flux in the solar wind appears to be influenced by Coulomb collisions (Kalman et al., 2006; Salem et al., 2003). Additionally, the stability or instability of plasma configurations can be influenced by Coulomb forces. For instance, stable or unstable magnetic structures may arise as a result of the equilibrium between Coulomb and magnetic forces. In addition to influencing the transport of charged particles in solar plasma, which can alter their speed and distribution, Coulomb forces can also contribute to the acceleration of particles in solar plasma, as in the case of solar flares or coronal mass ejections (see e.g. Bodmer & Bochsler, 2000; Gordovskyy et al., 2005).

2. Theory

In order to have some adequate representation of the plasma characteristics one of the most common parameters is a non-ideality parameter, Γ, given in simplest form applicable for hydrogen plasma given by

$$\Gamma = \frac{E_{pot}}{E_{kin}} = \frac{q_e^2}{4\pi\varepsilon_0 \langle r \rangle kT_e} = \frac{q_e^2}{4\pi\varepsilon_0 kT_e} \sqrt[3]{\frac{4\pi n_e}{3}}. \tag{1}$$

It presents a ratio of the intrinsic potential energy pf plasma divided by thermal energy, that could be related to the kinetic energy of plasma constituents (Tkachenko et al., 2006; Adamyan et al., 2009; Sakan et al., 2018). Here we are dealing with describing of plasma of mild nonideality, up to strongly nonideal plasma, $0.1 \leq \Gamma \leq 2$.

To calculate the optical properties of plasma the Schroedinger equation that introduces the collective plasma pseudo-potential should be solved (Prandini et al., 2018). For the case of hydrogen atom in plasma the simple form of pseudo-potential, cut-off Coulomb one, possesses the ability to have an analytical solutions in entire radial space as well as all bond as well as free solutions.

$$U_0(r; r_{cut}) = \begin{cases} -\dfrac{e^2}{r} + \dfrac{e^2}{r_{cut}} & : & 0 < r \leq r_{cut} \\ 0 & : & r_{cut} < r \end{cases}, \tag{2}$$

where r_{cut} is cut off radius (see e.g. Mihajlov et al., 2011a).

In later work it has been proven that the Hartree-Fock potential could be used instead of physically more correct Coulomb one. So the potential, could be substituted with the Hartree-Fock one shifted by the average plasma energy $1/r_{cut}$. It also relaxes the numerical complexity of the calculations, and in case of hydrogen the overall relative error is comparable or smaller than $1 \cdot 10^{-7}$.

In dipole approximation, that is valid for high density plasma,the radial part of equation is of interest. By the introduction of the substitution $R(r) = P(r)/r$ it becomes

$$\frac{d^2P}{dr^2} + \left[\frac{2m}{\hbar^2}\left(E - U(r)\right) - \frac{l(l+1)}{r^2}\right] P = 0. \qquad (3)$$
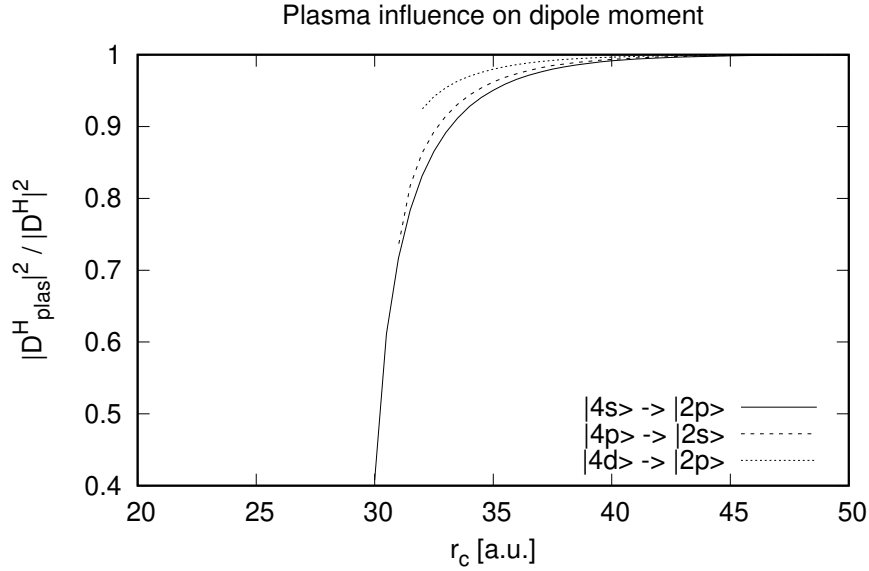
Figure 1. The plasma influence onto dipole matrix element for the transitions from main quantum number $n = 4$ onto states with $n = 2$.

In this contribution, we will present computed quantities, i.e. a dataset, and explain the results and future perspectives.

3. Results and discussion

Here, a behavior of plasma influence onto the dipole matrix elements is discussed. In Fig. 1 a influence of average plasma potential $1/r_c$ on the dipole

matrix element is shown. It could be seen that for the same main quantum number transition, from $n = 4$ to $n = 2$ the From Fig. 2 the influence of the enlarged plasma potential energy, e.g. diminishing of r_c, the influence of plasma is dominant onto the far most outer shell. This is expected behavior, but with the
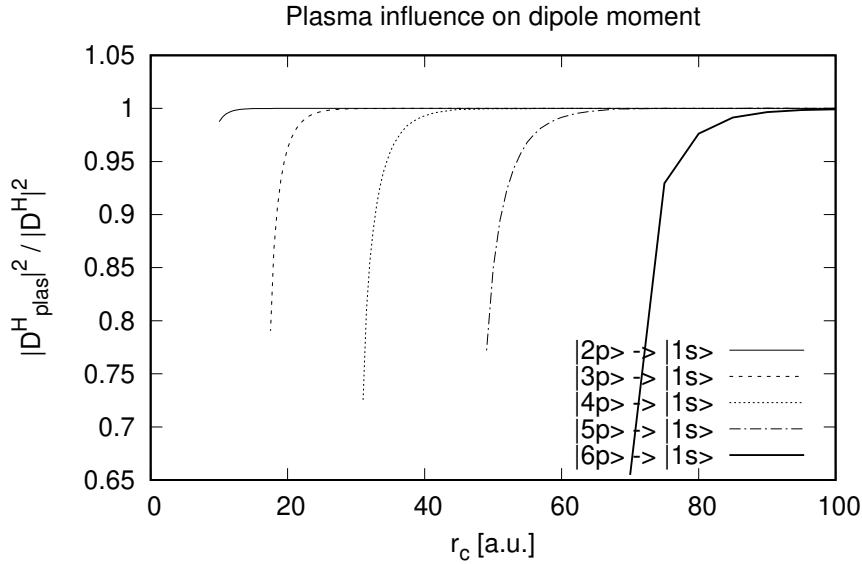
Figure 2. The plasma influence onto dipole matrix element for the transitions onto $1s$ state.

further steps that have been carried out it is expected to have a more adequate pseudo-potential model for describing of plasma influence.

The presented results could show a behavior of the dipole matrix elements inside plasma. As such they could be used as a mark of the real behavior of emitter in plasma. The work on calculating a more adequate pseudo-potentials that could characterize a better plasma influence onto the emitter is in progress. The results presented here could be of interest in describing of hydrogen astrophysical plasma optical properties in area od plasmas of moderate and high non-ideality. The behavior of such plasma is also of interest in fusion experiments and various laboratory research.

4. Final remarks and future work

This work examines dense plasma behavior and modeling in a cut-off pseudo-potential figure. Cut-off pseudopotentials, including Coulomb and Hartree-Fock

models, have been used to describe dense astrophysical plasma. The given results are crucial for estimating the optical characteristics of moderate and high density hydrogen astrophysical plasma. Plasma behavior is relevant to fusion experiments and laboratory research using ML (see e.g. Sakan et al., 2022; Lemishko et al., 2024, and references therein).

The findings and their analysis demonstrate the applications' interdisciplinary nature. This work's perspective and short-term goal is to use machine learning for astrophysical plasma research.

References

Adamyan, V. M., Mihajlov, A. A., Sakan, N. M., Srećković, V. A., & Tkachenko, I. M., The dynamic conductivity of strongly non-ideal plasmas: is the Drude model valid? 2009, *Journal of Physics A Mathematical General*, **42**, 214005, DOI:10.1088/1751-8113/42/21/214005

Akçay, C., Finn, J. M., Brennan, D. P., Burr, T., & Kürkçüoğlu, D. M., Machine learning methods for probabilistic locked-mode predictors in tokamak plasmas. 2021, *Phys. Plasmas*, **28**, DOI:10.1063/5.0053670

Bodmer, R. & Bochsler, P., Influence of Coulomb collisions on isotopic and elemental fractionation in the solar wind acceleration process. 2000, *Journal of Geophysical Research*, **105**, 47, DOI:10.1029/1999JA900434

Chabrier, G., Saumon, D., & Potekhin, A. Y., Dense plasmas in astrophysics: from giant planets to neutron stars. 2006, *J. Phys. A*, **39**, 4411, DOI:10.1088/0305-4470/39/17/S16

Douis, S. & Meftah, M. T., Correlation Function and Electronic Spectral Line Broadening in Relativistic Plasmas. 2013, *Serbian Astronomical Journal*, **186**, 15, DOI:10.2298/SAJ130218002D

Fortov, V., Iakubov, I., & Khrapak, A. 2006, *Physics of Strongly Coupled Plasma*, International Series of Monographs on Physics (OUP Oxford), ISBN: 9780199299805

Gordovskyy, M., Zharkova, V. V., Voitenko, Y. M., & Goossens, M., Proton versus electron heating in solar flares. 2005, *Advances in Space Research*, **35**, 1743, DOI:10.1016/j.asr.2005.07.004

Ignjatović, L., Srećković, V., & Dimitrijević, M., The Screening Characteristics of the Dense Astrophysical Plasmas: The Three-Component Systems. 2017, *Atoms*, **5**, 42, DOI:10.3390/atoms5040042

Kalman, G. J., Rommel, J. M., & Blagoev, K. 2006, *Strongly Coupled Coulomb Systems* (Springer Science & Business Media)

Khrapak, S. A. & Khrapak, A. G., On the conductivity of moderately non-ideal completely ionized plasma. 2020, *Results in Physics*, **17**, 103163, `DOI:10.1016/j.rinp.2020.103163`

Kobzev, G. & Popovich, M. 2013, *Transport and optical properties of nonideal plasma* (Springer Science & Business Media)

Lemishko, K., Armstrong, G. S. J., Mohr, S., et al., Machine learning-based estimator for electron impact ionization fragmentation patterns. 2024, *Journal of Physics D: Applied Physics*

Mihajlov, A. A., Sakan, N. M., Srećković, V. A., & Vitel, Y., Modeling of the Continuous Absorption of Electromagnetic Radiation in Dense Hydrogen Plasma. 2011b, *Baltic Astronomy*, **20**, 604, `DOI:10.1515/astro-2017-0345`

Mihajlov, A. A., Sakan, N. M., Srećković, V. A., & Vitel, Y., Modeling of continuous absorption of electromagnetic radiation in dense partially ionized plasmas. 2011a, *J. Phys. A*, **44**, 095502, `DOI:10.1088/1751-8113/44/9/095502`

Prandini, G., Marrazzo, A., Castelli, I. E., Mounet, N., & Marzari, N., Precision and efficiency in solid-state pseudopotential calculations. 2018, *npj Computational Materials*, **4**, 72, `DOI:10.1038/s41524-018-0127-2`

Remington, B. A., High energy density laboratory astrophysics. 2005, *Plasma Physics and Controlled Fusion*, **47**, A191, `DOI:10.1088/0741-3335/47/5A/014`

Rogers, F. J. & Iglesias, C. A., Opacity of Stellar Matter. 1998, *Space science reviews*, **85**, 61, `DOI:10.1023/A:1005132518820`

Sakan, N. M., Srećković, V. A., Simić, Z. J., & Dimitrijević, M. S., The Application of the Cut-Off Coulomb Model Potential for the Calculation of Bound-Bound State Transitions. 2018, *Atoms*, **6**, `DOI:10.3390/atoms6010004`

Sakan, N. M., Traparić, I., Srećković, V. A., & Ivković, M., The usage of perceptron, feed and deep feed forward artificial neural networks on the spectroscopy data: astrophysical & fusion plasmas. 2022, *Contributions of the Astronomical Observatory Skalnate Pleso*, **52**, 97, `DOI:10.31577/caosp.2022.52.3.97`

Salem, C., Hubert, D., Lacombe, C., et al., Electron Properties and Coulomb Collisions in the Solar Wind at 1 AU: Wind Observations. 2003, *The Astrophysical Journal*, **585**, 1147, `DOI:10.1086/346185`

Somov, B. V. 2006, *Plasma Astrophysics, Part I: Fundamentals and Practice* (Springer New York, NY)

Srećković, V. A., Šulić, D. M., Ignjatović, L. M., & Dimitrijević, M. S., A study of high-frequency properties of plasma and the influence of electromagnetic radiation from IR to XUV. 2017, *Nucl. Techn. & Rad. Protect.*, **32**, 222, `DOI:10.2298/NTRP1703222S`

Srećković, V. A., Sakan, N., Šulić, D., et al., Free–free absorption coefficients and Gaunt factors for dense hydrogen-like stellar plasma. 2018, *Mon. Not. R. Astron. Soc.*, **475**, 1131, `DOI:10.1093/mnras/stx3237`

Tkachenko, I. M., Adamyan, V. M., Mihajlov, A. A., et al., Electrical conductivity of dense non-ideal plasmas in external HF electric field. 2006, *Journal of Physics A Mathematical General*, **39**, 4693, `DOI:10.1088/0305-4470/39/17/S58`

Treumann, R. A. & Baumjohann, W. 1997, *Advanced space plasma physics* (Imperial College Press: London, UK), `DOI:10.1142/p020`

Trieschmann, J., Vialetto, L., & Gergs, T., Review: Machine learning for advancing low-temperature plasma modeling and simulation. 2023, *J. Micro/Nanopatterning Mater. Metrol.*, **22**, 041504, `DOI:10.1117/1.JMM.22.4.041504`

Uzdensky, D. A. & Rightley, S., Plasma physics of extreme astrophysical environments. 2014, *Reports on Progress in Physics*, **77**, 036902, `DOI:0.1088/0034-4885/77/3/036902`

van Horn, H. M., Dense Astrophysical Plasmas. 1991, *Science*, **252**, 384, `DOI:10.1126/science.252.5004.384`

Vitel, Y., Spectra of dense pure hydrogen plasma in Balmer area. 2004, *J. Quant. Spectrosc. Radiat. Transf.*, **83**, 387, `DOI:10.1016/S0022-4073(02)00380-1`

Stark broadening parameters for
6s ^{4}F - 6p ^{4}(D, F, G)^O supermultiplet
of singly ionized Hafnium

Z. Simić[1] [ID]**, M.S. Dimitrijević**[1,2] **and N. Sakan**[3]

[1] *Astronomical Observatory, Volgina 7, 11060 Belgrade, Serbia (E-mail: zsimic@aob.rs)*
[2] *LERMA, Observatoire de Paris, F-92195 Meudon Cedex, France*
[3] *University of Belgrade, Institute of Physics, PO Box 57, 11001 Belgrade, Serbia*

Abstract. Stark broadening parameters - line widths and shifts - are of interest in stellar spectroscopy as well as in laboratory and technological plasmas. Stark widths and shifts have been calculated for 28 Hf II transitions using plasma electron density of $10^{17} \mathrm{cm}^{-3}$ and temperature from 5000K to 80000K as parameters. The calculations were performed according to the simplified modified semiempirical (SMSE) method.
Key words: Stark broadening – line profiles – atomic data

1. Introduction

Insight into impact broadening parameters is of great importance for stellar spectroscopy and laboratory and technological plasma. In this context, stellar abundances must be both precise and accurate in order to obtain reliable information about the stellar atmospheres chemical composition. For example, in metal-poor stars, the strongest and often the only discernible lines of heavy elements are found in ultraviolet (UV) range, from 1000 to 4000 Å and visible blue from 4400 to 4900 Å, Roederer et al. (2012). Absorption lines of interest in these parts of the spectrum are likely to be blended with lines from other sources. To obtain accurate abundances, valid atomic data are necessary, and the electronic level populations in the line-forming layers of the atmosphere must be reliably modeled.

The first determination of the amount of solar hafnium was performed by Russell (1929). The value of A(Hf)=0.90 was surprisingly accurate for the time. In Andersen et al. (1976), the abundance of solar hafnium was redetermined, and reliable transition probabilities for Hf II were obtained. Photospheric spectra were obtained using the McMath Solar Telescope at Kitt Peak National Observatory, Arizona, USA. These analysis was carried out by means of the

method of spectrum synthesis. Lifetime measurements of nine Hf II levels have been performed by the beam-foil technique. These dominant spectral lines of Hf II in the solar spectrum and their upper levels were selected for this investigation. All Hf II lines investigated are situated in regions where numerous absorption lines occur.

The first detection of Hf II in a metal-poor halo star was reported in Sneden et al. (1996) in the spectrum of CS 22892-052 (two Hf II lines at 3719.28 Å and 3793.38 Å), with a mean abundance of log ϵ=-0.90±0.10. They compared their results with calculated contributions of r- and s-processes in the solar abundances, scaling the solar pattern to best fit the abundances of the 56≤ Z ≤76 elements. Elemental abundance in CS 22892-052 was reanalyzed by Sneden et al. (2003) who obtained the new value of log ϵ=-0.98±0.10.

In Den Hartog et al. (2021), authors recorded blue and UV spectra of several metal-poor stars and noticed many lines of singly ionized hafnium. Their report noted new measurements of the branching fraction for 199 UV and optical transitions of Hf II. These transitions range in wavelength (wavenumber) from 2068 to 6584 Å. With these these new transition probabilities it was derived and improved Hf abundances in two metal-poor stars. These lines show potential to be useful abundance indicators, for the stars namely HD 196944 enhanced in s-process elements and HD 222925 enhanced in r-process elements.

Hafnium is very important for nucleosynthesis of heavy elements. Improved laboratory data, especially atomic transition probabilities, are essential for using Hf as a reference element. New results were reported in Lawler et al. (2007), indicating Hf as a suitable stable reference element for nucleocosmochronometry, where it can serve for improved stellar age determination.

In Lawler et al. (2007), authors also disclosed radiative lifetimes of 8 Hf I and 18 Hf II levels, measured with the laser induced fluorescence technique. Branching fractions for transitions from the Hf II levels have been measured from the Fourier transform spectra. Combining the new lifetimes with the Branching fractions, 195 absolute oscillator strengths have been derived. In addition to the Branching fractions, accurate wavelengths for the 195 Hf II lines were measured. These data were applied in the determination of hafnium abundance in the chemically peculiar stars χ Lupi (HgMn) and HR 3383 (hot-Am), and were discussed in terms of possible revisions of the hafnium abundance for the Sun and the galactic halo stars CS 22892-052 and CS 31082-001 (see references Hill et al. (2002); Yushchenko et al. (2005); Ivarsson et al. (2003) for details).

2. Method

We used the simplified modified semiempirical method Dimitrijević & Konjević (1987), designed for Stark broadening of isolated spectral lines of singly and multiply charged ions in plasma. A more accurate semiclassical perturbation method Sahal-Bréchot (1969a,b); Sahal-Brechot et al. (2014) is not applicable

in an adequate way due to insufficient atomic data. Precise information on the closest perturber levels for both initial and final states of the transition is crucial for impact broadening parameters calculation.

Accordingly, full width at half maximum intensity reads:

$$w_{smse} = K_{fw} \frac{\lambda^2 N}{\sqrt{T}} (0.9 - \frac{1.1}{Z}) \sum_{k=i,f} \left(\frac{3n^*_{l_k}}{2Z} \right)^2 (n^*_{l_k}{}^2 - l_k{}^2 - l_k - 1) \tag{1}$$

where $\lambda[\text{m}]$ is the wavelength, $N[\text{m}^{-3}]$ denotes the perturber density, $T[\text{K}]$ the temperature, $K_{fw} = 2.21577 \cdot 10^{-20}$ m^{2}K$^{1/2}$ is a constant and $w_{smse}[\text{m}]$ is the full width at half maximum intensity. Initial atomic energy level is denoted by i and the final with f $(k = i, f)$. Z denotes ion residual charges: $Z = 1$ for neutral, $Z = 2$ for singly ionized, $Z = 3$ for doubly ionized, etc. Effective principal quantum number is labeled $n^*_{l_k}$, where l_k $(k = i, f)$ represents orbital angular momentum quantum number.

Formula for the Stark shift calculation depends on whether the transitions with $\Delta n = 0$ (where n denotes the main principal number) when all transition for $l+1$ and $l-1$ exist or not, as for example for s energy levels, where transition with $l - 1$ is missing. Its general form reads:

$$d_{smse} \approx K_{sh} \frac{\lambda^2 N}{\sqrt{T}} (0.9 - \frac{1.1}{Z}) \frac{9}{4Z^2} S \tag{2}$$

where $K_{sh} = 1.1076 \cdot 10^{-20}$ m^{2}K$^{1/2}$ is a constant and the polynomial S is calculated either like:

$$S_1 = \sum_{k=i,f} \frac{n^*_{l_k}{}^2 \epsilon_k}{2l_k + 1} (n^*_{l_k}{}^2 - 3l_k{}^2 - 3l_k - 1) \tag{3}$$

if all transition with $l + 1$ and $l - 1$ exist, or according to:

$$S_2 = \sum_{k=i,f} \frac{n^*_{l_k}{}^2 \epsilon_k}{2l_k + 1} [(l_k + 1)[n^*_{l_k}{}^2 - (l_k + 1)^2] - l_k (n^*_{l_k}{}^2 - l_k^2)] \tag{4}$$

in general; $\epsilon_k = +1$ for $k = i$ and $\epsilon_k = -1$ for $k = f$.

We used the following expression to calculate the averaged energies:

$$E = \frac{\sum_J (2J + 1) E_J}{\sum_J (2J + 1)} \tag{5}$$

where E represents the averaged energy in units cm^{-1}, E_J energy level and J the total angular momentum of a particular level.

3. Results and discussion

In this contribution, the research was continued on the singly ionized element Hafnium, which expands the list of the heavier elements that we tackled in the previous studies: iridium Simić et al. (2021), rhodium Simić & Sakan (2021) and rhenium Simić et al. (2023). The Stark broadening parameters were obtained - the widths and shifts of 28 Hf II spectral lines, according to the simplified modified semi-empirical method.
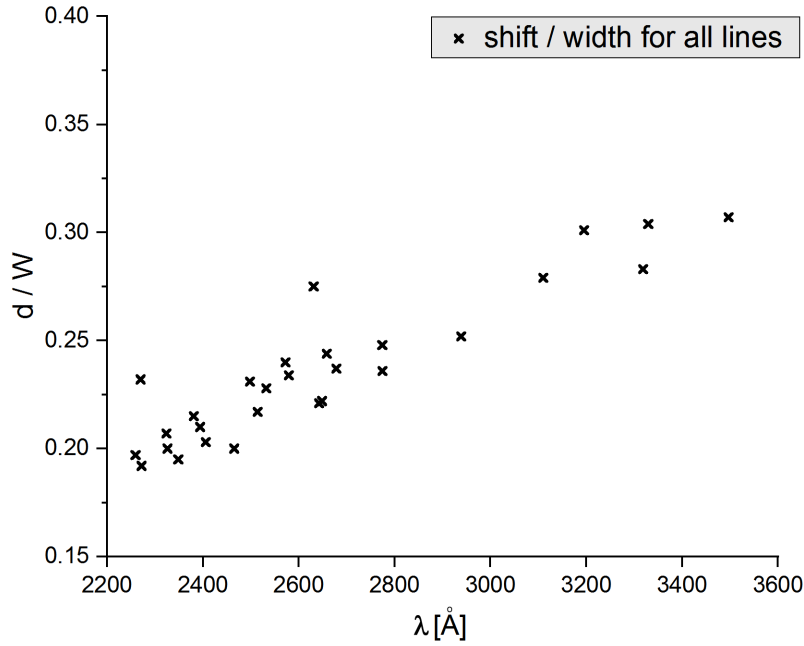
Figure 1. Ratio of calculated Stark shifts and widths for all spectral lines of singly ionized hafnium.

All calculations were performed using the electron density of 10^{17}cm^{-3} and temperatures from 5000 to 80000 K. Energy levels were taken from Moore (1971). Our results for the Hf II spectral lines are presented in Table 1. The first column presents transitions with calculated wavelengths, which may differ from the experimental ones. The second one contains the predefined temperatures, and the next two pairs of columns give the corresponding data for Stark width and shift in Å, as well as in angular frequency units. The latter are calculated according to the formulas:

$$W[\text{s}^{-1}] = \frac{2\pi c}{\lambda^2} W \tag{6}$$
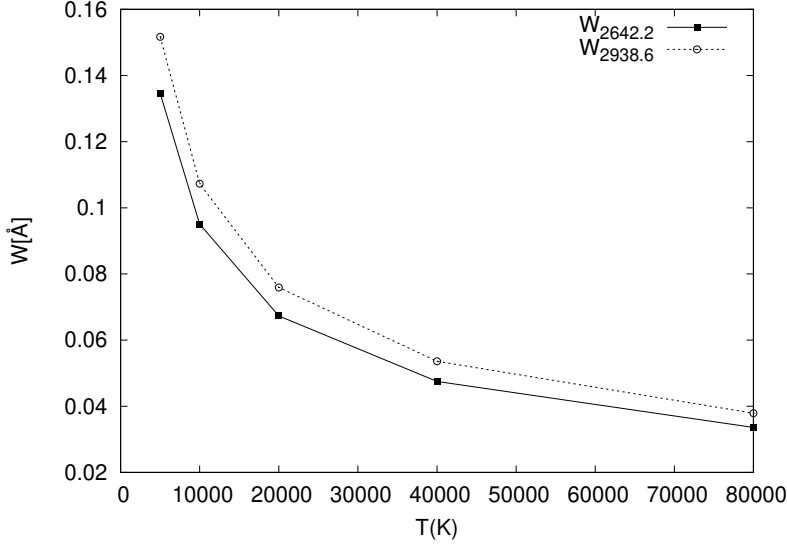
Figure 2. Dependence of width on temperature for 2642.2 Å and 2938.6 Å spectral lines of singly ionized hafnium of multiplet 6s ^{4}F - 6p ^{4}G^O.

$$d[\mathrm{s}^{-1}] = \frac{2\pi c}{\lambda^2} d \qquad (7)$$

where c is the light speed in inits m/s. The last column gives $3kT/2\Delta E$, where ΔE is the energy difference between the nearest perturbing level and the closest of the starting and ending levels. The $3kT/2\Delta E$ term must be less than or equal to two for the method to be valid. To determine the width or shift for an arbitrary experimental wavelength λ_{exp}, the following expressions should be used:

$$W_{exp} = (\frac{\lambda_{exp}}{\lambda})^2 W \qquad (8)$$

$$d_{exp} = (\frac{\lambda_{exp}}{\lambda})^2 d \qquad (9)$$

where W_{exp} and d_{exp} are the width and shift for an experimental λ_{exp}, and λ is a theoretical wavelength, with corresponding W and d (the width and shift) in Table 1.

In our calculations, we considered the supermultiplet of singly ionized hafnium 5d^2(a^{3}F)6s ^{4}F - 5d^2(a^{3}F)6p ^{4}(D, F, G)^O, which consists of the following multiplets with the identical parent term 5d^2(a^{3}F) for both the initial and final level. The first one is 6s ^{4}F - 6p ^{4}D^O with 9 spectral lines, the second one is 6s ^{4}F - 6p ^{4}F^O with 10 spectral lines and the third one is 6s ^{4}F - 6p ^{4}G^O with
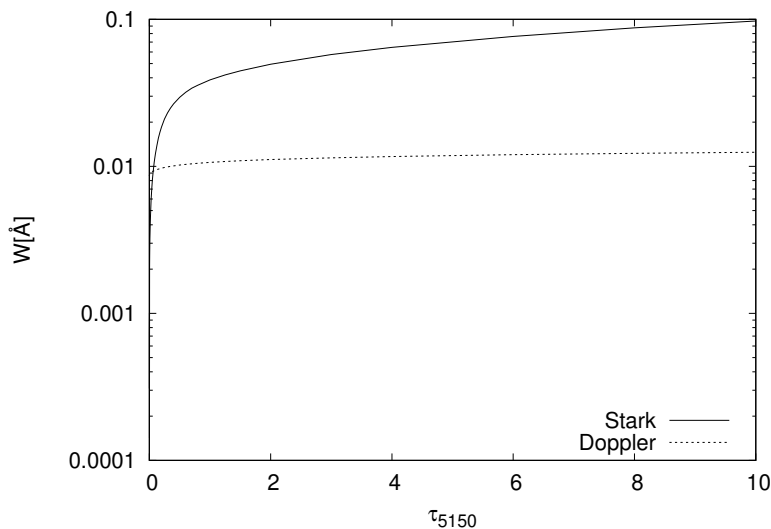
Figure 3. Thermal Doppler and Stark widths for Hf II 2642.2 Å spectral line of singly ionized hafnium of multiplet 6s ^{4}F - 6p ^{4}G^O for DA white dwarf atmosphere model with $T_{eff} = 15000$ K and log $g = 8$, as a function of optical depth τ_{5150}.

9 spectral lines, all of which fulfill the conditions of LS-coupling or Russell-Saunders coupling for connection and the selection rules. All labels are taken from Moore (1971); Reader et al. (1980); Ralchenko et al. (2005) and the NIST database, at site https://www.nist.gov/.

Taking into account the entire set of calculated spectral lines of singly ionized hafnium, we compared the shift and line width ratios (d/W) for each one, which can be seen in Figure 1. This ratio does not depend on the wavelength, temperature or density of the perturber, but it does depend on the quantum numbers and the optical charge seen by the electron. Minimum value of the ratio of 0.197 occurs for the 2259.4 Å line. The ratio increases approximately linearly with the wavelength, up to value 0.307 for the highest wavelength of 3496.8 Å.

For some of the calculated lines of singly ionized hafnium there are relative intensity presented in the NIST database. One of them has relative intensity of 1100 and it is observed at 2642.2 Å, which belongs to the multiplet 6s a^{4}F$_{9/2}$ - 6p z^{4}G$^o_{11/2}$, as well as the second strongest line of 2938.6 Å, with the relative intensity of 710. The Figure 2 shows the dependence of width on temperature, we notice that as the temperature increases, the width of the line decreases faster - the interval below 40000 K, and more slowly at higher temperatures than this. The spectral line 6s a^{4}F$_{9/2}$ - 6p z^{4}G$^o_{9/2}$ with wavelenght is 2938.6 Å from multiplet 6s ^{4}F - 6p ^{4}G^O was compared with the 2642.2 Å line. This results

is in accordance with the Eq. (1), given in the previous section, which provides dependencies from the wavelength and the initial and final energy levels.

In order to determine the influence of the Stark broadening in the atmosphere of hot stars, especially white dwarfs and check its importance and contribution, we tested the spectral line on the DA type model Wickramasinghe (1972) of white dwarfs, with $T_{eff} = 15000$ K and $\log g = 8$. Here, we denoted with τ_{5150} optical depth points at the standard wavelength λ_s=5150 Å also used in Wickramasinghe (1972). As can be seen from Figure 3 Stark broadening mechanism is more dominant in comparison with thermal Doppler, starting from the lowest photosphere layer in the atmosphere of the white dwarf. Our result shows 2642.2 Å spectral line from the multiplet 6s ^{4}F - 6p ^{4}G^O.

Insight into Stark broadening parameters is of great importance for the interpretation of spectra of A-type stars and white dwarfs, as we have shown in some of the previous studies Majlinger et al. (2015, 2017); Simić & Sakan (2020); Simić & Sakan (2021). Therefore, the Stark broadening must be taken into consideration when investigating stellar, technological and laboratory plasma.

4. Conclusion

In this paper, the selected transition metal is singly charged hafnium ion, which is detected in atmospheres of metallic stars, as for examle the spectrum of CS 22892-052. This element whose energy levels have been determined for 28 known lines provides opportunities for calulation by SMSE method to obtain Stark widths and shifts. We analyzed the shift-to-width ratio for all lines and observed the usual deviations as in previous studies of the transition metal group. We determined the influence of Stark broadening mechanism in the Atmosphere of a DA type white dwarf. The Stark broadening mechanism is very important for white dwarfs atmospheres, and one has to take into account this effect for their investigations, analysis and modeling.

Table 1. Electron-impact (Stark) broadening full widths at half intensity maximum (W) and shifts (d) for Hf II spectral lines, for a perturber density of 10^{17} cm^{-3} and temperatures from 5000 K to 80000 K.

Transition	T [K]	W [Å]	d [Å]	W [10^{12} s^{-1}]	d [10^{12} s^{-1}]	$\frac{3kT}{2\Delta E}$
Hf II a^{4}F$_{3/2}$ - 6p y^{4}D$^o_{1/2}$ 2381.03 Å	5000	0.103D+00	-0.223D-01	0.344	-0.074	0.124
	10000	0.733D-01	-0.158D-01	0.243	-0.052	0.248
	20000	0.519D-01	-0.111D-01	0.172	-0.037	0.497
	40000	0.367D-01	-0.791D-02	0.121	-0.026	0.993
	80000	0.259D-01	-0.559D-02	0.086	-0.018	1.986
Hf II 6s a^{4}F$_{3/2}$ - 6p y^{4}D$^o_{3/2}$ 2323.98 Å	5000	0.101D+00	-0.210D-01	0.354	-0.073	0.121
	10000	0.718D-01	-0.148D-01	0.250	-0.051	0.242
	20000	0.508D-01	-0.105D-01	0.177	-0.036	0.485
	40000	0.359D-01	-0.744D-02	0.125	-0.025	0.969
	80000	0.254D-01	-0.526D-02	0.088	-0.018	1.939
Hf II 6s a^{4}F$_{3/2}$ - 6p y^{4}D$^o_{5/2}$ 2259.39 Å	5000	0.992D-01	-0.196D-01	0.366	-0.072	0.118
	10000	0.701D-01	-0.138D-01	0.259	-0.051	0.236
	20000	0.496D-01	-0.979D-02	0.183	-0.036	0.471
	40000	0.350D-01	-0.692D-02	0.129	-0.025	0.942
	80000	0.248D-01	-0.490D-02	0.091	-0.018	1.885
Hf II 6s a^{4}F$_{3/2}$ - 6p y^{4}F$^o_{3/2}$ 2572.45 Å	5000	0.112D+00	-0.269D-01	0.318	-0.076	0.134
	10000	0.791D-01	-0.190D-01	0.225	-0.054	0.268
	20000	0.559D-01	-0.134D-01	0.159	-0.038	0.536
	40000	0.395D-01	-0.953D-02	0.112	-0.027	1.073
	80000	0.279D-01	-0.674D-02	0.079	-0.019	2.146
Hf II 6s a^{4}F$_{3/2}$ - 6p y^{4}F$^o_{5/2}$ 2497.75 Å	5000	0.108D+00	-0.251D-01	0.328	-0.075	0.130
	10000	0.768D-01	-0.177D-01	0.231	-0.053	0.260
	20000	0.543D-01	-0.125D-01	0.164	-0.037	0.521
	40000	0.384D-01	-0.889D-02	0.116	-0.026	1.042
	80000	0.271D-01	-0.628D-02	0.082	-0.018	2.084
Hf II 6s a^{4}F$_{3/2}$ - 6p z^{4}G$^o_{5/2}$ 3195.12 Å	5000	0.145D+00	-0.439D-01	0.268	-0.081	0.167
	10000	0.102D+00	-0.310D-01	0.189	-0.057	0.333
	20000	0.727D-01	-0.219D-01	0.134	-0.040	0.666
	40000	0.514D-01	-0.155D-01	0.094	-0.028	1.333
	80000	0.363D-01	-0.109D-01	0.067	-0.020	2.665
Hf II 6s a^{4}F$_{5/2}$ - 6p y^{4}D$^o_{3/2}$ 2394.09 Å	5000	0.108D+00	-0.228D-01	0.357	-0.075	0.125
	10000	0.769D-01	-0.161D-01	0.252	-0.053	0.250
	20000	0.544D-01	-0.114D-01	0.178	-0.037	0.499
	40000	0.384D-01	-0.808D-02	0.126	-0.026	0.999
	80000	0.272D-01	-0.571D-02	0.089	-0.018	1.997
Hf II 6s a^{4}F$_{5/2}$ - 6p y^{4}D$^o_{5/2}$ 2325.61 Å	5000	0.106D+00	-0.212D-01	0.369	-0.074	0.121
	10000	0.750D-01	-0.150D-01	0.261	-0.052	0.243
	20000	0.530D-01	-0.106D-01	0.184	-0.037	0.485
	40000	0.375D-01	-0.751D-02	0.130	-0.026	0.970
	80000	0.265D-01	-0.531D-02	0.092	-0.018	1.940
Hf II 6s a^{4}F$_{5/2}$ - 6p y^{4}D$^o_{7/2}$ 2271.39 Å	5000	0.104D+00	-0.199D-01	0.380	-0.072	0.118
	10000	0.736D-01	-0.141D-01	0.268	-0.051	0.237
	20000	0.520D-01	-0.999D-02	0.190	-0.036	0.474
	40000	0.368D-01	-0.706D-02	0.134	-0.025	0.947
	80000	0.260D-01	-0.499D-02	0.095	-0.018	1.895
Hf II 6s a^{4}F$_{5/2}$ - 6p y^{4}F$^o_{3/2}$ 2658.64 Å	5000	0.120D+00	-0.294D-01	0.322	-0.078	0.139
	10000	0.854D-01	-0.208D-01	0.227	-0.055	0.277
	20000	0.604D-01	-0.147D-01	0.161	-0.039	0.554
	40000	0.427D-01	-0.104D-01	0.113	-0.027	1.109
	80000	0.302D-01	-0.735D-02	0.080	-0.019	2.218

Table 1. Continued

Transition	T [K]	W [Å]	d [Å]	W [10^{12} s^{-1}]	d [10^{12} s^{-1}]	$\frac{3kT}{2\Delta E}$
Hf II 6s a^{4}F$_{5/2}$ - 6p y^{4}F$^o_{5/2}$ 2578.92 Å	5000	0.117D+00	-0.274D-01	0.331	-0.077	0.134
	10000	0.827D-01	-0.193D-01	0.234	-0.054	0.269
	20000	0.585D-01	-0.137D-01	0.165	-0.038	0.538
	40000	0.413D-01	-0.968D-02	0.117	-0.027	1.076
	80000	0.292D-01	-0.684D-02	0.082	-0.019	2.151
Hf II 6s a^{4}F$_{5/2}$ - 6p y^{4}F$^o_{7/2}$ 2531.96 Å	5000	0.114D+00	-0.262D-01	0.337	-0.077	0.132
	10000	0.811D-01	-0.185D-01	0.238	-0.054	0.264
	20000	0.574D-01	-0.131D-01	0.168	-0.038	0.528
	40000	0.406D-01	-0.927D-02	0.119	-0.027	1.056
	80000	0.287D-01	-0.655D-02	0.084	-0.019	2.112
Hf II 6s a^{4}F$_{5/2}$ - 6p z^{4}G$^o_{5/2}$ 3329.17 Å	5000	0.159D+00	-0.486D-01	0.271	-0.082	0.174
	10000	0.113D+00	-0.344D-01	0.192	-0.058	0.347
	20000	0.799D-01	-0.243D-01	0.135	-0.041	0.694
	40000	0.565D-01	-0.172D-01	0.096	-0.029	1.389
	80000	0.399D-01	-0.121D-01	0.067	-0.020	2.777
Hf II 6s a^{4}F$_{5/2}$ - 6p z^{4}G$^o_{7/2}$ 2631.02 Å	5000	0.107D+00	-0.297D-01	0.293	-0.080	0.155
	10000	0.762D-01	-0.210D-01	0.207	-0.057	0.310
	20000	0.539D-01	-0.148D-01	0.146	-0.040	0.621
	40000	0.381D-01	-0.105D-01	0.103	-0.028	1.242
	80000	0.269D-01	-0.743D-02	0.073	-0.020	2.483
Hf II 6s a^{4}F$_{7/2}$ - 6p y^{4}D$^o_{5/2}$ 2406.16 Å	5000	0.114D+00	-0.233D-01	0.373	-0.075	0.125
	10000	0.812D-01	-0.165D-01	0.264	-0.053	0.251
	20000	0.574D-01	-0.116D-01	0.186	-0.037	0.502
	40000	0.406D-01	-0.825D-02	0.132	-0.026	1.004
	80000	0.287D-01	-0.583D-02	0.093	-0.019	2.007
Hf II 6s a^{4}F$_{7/2}$ - 6p y^{4}D$^o_{7/2}$ 2348.17 Å	5000	0.112D+00	-0.219D-01	0.384	-0.074	0.122
	10000	0.795D-01	-0.155D-01	0.271	-0.053	0.245
	20000	0.562D-01	-0.109D-01	0.192	-0.037	0.490
	40000	0.397D-01	-0.775D-02	0.135	-0.026	0.979
	80000	0.281D-01	-0.548D-02	0.096	-0.018	1.959
Hf II 6s a^{4}F$_{7/2}$ - 6p y^{4}F$^o_{5/2}$ 2678.35 Å	5000	0.127D+00	-0.303D-01	0.335	-0.079	0.140
	10000	0.903D-01	-0.214D-01	0.237	-0.056	0.279
	20000	0.638D-01	-0.151D-01	0.167	-0.039	0.559
	40000	0.451D-01	-0.107D-01	0.118	-0.028	1.117
	80000	0.319D-01	-0.757D-02	0.083	-0.019	2.234
Hf II 6s a^{4}F$_{7/2}$ - 6p y^{4}F$^o_{7/2}$ 2269.86 Å	5000	0.933D-01	-0.216D-01	0.341	-0.079	0.137
	10000	0.660D-01	-0.152D-01	0.241	-0.055	0.274
	20000	0.466D-01	-0.108D-01	0.170	-0.039	0.548
	40000	0.330D-01	-0.764D-02	0.120	-0.027	1.096
	80000	0.233D-01	-0.540D-02	0.085	-0.019	2.192
Hf II 6s a^{4}F$_{7/2}$ - 6p y^{4}F$^o_{9/2}$ 2513.79 Å	5000	0.119D+00	-0.260D-01	0.356	-0.077	0.131
	10000	0.845D-01	-0.184D-01	0.252	-0.054	0.262
	20000	0.598D-01	-0.130D-01	0.178	-0.038	0.524
	40000	0.422D-01	-0.920D-02	0.126	-0.027	1.049
	80000	0.299D-01	-0.651D-02	0.089	-0.019	2.097
Hf II 6s a^{4}F$_{7/2}$ - 6p z^{4}G$^o_{5/2}$ 3496.75 Å	5000	0.179D+00	-0.549D-01	0.275	-0.084	0.182
	10000	0.126D+00	-0.388D-01	0.195	-0.059	0.365
	20000	0.895D-01	-0.274D-01	0.137	-0.042	0.729
	40000	0.632D-01	-0.194D-01	0.097	-0.029	1.459
	80000	0.447D-01	-0.137D-01	0.068	-0.021	2.917

Table 1. Continued

Transition	T [K]	W [Å]	d [Å]	W [10^{12} s^{-1}]	d [10^{12} s^{-1}]	$\frac{3kT}{2\Delta E}$
Hf II 6s a^{4}F$_{7/2}$ - 6p z^{4}G$^o_{7/2}$ 3110.01 Å	5000	0.152D+00	-0.425D-01	0.297	-0.082	0.162
	10000	0.108D+00	-0.301D-01	0.210	-0.058	0.324
	20000	0.763D-01	-0.212D-01	0.148	-0.041	0.649
	40000	0.539D-01	-0.150D-01	0.105	-0.029	1.297
	80000	0.381D-01	-0.106D-01	0.074	-0.020	2.594
Hf II 6s a^{4}F$_{7/2}$ - 6p z^{4}G$^o_{9/2}$ 2774.18 Å	5000	0.132D+00	-0.329D-01	0.325	-0.080	0.145
	10000	0.939D-01	-0.232D-01	0.229	-0.056	0.289
	20000	0.664D-01	-0.164D-01	0.162	-0.040	0.579
	40000	0.469D-01	-0.116D-01	0.114	-0.028	1.157
	80000	0.332D-01	-0.822D-02	0.081	-0.020	2.314
Hf II 6s a^{4}F$_{9/2}$ - 6p y^{4}D$^o_{7/2}$ 2464.93 Å	5000	0.125D+00	-0.2512-01	0.389	-0.077	0.129
	10000	0.889D-01	-0.177D-01	0.275	-0.055	0.257
	20000	0.628D-01	-0.125D-01	0.195	-0.038	0.514
	40000	0.444D-01	-0.888D-02	0.137	-0.027	1.028
	80000	0.314D-01	-0.628D-02	0.097	-0.019	2.056
Hf II 6s a^{4}F$_{9/2}$ - 6p y^{4}F$^o_{7/2}$ 2774.83 Å	5000	0.141D+00	-0.335D-01	0.347	-0.081	0.145
	10000	0.100D+00	-0.236D-01	0.245	-0.057	0.289
	20000	0.709D-01	-0.167D-01	0.173	-0.040	0.579
	40000	0.501D-01	-0.118D-01	0.122	-0.028	1.157
	80000	0.354D-01	-0.837D-02	0.086	-0.020	2.315
Hf II 6s a^{4}F$_{9/2}$ - 6p y^{4}F$^o_{9/2}$ 2648.09 Å	5000	0.134D+00	-0.299D-01	0.362	-0.080	0.138
	10000	0.954D-01	-0.212D-01	0.256	-0.056	0.276
	20000	0.674D-01	-0.149D-01	0.181	-0.040	0.552
	40000	0.477D-01	-0.106D-01	0.128	-0.028	1.105
	80000	0.337D-01	-0.749D-02	0.090	-0.020	2.209
Hf II 6s a^{4}F$_{9/2}$ - 6p z^{4}G$^o_{7/2}$ 3318.21 Å	5000	0.177D+00	-0.501D-01	0.303	-0.085	0.173
	10000	0.125D+00	-0.354D-01	0.214	-0.060	0.346
	20000	0.886D-01	-0.250D-01	0.151	-0.042	0.692
	40000	0.626D-01	-0.177D-01	0.107	-0.030	1.384
	80000	0.443D-01	-0.125D-01	0.075	-0.021	2.768
Hf II 6s a^{4}F$_{9/2}$ - 6p z^{4}G$^o_{9/2}$ 2938.64 Å	5000	0.151D+00	-0.382D-01	0.330	-0.083	0.153
	10000	0.107D+00	-0.270D-01	0.234	-0.059	0.306
	20000	0.758D-01	-0.191D-01	0.165	-0.041	0.613
	40000	0.536D-01	-0.135D-01	0.117	-0.029	1.226
	80000	0.379D-01	-0.956D-02	0.082	-0.020	2.451
Hf II 6s a^{4}F$_{9/2}$ - 6p z^{4}G$^o_{11/2}$ 2642.20 Å	5000	0.134D+00	-0.298D-01	0.363	-0.080	0.138
	10000	0.951D-01	-0.210D-01	0.256	-0.056	0.276
	20000	0.673D-01	-0.149D-01	0.181	-0.040	0.551
	40000	0.475D-01	-0.105D-01	0.128	-0.028	1.102
	80000	0.336D-01	-0.745D-02	0.090	-0.020	2.204

References

Andersen, T., Petersen, P., & Hauge, O., The solar hafnium abundance. 1976, *Solar Physics*, **49**, 211, DOI:10.1007/BF00162445

Den Hartog, E. A., Lawler, J. E., & Roederer, I. U., Improved Atomic Transition Probabilities for UV and Optical Lines of Hf II and Determination of the Hf Abundance in Two Metal-poor Stars. 2021, *ApJS*, **254**, 5, DOI:10.3847/1538-4365/abe861

Dimitrijević, M. S. & Konjević, N., Simple estimates for Stark broadening of ion lines in stellar plasmas. 1987, *Astronomy and Astrophysics*, **172**, 345

Hill, V., Plez, B., Cayrel, R., et al., First stars. I. The extreme r-element rich, iron-poor halo giant CS 31082-001. Implications for the r-process site(s) and radioactive cosmochronology. 2002, *A&A*, **387**, 560, DOI:10.1051/0004-6361:20020434

Ivarsson, S., Andersen, J., Nordström, B., et al., Improved oscillator strengths and wavelengths for Os I and Ir I, and new results on early r-process nucleosynthesis. 2003, *A&A*, **409**, 1141, DOI:10.1051/0004-6361:20031184

Lawler, J. E., den Hartog, E. A., Labby, Z. E., et al., Improved Laboratory Transition Probabilities for Hf II and Hafnium Abundances in the Sun and 10 Metal-poor Stars. 2007, *ApJS*, **169**, 120, DOI:10.1086/510368

Majlinger, Z., Simić, Z., & Dimitrijević, M. S., On the Stark Broadening of Lu III Spectral Lines. 2015, *Journal of Astrophysics and Astronomy*, **36**, 671, DOI:10.1007/s12036-015-9362-9

Majlinger, Z., Simić, Z., & Dimitrijević, M. S., Stark broadening of Zr IV spectral lines in the atmospheres of chemically peculiar stars. 2017, *Monthly Notices of the Royal Astronomical Society*, **470**, 1911, DOI:10.1093/mnras/stx1321

Moore, C. E., Atomic Energy Levels as Derived from the Analysis of Optical Spectra – Molybdenum through Lanthanum and Hafnium through Actinium. 1971, in *Nat. Stand. Ref. Data Ser. 35, Vol. III (Reprint of NBS Circ. 467, Vol. III, 1958)* (U.S.: Nat. Bur. Stand.)

Ralchenko, Y., Fuhr, J. R., Jou, F. C., et al., New Generation of the NIST Atomic Spectroscopic Databases. 2005, in American Institute of Physics Conference Series, Vol. **771**, *Atomic and Molecular Data and their Applications*, ed. T. Kato, D. Kato, & H. Funaba, 276–285

Reader, J., Corliss, C. H., Wiese, W. L., & Martin, G. A. 1980, *Wavelengths and transition probabilities for atoms and atomic ions: Part 1. Wavelengths, part 2. Transition probabilities*

Roederer, I. U., Lawler, J. E., Sobeck, J. S., et al., New Hubble Space Telescope Observations of Heavy Elements in Four Metal-Poor Stars. 2012, *ApJS*, **203**, 27, DOI:10.1088/0067-0049/203/2/27

Russell, H. N., On the Composition of the Sun's Atmosphere. 1929, *ApJ*, **70**, 11, DOI:10.1086/143197

Sahal-Bréchot, S., Impact Theory of the Broadening and Shift of Spectral Lines due to Electrons and Ions in a Plasma. 1969a, *Astronomy and Astrophysics*, **1**, 91

Sahal-Bréchot, S., Impact Theory of the Broadening and Shift of Spectral Lines due to Electrons and Ions in a Plasma (Continued). 1969b, *Astronomy and Astrophysics*, **2**, 322

Sahal-Brechot, S., Dimitrijevic, M., & Nessib, N., Widths and Shifts of Isolated Lines of Neutral and Ionized Atoms Perturbed by Collisions With Electrons and Ions: An Outline of the Semiclassical Perturbation (SCP) Method and of the Approximations Used for the Calculations. 2014, *Atoms*, **2**, 225, DOI:10.3390/atoms2020225

Simić, Z., Milovanović, N., Sakan, N., & Malović, M., On the Stark broadening of the Re II spectral lines. 2023, *Advances in Space Research*, **71**, 1287, DOI:10.1016/j.asr.2022.07.079

Simić, Z. & Sakan, N. M., The electron-impact broadening of the Nb III for 5p-5d transitions. 2020, *Monthly Notices of the Royal Astronomical Society*, **491**, 4382, DOI:10.1093/mnras/stz3362

Simić, Z. & Sakan, N. M., Stark Widths and Shifts of Rh II in Chemically Peculiar Stars. 2021, *International Astronomy and Astrophysics Research Journal*, **3**, 37

Simić, Z., Sakan, N. M., Milovanović, N., & Martinović, M., Singly Ionized Iridium Spectral Lines in the Atmosphere of Hot Stars. 2021, *International Astronomy and Astrophysics Research Journal*, **3**, 33

Sneden, C., Cowan, J. J., Lawler, J. E., et al., The Extremely Metal-poor, Neutron Capture-rich Star CS 22892-052: A Comprehensive Abundance Analysis. 2003, *ApJ*, **591**, 936, DOI:10.1086/375491

Sneden, C., McWilliam, A., Preston, G. W., et al., The Ultra–Metal-poor, Neutron-Capture–rich Giant Star CS 22892-052. 1996, *ApJ*, **467**, 819, DOI:10.1086/177656

Wickramasinghe, D. T., Model atmospheres for DA and DB white dwarfs. 1972, *Memoirs of the Royal Astronomical Society*, **76**, 129

Yushchenko, A., Gopka, V., Goriely, S., et al., Thorium-rich halo star HD 221170: Further evidence against the universality of the r-process. 2005, *A&A*, **430**, 255, DOI:10.1051/0004-6361:20041540

MolD, EMol and ACol atomic and molecular databases for astrophysics: current stage and new directions of development

V.A. Srećković[1] , **B.P. Marinković**[1] , **Lj.M. Ignjatović**[1] and **V.Vujčić**[2]

[1] *University of Belgrade, Institute of Physics Belgrade, PO Box 57, (E-mail: vlada@ipb.ac.rs, ljuba@ipb.ac.rs)*

[2] *Astronomical Observatory, Volgina 7, 11060 Belgrade, Serbia (E-mail: veljko@aob.rs)*

Abstract. In this contribution, we provide the current state of the MolD, EMol and ACol databases, hosted within the Virtual Atomic and Molecular Data Center (VAMDC) and the Serbian Virtual Observatory (SerVO). MolD, EMol and ACol are atomic and molecular databases dedicated to modeling various laboratory plasmas, and stellar atmospheres. Moreover, in this contribution, we present plans for the further directions of development like machine learning, software updates, etc.

Key words: databases – atoms – molecules – collisions – atmospheres – modeling – ML

1. Introduction

Data volumes have grown rapidly from terabytes to tens or hundreds of petabytes, and will continue to grow at an accelerating rate in the age of huge sky surveys and large telescopes (Koekemoer et al., 2007; Tucker et al., 2006). Simultaneously, utilizing new technologies, vast amounts of data and information (generated by potent supercomputer simulations) are dispersed throughout the global network architecture and archived in networks (Ivezić et al., 2019). Thus, research methodologies, algorithms, and procedures, as well as the state of data-oriented science, become crucial. One of the main driving forces behind the astronomical Virtual Observatories is still the operational processing and scientific utilization of such massive data sets (Djorgovski & Williams, 2005).

Atomic and molecular (A&M) data and databases are becoming increasingly important for diagnostics, data interpretation, and the development of models and simulations of complex physical processes (Iacob, 2014; Srećković et al., 2014; Mihajlov et al., 2011; Vujčić et al., 2023; Dubernet et al., 2024). One of the key goals of the astronomical Virtual Observatories is still the scientific use

of such resources. In this contribution we provide an overview of the MolD, EMol and ACol databases, hosted within the Virtual Atomic and Molecular Data Center (VAMDC) and the Serbian Virtual Observatory (SerVO), their current state and future directions of development like e.g. involvement of machine learning (ML) models to produce and predict new A&M data (see papers of Michalenko et al. 2021; Harris & Nepomuceno 2024).

2. The Virtual Observatory and BG nodes

The SerVO (`http://servo.aob.rs`) hosts the Belgrade radiative and collisional nodes MolD, EMol and ACol of the Virtual Atomic and Molecular Data Centre (VAMDC) (Albert et al., 2020). The databases MolD (`http://servo.aob.rs/mold`), EMol (`http://servo.aob.rs/emol/`) and ACol (`http://servo.aob.rs/acol`) include astrophysically relevant data. Furthermore, the data and its analysis demonstrate their interdisciplinary character and applications, such as in physics, astrophysics, and chemistry. Fig.1 represents a snapshot of the SerVO web page. One can see on the left side are links to BG Nodes (MolD, ACol, BEAMdb/ EMol) as well as STARK-B (database for "Stark" broadening of isolated lines of atoms and ions in the impact approximation). In the middle are links to the photo plate archive as well as new information related to scientific meetings, etc.

Figure 1. The SerVO's homepage. On the left side are links to BG Nodes. In the middle are links to the photo plate archive as well as new information related to scientific meetings, etc.

The MolD, EMol and ACol Belgrade A&M databases have been linked with the VAMDC project (`http://vamdc.eu`) since their early phases of development (see e.g. Vujčič et al., 2015; Marinković et al., 2015). The VAMDC project

Albert et al. (2020) intends to bring together numerous current databases under a common standard, creating a centralized platform for accessing atomic and molecular data. Users can download A&M data in a consistent format using the XML Schema for Atoms, Molecules, and Solids (XSAMS) (Marinković et al., 2017; Jevremović et al., 2020; Albert et al., 2020). Technically, the data models were updated to effortlessly transition to the VAMDC's tree-structured serialization schema, XSAMS. All databases are stored on a MariaDB server (an open-source relational database management system based on MySQL) and backed up on a regular basis.

2.1. The MolD database

Information on a number of molecular species and their excited states can be found in the MolD database (see, for example, Srećković et al., 2017a; Vujčić et al., 2023). As a radiative database it includes associated averaged thermal photodissociation cross sections and the data, i.e., photodissociation cross sections, for the various ro-vibrational states of the diatomic molecular ions (see Fig. 2).

Beginning at the end of 2014, the MolD database underwent multiple rounds of development. The Astronomical Observatory Belgrade is hosting it. Astronomers regularly use the MolD, to study a variety of astro phenomena and model stellar atmospheres (Coppola et al., 2013; Mihajlov et al., 2011; Srećković et al., 2014). Research on plasma chemistry and experiments are among the other uses for the data (Srećković et al., 2021, 2022).

2.2. The EMol database

The EMol database curates cross sections for electron interactions with atomic particles (atoms, molecules and ions) as well as energy loss and threshold spectra. Cross sections may be differential, integrated (integral and momentum transfer) or total. Processes that are covered within the database are elastic scattering, excitations (electronic and vibrational) and ionization (partial or total). At the moment, within the database there are 16 neutral atomic species and two ionic ones, while there are 16 neutral molecules and five cations. These numbers grow slowly but steadily over the years.

Data maintained within EMol are published in scientific journals and have passed the referee procedure. They are obtained either experimentally or theoretically. Data sets coming from experiments are usually of limited range of experimental parameters, like impact energy, scattering angle or energy loss, while calculated data may be voluminous with dense grid. That is why some of the experimental data needs to be completed. There are already attempts to extrapolate experimental differential cross sections to inaccessible domains by using machine learning algorithms (Ivanović et al., 2020). One of the examples of successful application of such algorithms in the determination of cross

Figure 2. MolD sample output. Data displayed in XSAMS format.

sections from transport coefficients using deep neural networks is presented by Stokes et al. (2020).

2.3. The ACol database

The ACol database contains data on cross sections and rate coefficients for collisional processes of excitation/deexcitation and ionization/recombination in hydrogen, helium, and alkali metal plasmas (see e.g. Srećković et al., 2017b; Srećković et al., 2022; Vujčić et al., 2023, and references therein). This is the youngest BG VAMDC node. SerVO hosts the ACol database. The website executes the queries locally and transmits data in the VAMDC-specified XSAMS format via an AJAX-enabled web page. The dataset/database can be used for laboratory research and modeling of interstellar gas, weakly ionized layers in various atmospheres, and low temperature plasma.

3. Summary and further directions

In this paper we provided an overview of the MolD, EMol and ACol databases, hosted within the VAMDC and SerVO. MolD, EMol and ACol are atomic and molecular databases dedicated to modeling various laboratory plasmas, and stellar atmospheres.

To maintain and curate databases effectively, it's important to stay up-to-date with the rapidly evolving IT sector, in addition to following basic principles. In this regard, new standards and database future upgrades should be:

– Updating Node software, including Python and Django, on a regular basis.

– Adding new AJAX-enabled queries, visualizations, and extensions to the website user interface.

– Adding new calculated/measured datasets and radiative/collisional processes.

– Involvement of ML models to produce i.e. to fast predict new A&M data. We are currently in the process of preparation for training and testing datasets for development of advanced models.

While ML models can provide quick predictions, it is crucial to remember that they may not be very accurate. Consequently, there should be some skepticism regarding the results and datasets of machine learning models.

References

Albert, D., Antony, B. K., Ba, Y. A., et al., A Decade with VAMDC: Results and Ambitions. 2020, *Atoms*, **8**, 76, DOI:10.3390/atoms8040076

Coppola, C. M., Galli, D., Palla, F., Longo, S., & Chluba, J., Non-thermal photons and H_2 formation in the early Universe. 2013, *MNRAS*, **434**, 114, DOI:10.1093/mnras/stt1007

Djorgovski, S. G. & Williams, R., Virtual Observatory: From Concept to Implementation. 2005, in Astronomical Society of the Pacific Conference Series, Vol. **345**, *From Clark Lake to the Long Wavelength Array: Bill Erickson's Radio Science*, ed. N. Kassim, M. Perez, W. Junor, & P. Henning, 517

Dubernet, M. L., Boursier, C., Denis-Alpizar, O., et al., BASECOL2023 scientific content. 2024, *Astronomy and Astrophysics*, **683**, A40, DOI:10.1051/0004-6361/202348233

Harris, A. L. & Nepomuceno, J., A data-driven machine learning approach for electron-molecule ionization cross sections. 2024, *Journal of Physics B Atomic Molecular Physics*, **57**, 025201, DOI:10.1088/1361-6455/ad2185

Iacob, F., Spectral characterization of hydrogen-like atoms confined by oscillating systems. 2014, *Cent. Eur. J. Phys.*, **12**, 628, DOI:10.2478/s11534-014-0496-1

Ivanović, S., Uskoković, N., Marinković, B. P., & Mason, N. J., Determining Extrapolated Differential Cross Sections from Data Sets in BEAMDB Using Machine Learning Algorithms. 2020, in 30th Summer School and International Symposium on the Physics of Ionized Gases, Vol. **99**, *Publications of the Astronomical Observatory of Belgrade*, ed. L. C. Popović, D. Borka, D. Ilić, & V. A. Srećković (Astronomical Observatory of Belgrade), 43–46, http://spig2020.ipb.ac.rs/Spig2020-Book-Onine.pdf

Ivezić, Ž., Kahn, S. M., Tyson, J. A., et al., LSST: From Science Drivers to Reference Design and Anticipated Data Products. 2019, *Astrophysical Journal*, **873**, 111, DOI:10.3847/1538-4357/ab042c

Jevremović, D., Srećković, V. A., Marinković, B. P., & Vujčić, V., Databases for collisional and radiative processes in small molecules needed for spectroscopy use in astrophysics. 2020, *Contributions of the Astronomical Observatory Skalnate Pleso*, **50**, 44, DOI:10.31577/caosp.2020.50.1.44

Koekemoer, A. M., Aussel, H., Calzetti, D., et al., The COSMOS Survey: Hubble Space Telescope Advanced Camera for Surveys Observations and Data Processing. 2007, *Astrophysical Journal, Supplement*, **172**, 196, DOI:10.1086/520086

Marinković, B. P., Jevremović, D., Srećković, V. A., et al., BEAMDB and MolD - databases for atomic and molecular collisional and radiative processes: Belgrade nodes of VAMDC. 2017, *European Physical Journal D*, **71**, 158, DOI:10.1140/epjd/e2017-70814-6

Marinković, B. P., Vujčić, V., Sushko, G., et al., Development of collisional data base for elementary processes of electron scattering by atoms and molecules. 2015, *Nuclear Instruments and Methods in Physics Research Section B: Beam Interactions with Materials and Atoms*, **354**, 90, DOI:10.1016/j.nimb.2014.12.039, 26th International Conference on Atomic Collisions in Solids

Michalenko, J. J., Murzyn, C. M., Zollweg, J. D., et al., Machine Learning Predictions of Transition Probabilities in Atomic Spectra. 2021, *Atoms*, **9**, DOI:10.3390/atoms9010002

Mihajlov, A. A., Ignjatović, L. M., Srećković, V. A., & Dimitrijević, M. S., Chemi-ionization in Solar Photosphere: Influence on the Hydrogen Atom Excited States Population. 2011, *Astrophys. J., Suppl. Ser.*, **193**, 2, DOI:10.1088/0067-0049/193/1/2

Srećković, V., Ignjatović, L., Jevremović, D., Vujčić, V., & Dimitrijević, M., Radiative and Collisional Molecular Data and Virtual Laboratory Astrophysics. 2017a, *Atoms*, **5**, 31, `DOI:10.3390/atoms5030031`

Srećković, V. A., Jevremović, D., Vujčić, V., et al., Mol-D a database and a web service within the Serbian virtual observatory and the virtual atomic and molecular data centre. 2017b, *Proceedings of the International Astronomical Union*, **12**, 393, `DOI:10.1017/S1743921316012643`

Srećković, V. A., Mihajlov, A. A., Ignjatović, L. M., & Dimitrijević, M. S., Ion-atom radiative processes in the solar atmosphere: quiet Sun and sunspots. 2014, *Advances in Space Research*, **54**, 1264, `DOI:10.1016/j.asr.2013.11.017`

Srećković, V. A., Ignjatović, L. M., & Dimitrijević, M. S., Photodestruction of Diatomic Molecular Ions: Laboratory and Astrophysical Application. 2021, *Molecules*, **26**, `DOI:10.3390/molecules26010151`

Srećković, V. A., Ignjatović, L. M., Kolarski, A., et al., Data for Photodissociation of Some Small Molecular Ions Relevant for Astrochemistry and Laboratory Investigation. 2022, *Data*, **7**, `DOI:10.3390/data7090129`

Stokes, P. W., Cocks, D. G., Brunger, M. J., & White, R. D., Determining cross sections from transport coefficients using deep neural networks. 2020, *Plasma Sources Science and Technology*, **29**, 055009, `DOI:10.1088/1361-6595/ab85b6`

Tucker, D. L., Kent, S., Richmond, M. W., et al., The Sloan Digital Sky Survey monitor telescope pipeline. 2006, *Astronomische Nachrichten*, **327**, 821, `DOI:10.1002/asna.200610655`

Vujčić, V., Marinković, B. P., Srećković, V. A., et al., Current stage and future development of Belgrade collisional and radiative databases/datasets of importance for molecular dynamics. 2023, *Physical Chemistry Chemical Physics*, **25**, 26972, `DOI:10.1039/D3CP03752E`

Vujčič, V., Jevremović, D., Mihajlov, A. A., et al., MOL-D: A Collisional Database and Web Service within the Virtual Atomic and Molecular Data Center. 2015, *Journal of Astrophysics and Astronomy*, **36**, 693, `DOI:10.1007/s12036-015-9344-y`

The strongest solar flares of Solar Cycle 25 and their subionospheric impact: data and modeling

V.A. Srećković[1,2] **, A. Kolarski**[1] **, M. Langović**[1] **, F. Arnaut**[1] **,**

S. Jevremović[1,2] **and Z.R. Mijić**[1]

[1] *University of Belgrade, Institute of Physics Belgrade, PO Box 57, (E-mail: vlada@ipb.ac.rs, kolarski@ipb.ac.rs, langovic@ipb.ac.rs, zoran.mijic@ipb.ac.rs)*

[2] *Scientific Society "Isaac Newton", Volgina 7, 11160 Belgrade, Serbia (E-mail: iniscientificsociety@gmail.com)*

Abstract. Solar flares, which are powerful explosions on the Sun's surface, are well recognized driving forces that have a significant impact on the near-Earth environment, causing extra ionization within the sunlit Earth's atmospheric layers. Based on how they affect the lower ionosphere and its electron density profile, X-ray solar flares can be categorized. In order to forecast the effects of potential solar occurrences during the waning phase of Solar Cycle 25, this study focuses on the disturbances caused by X-ray solar flares. In this paper we examined Solar Cycle progression i.e. solar activity of highest intensity (strongest 50 solar flares) during the ascending phase of Solar Cycle 25 by conducting numerical ionospheric modeling based on the Geostationary Operational Environmental Satellite (GOES) database on solar X-ray radiation.
Key words: Space weather – Solar activity – Solar X-ray flares – radio signal perturbations – GOES – data – modeling – electron density

1. Introduction

Strong explosions of electromagnetic radiation that come from the Sun's surface are known as solar flares (SFs) (Bothmer et al., 2007; Kahler, 1982; Tandberg-Hanssen & Emslie, 2009; Davidson, 2020; Riley & Love, 2017). The SF classifications range from A to X-class (see e.g. Grubor et al., 2008; Hayes et al., 2021, and references therein). Strong flares have the ability to impair communication and navigation systems and can cause disturbances in the ionosphere, affecting terrestrial communication. SFs emit powerful X-ray and ultraviolet radiation that can ionize the upper atmosphere, resulting in extra free electrons (Khodairy et al., 2020; Le et al., 2013; Šulić et al., 2016; Curto, 2020; Barta et al., 2022). These unbound electrons can affect radio wave propagation by changing the ionosphere's refractive characteristics (Thomson & Clilverd, 2000; Šulić & Srećković, 2014; Kolarski & Grubor, 2014; Srećković, 2023). The density of the

ionosphere briefly increases, affecting radio signals going through it (McRae & Thomson, 2004; Kelly, 2009; Nina et al., 2019; Srećković et al., 2024, 2017).

To forecast the impacts of potential solar occurrences during the declining phase of Solar Cycle 25, this study focuses on the disruptions induced by X-ray solar flares. In this paper, we investigated Solar Cycle progression, i.e. solar activity of highest intensity (strongest 50 solar flares) during the ascending phase of Solar Cycle 25 using numerical ionospheric modeling and the Geostationary Operational Environmental Satellite (GOES) (Aschwanden, 1994; Woods et al., 2024) database on solar X-ray radiation (https://data.ngdc.noaa.gov/platforms/solar-space-observing-satellites/goes).
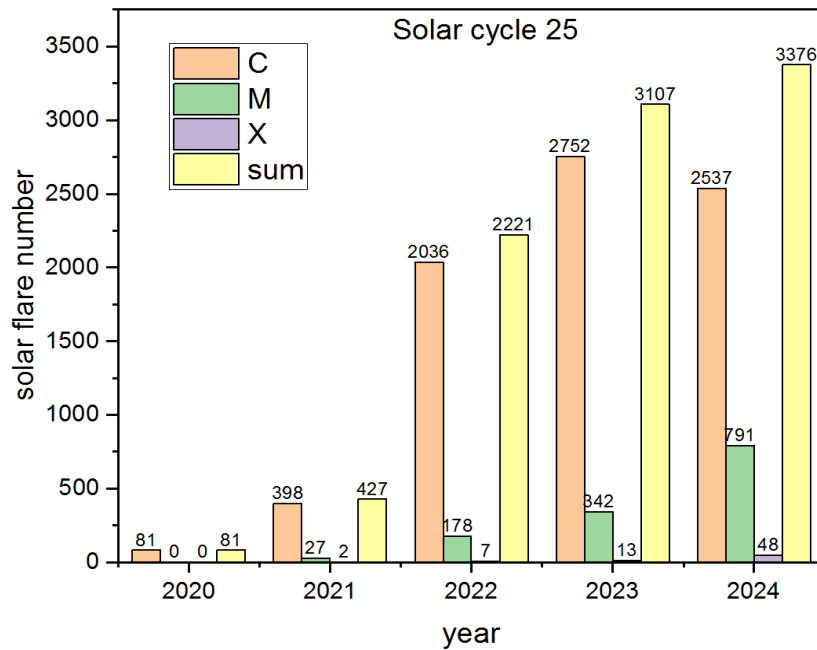
Figure 1. The graph shows the number of C, M and X-class solar flares that were produced during Solar Cycle 25 during the accessing phase, presented by year.

This study's findings may help to improve forecasting models (Gorney, 1990; Lean, 2010; Georgieva & Shiokawa, 2018; Bilitza et al., 2012, 2022), allowing for greater prediction and preparedness for ionospheric disruptions produced by high class SFs. The study of high-class SFs during Solar Cycle 25 and their impact on the ionosphere emphasizes the importance of ongoing research and monitoring of such occurrences to improve our understanding of space weather phenomena and protect technological infrastructure from potential disruptions.

The paper is organized as follows. This Section describes the current state and an introduction to the research problem. Section 2 provides results and analysis concerning the strongest solar flares of Solar Cycle 25 and their subionospheric impact, whereas Section Sec. 3 presents the conclusions and future perspectives of research.

2. Results and discussion

In this paper focus is on the further use of numerical method, so called easyFit that were developed by Srećković et al. (2021a,b) on the cases of high intensity SFs i.e. the strongest ones. We note that initially easyFit methods were developed for SF events of mid to high intensity (upper C-, M- and lower X-class SFs, see e.g. papers Srećković et al. (2021b); Kolarski et al. (2022)).

Datasets from this paper provide an overview of the results obtained by applying the numerical methods easyFit to the examples chosen for investigation, namely the top 50 SF of Solar Cycle 25 from X1.2 to X9. Solar X-ray flux was obtained from the Geostationary Operational Environmental Satellite (GOES) archive database (https://data.ngdc.noaa.gov/platforms/solar-space-observing-satellites/goes).

Figure 1 shows the number of C, M and X-class solar flares that were produced during the ascending branch of Solar Cycle 25 presented by year from 2020 to the end of 2024. We observe that, beginning in 2020 and reaching their peak at the end of 2024, the frequency of solar flares is clearly rising. It can be noted that on Jul 3, 2021 X1.59 - class flare occurred as the first X-class flare of Solar Cycle 25 and the first X-class solar flare since September 10, 2017.

Figure 2 upper panel shows sunspot number that were produced during the accessing phase of Solar Cycle 25 presented by year. We note that the number of sunspots is visibly increasing starting from 2020 and reaches its current maximum at the end of 2024. From the listed cases, differences in X-ray flux are associated with solar activity. Lower panel of Figure 2 shows the 50 strongest solar flares of Solar Cycle 25 (black circles) and corresponding reference height ionospheric D-region electron density (red circles). The left axis of the lower panel of Figure 2 shows the soft X-ray flux, while the right axis shows the perturbed values of the ower ionospheric electron density due to solar flares. The electron density is obtained by the easyFit method that was developed by Srećković et al. (2021a,b). One can observe a correlative behavior of increasing solar activity with increasing electron density.

Examining Solar Cycle progression we note that ionospheric disturbances and its parameters are correlated with solar activity during the ascending phase of Solar Cycle 25. These results will allow us to predict and model the ionosphere and its parameters during the waning phase of the Solar Cycle 25.
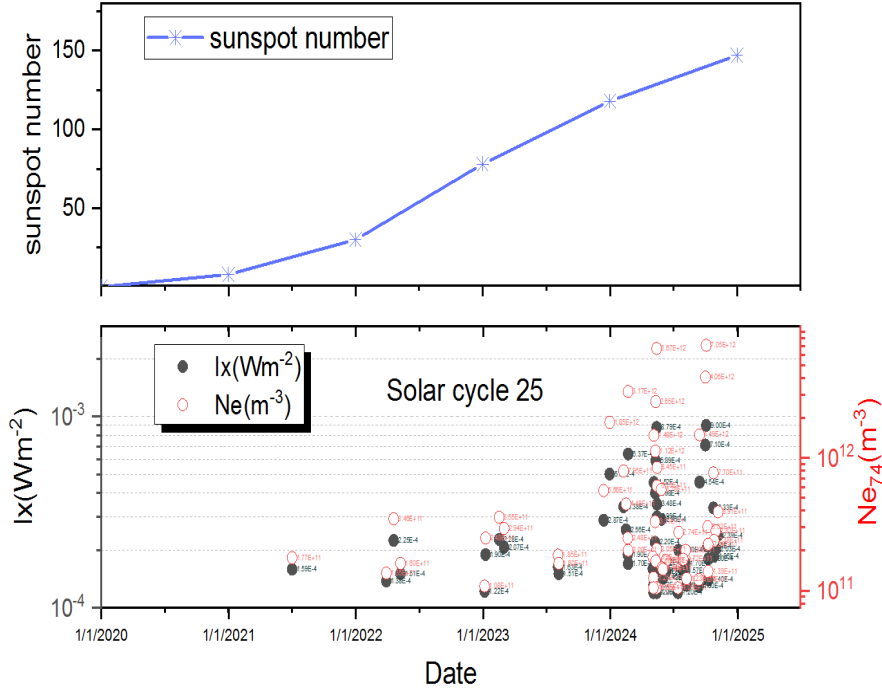
Figure 2. Upper panel: The graph shows sunspot number that were produced during Solar Cycle 25 by year; lower panel: The graph shows the 50 strongest solar flares of Solar Cycle 25 (black circles) and corresponding reference height ionospheric electron density (red circles).

3. Summary and future development

Solar flares, which are powerful explosions on the Sun's surface, are well recognized driving forces that have a significant impact on the near-Earth environment, causing extra ionization within the sunlit Earth's atmospheric layers. In order to forecast the effects of potential solar occurrences during the whole Solar Cycle 25, this study focuses on the disturbances caused by X-ray solar flares from 2020 to the end of 2024.

In this contribution, we investigated Solar Cycle progression, i.e. solar activity of highest intensity (strongest 50 solar flares) during the ascending phase of Solar Cycle 25, using numerical ionospheric modeling and the Geostationary Operational Environmental Satellite (GOES) database on solar X-ray radiation. Numerical method easyFit were applied to research impact of SFs of highest intensity ranging from X1 to X9 during 2020-2024 i.e. the ascending phase of Solar Cycle 25, with the aim to obtain parameters of perturbed lower ionosphere.

The results of this work could aid in the development of forecasting models, enabling better anticipation and readiness for ionospheric disturbances brought on by high-class SFs (see e.g. Gopalswamy, 2022). In order to better understand space weather events and safeguard technological infrastructure from potential disruptions, it is crucial to conduct continuous research and monitoring of high-class SFs during Solar Cycle 25 and their effects on the ionosphere.

References

Aschwanden, M. J., Irradiance observations of the 1-8 A solar soft X-ray flux from GOES. 1994, *Solar Physics (ISSN 0038-0938), vol. 152, no. 1, p. 53-59*, **152**, 53, DOI:10.1007/BF0147318

Barta, V., Natras, R., Srećković, V., et al., Multi-instrumental investigation of the solar flares impact on the ionosphere on 05–06 December 2006. 2022, *Frontiers in Environmental Science*, **10**, DOI:10.3389/fenvs.2022.904335

Bilitza, D., Brown, S. A., Wang, M. Y., Souza, J. R., & Roddy, P. A., Measurements and IRI model predictions during the recent solar minimum. 2012, *Journal of Atmospheric and Solar-Terrestrial Physics*, **86**, 99, DOI:10.1016/j.jastp.2012.06.010

Bilitza, D., Pezzopane, M., Truhlik, V., et al., The International Reference Ionosphere Model: A Review and Description of an Ionospheric Benchmark. 2022, *Reviews of Geophysics*, **60**, e2022RG000792, DOI:10.1029/2022RG000792

Bothmer, V., Daglis, I. A., & Bogdan, T. J., Space Weather: Physics and Effects. 2007, *Physics Today*, **60**, 59, DOI:10.1063/1.2825074

Curto, J. J., Geomagnetic solar flare effects: a review. 2020, *Journal of Space Weather and Space Climate*, **10**, 27, DOI:10.1051/swsc/2020027

Davidson, B. 2020, *Weatherman's Guide to the Sun, 3rd ed.* (Space Weather News, LLC.: New York, NY, USA)

Georgieva, K. & Shiokawa, K., Variability of the sun and its terrestrial impacts. 2018, *Journal of Atmospheric and Solar-Terrestrial Physics*, **180**, 1, DOI:10.1016/j.jastp.2018.09.008

Gopalswamy, N., The Sun and Space Weather. 2022, *Atmosphere*, **13**, DOI:10.3390/atmos13111781

Gorney, D. J., Solar cycle effects on the near-earth space environment. 1990, *Reviews of Geophysics*, **28**, 315, DOI:10.1029/RG028i003p00315

Grubor, D., Šulić, D., & Žigman, V., Classification of X-ray solar flares regarding their effects on the lower ionosphere electron density profile. 2008, *Annales Geophysicae*, **26**, 1731, DOI:10.5194/angeo-26-1731-2008

Hayes, L. A., O'Hara, O. S. D., Murray, S. A., & Gallagher, P. T., Solar Flare Effects on the Earth's Lower Ionosphere. 2021, *Solar Physics*, **296**, 157, `DOI:10.1007/s11207-021-01898-y`

Kahler, S. W., The role of the big flare syndrome in correlations of solar energetic proton fluxes and associated microwave burst parameters. 1982, *Journal of Geophysics Research*, **87**, 3439, `DOI:10.1029/JA087iA05p03439`

Kelly, M. C. 2009, *The Earth's Ionosphere: Plasma Physics and Electrodynamics, Second Edition* (Academic Press, USA)

Khodairy, S., Sharaf, M., Awad, M., Abdel Hamed, R., & Hussein, M., Impact of solar activity on Low Earth Orbiting satellites. 2020, in Journal of Physics Conference Series, Vol. **1523**, *Journal of Physics Conference Series* (IOP), 012010

Kolarski, A. & Grubor, D., Sensing the Earth's low ionosphere during solar flares using VLF signals and goes solar X-ray data. 2014, *Advances in space research*, **53**, 1595, `DOI:10.1016/j.asr.2014.02.022`

Kolarski, A., Srećković, V. A., & Mijić, Z. R., Monitoring solar activity during 23/24 solar cycle minimum through VLF radio signals. 2022, *Contributions of the Astronomical Observatory Skalnate Pleso*, **52**, 105, `DOI:10.31577/caosp.2022.52.3.105`

Le, H., Liu, L., Chen, Y., & Wan, W., Statistical analysis of ionospheric responses to solar flares in the solar cycle 23. 2013, *Journal of Geophysical Research (Space Physics)*, **118**, 576, `DOI:10.1029/2012JA017934`

Lean, J. L., Cycles and trends in solar irradiance and climate. 2010, *WIREs Climate Change*, **1**, 111, `DOI:10.1002/wcc.18`

McRae, W. M. & Thomson, N. R., Solar flare induced ionospheric D-region enhancements from VLF phase and amplitude observations. 2004, *Journal of Atmospheric and Solar-Terrestrial Physics*, **66**, 77, `DOI:10.1016/j.jastp.2003.09.009`

Nina, A., Srećković, V. A., & Radovanović, M., Multidisciplinarity in research of extreme solar energy influences on natural disasters. 2019, *Sustainability*, **11**, 974, `DOI:10.3390/su11040974`

Riley, P. & Love, J. J., Extreme geomagnetic storms: Probabilistic forecasts and their uncertainties. 2017, *Space Weather*, **15**, 53, `DOI:10.1002/2016SW001470`

Srećković, V. A., New Challenges in Exploring Solar Radiation: Influence, Consequences, Diagnostics, Prediction. 2023, *Applied Sciences*, **13**, 4126, `DOI:10.3390/app13074126`

Srećković, V. A., Dimitrijević, M. S., & Mijić, Z. R., Data in Astrophysics and Geophysics: Novel Research and Applications. 2024, *Data*, **9**, `DOI:10.3390/data9020032`

Srećković, V. A., Šulić, D. M., Ignjatović, L., & Vujčić, V., Low Ionosphere under Influence of Strong Solar Radiation: Diagnostics and Modeling. 2021a, *Applied Sciences*, **11**, 7194, `DOI:10.3390/app11167194`

Srećković, V. A., Šulić, D. M., Vujčić, V., Jevremović, D., & Vyklyuk, Y., The effects of solar activity: Electrons in the terrestrial lower ionosphere. 2017, *J. Geogr. Inst. Jovan Cvijic SASA*, **67**, 221, `DOI:10.2298/IJGI1703221S`

Srećković, V. A., Šulić, D. M., Vujčić, V., Mijić, Z. R., & Ignjatović, L. M., Novel Modelling Approach for Obtaining the Parameters of Low Ionosphere under Extreme Radiation in X-Spectral Range. 2021b, *Applied Sciences*, **11**, 11574, DOI: 10.3390/app112311574

Tandberg-Hanssen, E. & Emslie, A. G. 2009, *The Physics of Solar Flares* (Cambridge University Press, UK)

Thomson, N. R. & Clilverd, M. A., Solar cycle changes in daytime VLF subionospheric attenuation. 2000, *Journal of Atmospheric and Solar-Terrestrial Physics*, **62**, 601, DOI:10.1016/S1364-6826(00)00026-2

Šulić, D. M. & Srećković, V. A., A Comparative Study of Measured Amplitude and Phase Perturbations of VLF and LF Radio Signals Induced by Solar Flares. 2014, *Serbian Astronomical Journal*, **188**, 45, DOI:10.2298/SAJ1488045S

Šulić, D. M., Srećković, V. A., & Mihajlov, A. A., A study of VLF signals variations associated with the changes of ionization level in the D-region in consequence of solar conditions. 2016, *Advances in Space Research*, **57**, 1029, DOI:10.1016/j.asr.2015.12.025

Woods, T. N., Eden, T., Eparvier, F. G., et al., GOES-R Series X-Ray Sensor (XRS): 1. Design and pre-flight calibration. 2024, *Journal of Geophysical Research: Space Physics*, **129**, e2024JA032925, DOI:10.1029/2024JA032925

An overview of astronomical transient brokers in Rubin era

V. Vujčić[1] , **V. A. Srećković**[2] , **S. Babarogić**[3] and **J. Aleksić**[1]

[1] *Astronomical Observatory, Volgina 7, 11060 Belgrade, Serbia (E-mail: veljko@aob.rs)*

[2] *University of Belgrade, Institute of Physics Belgrade, PO Box 57, 11001 Belgrade, Serbia*

[3] *University of Belgrade, Faculty of Organizational Sciences, Jove Ilića, 11000 Belgrade, Serbia*

Abstract. Vera C. Rubin Observatory, formerly known as the Large Synoptic Survey Telescope (LSST) is approaching its operational phase, and all actors in the scientific/software ecosystem surrounding it are in the last phases of preparations. One of the types of the data that Rubin will publicly deliver are real-time alerts - a data stream of transient astronomical events. These alerts will be disseminated to the public through seven project-approved 'community brokers' - applications used to ingest data stream and provide various additional functionalities. In this review paper we compare software designs and analyze features of seven Rubin community brokers - ALeRCE, AMPEL, ANTARES, Babamul, Fink, Lasair, Pitt-Google.

Key words: astronomical transients – large astronomical survey – lsst – real time event processing – stream processing – data

1. Introduction

Both data suppliers, intermediary software and tool providers, and end users are getting ready for the start of the data flow as Vera C. Rubin Observatory - Legacy Survey of Space and Time, formerly known as the Large Synoptic Survey Telescope (LSST, Ivezić et al. (2019)), nears its operational phase. Real-time alerts, or data stream of transient astronomical occurrences, are one of the two main types of data products that LSST will deliver. Alert stream will be publicly available, but because of the infrastructural and bandwidth limits LSST approved seven 'community brokers' - software platforms that ingest, transform, add value and redistribute the stream - to act as intermediary layer between the data stream and the scientific community. Most broadly defined, the task of the 'broker' is not to act as a definitive scientific tool but to be an intermediary agent, reducing the stream to smaller number of events with most potential for particular science case and offering automatization capabilities to programmatically connect to the next tool in the process. That being said,

brokers differ in their functionalities and architecture, and the aim of this paper is to analyze and explain these differences.

Nightly pipeline - or Alert Production pipeline, one of several LSST data pipelines (Jurić et al., 2015), will process difference image data after it is obtained by the telescope. Each detection of an astronomical object which surpasses threshold of SNR>5 after performing subtraction from the template image will be treated as a potentially significant event and included in the alert stream. Every alert includes a package with LSST information about the source, including photometry, coordinates, and picture cutouts (Graham et al., 2019a). The stream will be broadcast in near-real time with a 60-second latency to account for processing time and source association.

LSST plans to ship alerts in Apache Avro serialization format with 12-month history, with approx 82KB size per alert packet - additionally LSST may ship 'lite' packets, drastically smaller without history and cutout. Broadband rate of the stream is estimated to be between 0.2 Gbps, and 5 Gbps, and this was the main reason LSST decided to limit the number of direct consumers by soliciting external(community) 'brokers'. After nine teams submitted full proposals (in 2020), seven were selected to receive direct full stream and two a downstream through an intermediary. Majority of selected brokers are developed and tested using data stream from Zwicky Transient Facility (ZTF Graham et al. 2019b) - a precursor to LSST at 10% data volume, which shares similar alert schema, serializaton format and streaming platform (Apache Kafka). LSST makes a distinction between a diaobject (dia as in difference image analysis), an astronomical object, and a diasource - a single measurement of the object, with one-to-many relationship. This terminology may differ in individual broker's documentation (object− >alert, locus− >alert, etc.) but the cardinality stays the same.

In this review we compare software designs and analyze features of seven Rubin community brokers - ALeRCE, AMPEL, ANTARES, Babamul, Fink, Lasair, Pitt-Google.

2. Overview of LSST community brokers

Brokers (a term long ago accepted in the astronomical community (Borne, 2008), more precisely stream/event processing engines) are intended to deal with real time, high throughput (big data is term more commonly used in the community) input streams of astronomical events.

2.1. Alerce

ALeRCE (https://alerce.science/, https://github.com/alercebroker) - Automatic Learning for the Rapid Classification of Events - is a Chilean event processing platform, rich in features, with online services and Python API. It includes the real-time ingestion, aggregation, cross-matching, machine learning (ML) classification, and visualization (see Förster et al., 2021). ALeRCE

performs two ML classification methods - a Balanced Hierarchical Random Forest (BHRF) on lightcurve features Sánchez-Sáez et al. (2021) and convolutional neural network classifier of cutout images - stamps Carrasco-Davis et al. (2021). More recently, ALeRCE tested novel approaches including Deep Learning Transformer Cabrera-Vives et al. (2024) which outperformed ALeRCE's own BHRF at the ELAsTiCC campaign[1]. For the outliers that don't belong to the proposed taxonomy, ALeRCE introduces anomaly detector based on deep support vector data description / autoencoder neural networks (Perez-Carrasco et al., 2023). ALeRCE offers a variety of services: a web portal wi for retrieval of astronomical objects via simplified graphical query with depiction of objects within a portfolio consisting of graphical lightcurves, classification assessments, cross-matching records, cutout stamps etc; a web portal used for real-time supernova (SN) candidates discovery updates, including visual spatial depiction; a Python client for interaction with Alerce databases and services (https://github.com/alercebroker/alerce_client); Target and Observation Manager - a tool for authorized users who can send follow-up requests; direct database access, Jupyter notebooks etc.

2.2. AMPEL

AMPEL (https://github.com/ampelproject, https://github.com/Ampel Astro) Alice in Modular Provenance-Enabled Land - alert management, photometry, and evaluation of light curves - is a scalable Python framework for general processing of large datasets, with specific application for astronomic alert streams (Nordin et al., 2019) developed at DESY, Hamburg. AMPEL is flexible - it can process real time or batch (existing) datasets, and extendable - it offers users to write additional code via python interface, or to easily plug an existing classification or analytical tool. AMPEL defines 'channels' as a subset of processes which belong to an individual user and is designed to avoid redundant processing, i.e resources will be shared between channels. Use of AMPEL is available through a fork or online live query API which requires pre-authorization.

2.3. ANTARES

ANTARES (https://antares.noirlab.edu/, https://gitlab.com/nsf-noirlab/csdc/antares/) - Arizona-NOIRLab Temporal Analysis and Response to Events System - is a broker which was conceived and funded long before the others, as early as 2014 (see e.g. Matheson et al., 2014). Its aim is to provide a web platform for filtering, flagging, categorizing and classifying relevant candidates and enable users to do science in various use cases. It has access through web portal which offers graphical querying, object portfolio, and defining custom science-enable filters written in Python. ANTARES can also be

---

[1]https://portal.nersc.gov/cfs/lsst/DESC_TD_PUBLIC/ELASTICC/

accessed via HTTP API, python client and webkit (Matheson et al., 2021). In the ANTARES system, 'locus' is a synonym for for an astrophysical object.

2.4. Babamul

Babamul (https://github.com/babamul/babamul), is conceived at Caltech as a lightweight and fully featured LSST broker but it seems like it was never fully developed or documented. A Babamul-related presentation was offered at the 2024 ESO - LSST workshop[2] where it was said that there is still a need for a low latency broker that is not heavy on hardware resources, without being specific about current status or plans for development. It was also mentioned that Fritz (https://www.ztf.caltech.edu/ztf-fritz.html), data management system within ZTF which was also developed at Caltech, would meet the broker function and handle LSST data rates. For the lack of more precise information, we will not further analyze Babamul in this work.

2.5. Fink

FINK Broker (https://fink-broker.org/, https://github.com/astro labsoftware/fink-broker), an international project centered around French National Centre for Scientific Research, is a robust alert processor based on Apache Spark engine for main streams (ZTF, LSST) and Apache Kafka for transformation of secondary streams. It is designed to efficiently handle high throughput and different timeframes of diverse astronomical phenomena (Möller et al., 2021). Fink defines science modules as additional functionalities written in Python - such as cross-matching, machine and deep learning classifiers, aggregators and additional community modules. The modules operate in an adjustable system, where input of one module can be used as the output of other modules. Fink distinguishes alert classification (which it does) from object classification. Fink is available through science (web) portal - which offers querying and rich objects portfolios, Python API, as well as redistributed Kafka filtered stream.

2.6. Lasair

Lasair (https://lasair-ztf.lsst.ac.uk/, https://github.com/lsst-uk/lasair-lsst), an Edinburgh/Oxford/Belfast collaboration, is a well-tested platform for filtering, adding value and storing alerts (Williams et al., 2024). As formulated in the documentation, 'Lasair is a platform for scientists to make science; it does not try to make the science itself'. Lasair web portal introduces concepts of filters, watchlists and annotators which are shareable among users. Filters are written as SQL queries to be applied on the running stream. Watchlists are personalized lists of points of interest in the sky from which alerts are

---

[2]https://www.eso.org/sci/meetings/2024/lsst.html

collected. Annotators include third party added-value tools, such as ML classifiers. Lasair also uses an internal classifier - Sherlock (Young, 2023), which uses spatial context implemented through search of archival catalogues with a boosted decision tree algorithm to give a primary classification assessment and spatial association (Smith, 2019).

2.7. Pitt-Google

Pitt-Google Alert Broker (https://github.com/mwvgroup/Pitt-Google-Broker, https://github.com/mwvgroup/pittgoogle-user) is an University of Pittsburgh project running on Google Cloud (GC) and provides alert stream filtering, distribution, processing, analysis, value adding with the focus on providing broad public access and flexibility. Users can use GC services or move data out of the cloud /citepwood2024pitt. Also, users can define their preferred level of pre-processing by using Pub/Sub services. Pitt-Google is highly flexible and customizable and can serve as a stream replicator (as LSST restricts direct shipping of alerts) with or without basic filtering, as well as full scale analytical/classification tool, where users access data through GC platform. Pitt-Google will offer subscription models, mainly to cover the costs of the GC services.

3. Comparison

We compare conceptual design of brokers to the concepts of stream processing as defined in relevant literature, cross-examine their functional and technical features, and offer a glimpse into the performance.

3.1. Design concepts

While most brokers were conceived and developed in the last five years, the idea and surrounding concepts are around two decades old (e.g Borne (2008)). A dedicated conference 'Hot-wiring the Transient Universe', which started in 2007, includes discussions on numerous aspects of automatization of processes involving transient event data. In comparison to the design based on relevant event processing literature (Fig.1), where blue rectangles present internal event processing agents and yellow hexagons interoperable communication channels, most of the brokers are built on similar premises - applying simple filtering for narrowing selection, enrichment by adding historical data (such as spectrography or additional photometry) from internal or external DB's, applying machine learning tools and/or predefined patterns, selecting most interesting candidates

for followup[3] and finally redistribute the altered stream in the same interoperable data format[4]. Some of them keep modular flexibility to skip or combine any of these steps. Somewhat in contrast to Fig.1, we can note prevalence of machine learning instead of pattern matching inference mechanism which can be explained with general tendency of ML/DL methods research within the astro community. We may remark here that while some methods offer significant accuracy, no ML classifier for significant phenomena such as Supernovae is valid to the point of conclusiveness (i.e it has to be verified further by a followup), and they are sometimes resource-heavy within the broker workflow. This trend shifted broker design perspective from high performance stream engines (designed to transform, reduce and apply inference mechanisms), to centralized cluster-hosted feature-rich scientific tools. It will take several years from now to see which paradigm is optimal.
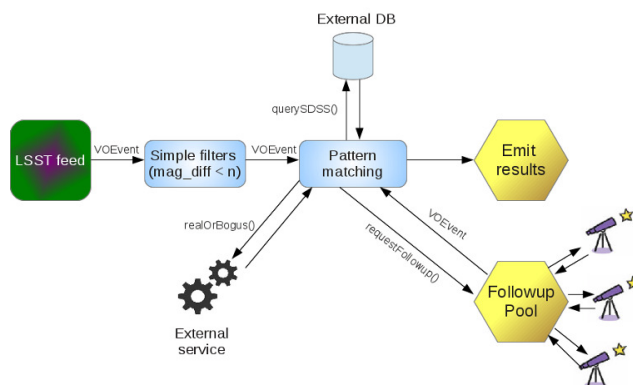
Figure 1. A proposed event processing network for real-time detection and classification of astronomical alerts - Figure from Vujčić (2014); Vujčić & Jevremović (2020), based on stream processing building blocks as defined in Etzion & Niblett (2010).

3.2. Functional and technical features

As we saw in the Sec. 2, functionalities of different brokers can vary or overlap and it's common to use different terms for the same concept. For example, AMPEL uses 4-tier event processing architecture, with following concepts - *add*,

---

[3]Software tools that manage 'Followup Pool', i.e that coordinate requests between brokers and telescopes/facilities for additional observation, are now called TOMs - from Target and Observation Manager. For more info, see https://lco.global/tomtoolkit/ and https://tom-toolkit.readthedocs.io/en/stable/

[4]In the late 2010's LSST switched from the International Virtual Observatory Alliance (https://ivoa.net) VOEvent XML/json standard for exchange of astronomical events to a more resource-efficient avro format (https://github.com/lsst/alert_packet).

combine, *complement*, *react* which correspond to design patterns of filter, correlate, enrich and pattern match as defined in literature (Tsimelzon, 2006). Core concepts of event processing (and synonyms used in brokers' documentation, in brackets), as defined in the seminal book on event processing, Etzion & Niblett (2010), include: ingestion, filtering, correlation (joining streams, multimessaging), enrichment (complement, annotate, query, cross-match, xmatch), matching (machine learning, classify, characterize, react) and distribution. Brokers often add some of the features taken over from other types of software, such as rich UX, object portfolios, programmable/extensible APIs etc. In this sense, functionalities of some brokers aim to push more ambitiously into scientific exploration and overlap with other multipurpose, integrated astronomical platforms such as SkyPortal (Coughlin et al., 2023).

For concrete cross-comparison of functional and technical aspects, we show Table 1. We compare brokers across twelve operational and infrastructure categories. Where functionalities of all brokers overlap are most fundamental concepts - basic stream filtering capabilities, cross-matching (with internal storage/external access differences) and API's that offer programmatic extension to external tools (like custom analytic tools or TOMs/Marshalls). Also, all of the brokers are open-source and are published at online git repositories. Most brokers are free - Pitt-Google will work on a subscription model, charging for cloud services and some (like AMPEL) offer limited access to the 'live' version running on their own resources. Most use machine (deep) learning algorithms for classification estimate - here we make a distinction between the teams who made efforts to develop a variety of detailed methods ('rich'), a single/provisional method(s) ('basic') and an option to include other's methods ('external'). Only Fink and Google-Pitt base their back-end on a proven industry stream processor platform, while all of the brokers apply cluster storage solutions, whether relational, document or a combination of both. ALeRCE, ANTARES, Fink and Lasair each developed a convenient web-portal with options for online querying and portfolios of astronomical objects, among other project-specific features. ANTARES, Fink, Lasair and Google-Pitt can redistribute alerts in the original avro format. Although built on different premises, it could be said that AMPEL, Fink, Lasair and Google-Pitt share concept of modularity, offering users/developers to choose which aspects or functions of the system will they include in their own workflow.

3.3. Performance

There were two LSST broker challeges in 2022 and 2023 called ELAsTiCC[5], with taxonomy tree defined by the ELAsTiCC team (Malz & Knop, 2022). where "all brokers have demonstrated the ability to classify objects in less than one day, and often in less than 3 hours" (Knop & Team, 2023). During June

---

[5]Extended LSST Astronomical Time-series Classification Challenge

2024, Operations Rehearsal 4 Rubin Observatory processed simulated ComCam images sent from the summit and sent live alerts to brokers where all brokers operated at the same time. However, the purpose of the test was not to evaluate performance metrics in any specific sense, but rather to demonstrate that the series of processes operates successfully.

According to the private communication with some of the authors of the brokers, including Julien Peloton of Fink and Roy Williams of Lasair, attempting direct comparisons between brokers in order to compare some measurable value is a common misconception. The brokers associated with the Rubin Observatory are not alternative implementations designed for the same scientific objective but distinct implementations tailored to diverse scientific goals that often do not overlap. According to members involved, the questions that brokers are designed to address are shaped by the specific needs and priorities of their respective user communities, each of which defines "performance" differently.

4. Conclusion

We gave the overview of the current pallette of brokers for transient astronomical events - software tools designed to act as an intermediary layer between high throughput astronomical streams and more specific scientific tools. Different brokers match in some aspects and diverge in other aspects of their functionalities and conceptual design. Our broad conclusion points would be: Lasair and ALeRCE offer richest web portal features and may be appealing to widest scientific community; ALeRCE team has put most effort into development of ML classifying methods, but that might prove not to be of primary importance as some brokers allow external classifiers; Fink and Pitt-Google have robust architecture which may be critical for latency/volume ratio of some scientific use cases; Fink, AMPEL, Pitt and Lasair show various ranges of systemic modularity, where AMPEL might prove most flexible in terms of low coupling of modules and workflow extensibility. Overall, Fink fulfills all functional, design and infrastructure requests that we analyzed - not necessarily being dominant in each one of them. Choice of the broker will depend on specific scientific use cases, flexibility for further refinement as the LSST survey proceeds and assignment/availability of resources.

Table 1. Comparison of community brokers' features

	ALeRCE	AMPEL	ANTARES	FINK	Lasair	Pitt-Google
Filtering	x	x	x	x	x	x
ML/classifiers integration	rich	basic		rich+external	basic+external	basic
Cross-match external dbs	x	x	stored internally	x	stored internally for classification, portal only for annotation	x
Web portal with object portfolio	x		x	x	x	via api only
Client API	x	x	x	x	x	x
HTTP/REST API			x	x		
Based on industry stream processor				apache spark		google cloud platform
Cluster storage	s3 + postgresql cluster	mongodb	cassandra + mysql cluster	hbase	cassandra + galera mysql	bigquery
Open source / online repo	x	x	x	x	x	x
Redistribution in the same format			x	x	x	x
Association with other real time streams				x		
Modularity		x		x	x	x

References

Borne, K., A machine learning classification broker for the LSST transient database. 2008, *Astronomische Nachrichten: Astronomical Notes*, **329**, 255, DOI:10.1002/asna.200710946

Cabrera-Vives, G., Moreno-Cartagena, D., Astorga, N., et al., ATAT: Astronomical Transformer for time series and Tabular data. 2024, *Astronomy and Astrophysics*, **689**, A289, DOI:10.1051/0004-6361/202449475

Carrasco-Davis, R., Reyes, E., Valenzuela, C., et al., Alert Classification for the ALeRCE Broker System: The Real-time Stamp Classifier. 2021, *Astronomical Journal*, **162**, 231, DOI:10.3847/1538-3881/ac0ef1

Coughlin, M. W., Bloom, J. S., Nir, G., et al., A data science platform to enable time-domain astronomy. 2023, *The Astrophysical Journal Supplement Series*, **267**, 31, DOI:10.3847/1538-4365/acdee1

Etzion, O. & Niblett, P. 2010, *Event processing in action* (Manning Publications Co., United States)

Förster, F., Cabrera-Vives, G., Castillo-Navarrete, E., et al., The Automatic Learning for the Rapid Classification of Events (ALeRCE) Alert Broker. 2021, *Astronomical Journal*, **161**, 242, DOI:10.3847/1538-3881/abe9bc

Graham, M., Bellm, E., Guy, L., Slater, C., & Dubois-Felsmann, G. 2019a, *LSST Alerts: Key Numbers* (DMTN-102, URL https://dmtn-102. lsst. io, LSST Data Management Technical Note)

Graham, M., Kulkarni, S., Bellm, E., et al., The Zwicky Transient Facility: Science Objectives. 2019b, *Publications of the Astronomical Society of the Pacific*, **131**, 078001, DOI:10.1088/1538-3873/ab006c

Ivezić, Ž., Kahn, S. M., Tyson, J. A., et al., LSST: From Science Drivers to Reference Design and Anticipated Data Products. 2019, *Astrophysical Journal*, **873**, 111, DOI:10.3847/1538-4357/ab042c

Jurić, M., Kantor, J., Lim, K., et al., The LSST data management system. 2015, *arXiv preprint arXiv:1512.07914*

Knop, R. & Team, E., Simulated Transient Alerts and Broker Classifications for ELAsTiCC. 2023, in *American Astronomical Society Meeting Abstracts*, 117–02

Malz, A. & Knop, R. 2022, ELAsTiCC taxonomy, https://github.com/LSSTDESC/elasticc/blob/elasticc2/taxonomy/taxonomy.ipynb, [Online; accessed 12-2024]

Matheson, T., Saha, A., Snodgrass, R., & Kececioglu, J., ANTARES: A Prototype Transient Broker System. 2014, in American Astronomical Society Meeting Abstracts, Vol. **223**, *American Astronomical Society Meeting Abstracts #223*, 343.02

Matheson, T., Stubens, C., Wolf, N., et al., The ANTARES astronomical time-domain event broker. 2021, *The Astronomical Journal*, **161**, 107, DOI:10.3847/1538-3881/abd703

Möller, A., Peloton, J., Ishida, E. E., et al., FINK, a new generation of broker for the LSST community. 2021, *Monthly Notices of the Royal Astronomical Society*, **501**, 3272, DOI:10.1093/mnras/staa3602

Nordin, J., Brinnel, V., Van Santen, J., et al., Transient processing and analysis using AMPEL: alert management, photometry, and evaluation of light curves. 2019, *Astronomy & Astrophysics*, **631**, A147, DOI:10.1051/0004-6361/201935634

Perez-Carrasco, M., Cabrera-Vives, G., Hernandez-García, L., et al., Alert classification for the alerce broker system: The anomaly detector. 2023, *The Astronomical Journal*, **166**, 151, DOI:10.3847/1538-3881/ace0c1

Sánchez-Sáez, P., Reyes, I., Valenzuela, C., et al., Alert Classification for the ALeRCE Broker System: The Light Curve Classifier. 2021, *Astronomical Journal*, **161**, 141, DOI:10.3847/1538-3881/abd5c1

Smith, K., Lasair: the transient alert broker for LSST: UK. 2019, *The Extragalactic Explosive Universe: the New Era of Transient Surveys and Data-Driven Discovery*, 51

Tsimelzon, M. 2006, Complex Event Processing: Ten Design Patterns, [Online; accessed 12-2024]

Vujčić, V., Use of complex event processing engines in astronomy. 2014, in *Big Data Conference proceedings, Szombately Hungary*

Vujčić, V. & Jevremović, D., Real-time stream processing in astronomy. 2020, in *Knowledge Discovery in Big Data from Astronomy and Earth Observation* (Elsevier), 173–182

Williams, R. D., Francis, G. P., Lawrence, A., et al., Enabling science from the Rubin alert stream with Lasair. 2024, *RAS Techniques and Instruments*, **3**, 362

Young, D. R. 2023, *Sherlock. Contextual classification of astronomical transient sources*, DOI:10.5281/zenodo.8038057

Some features in the time series of energetic protons measured at L1 during November 2001

N. Veselinović[1] , **M. Savić**[1] , **D. Maričić**[2], **F. Šterc**[2], **R. Banjanac**[1],
D. Joković[1] **and A. Dragić**[1]

[1] *Institute of Physics Belgrade, Pregrevica 118,11090 Belgrade, Serbia*
(E-mail: veselinovic@ipb.ac.rs)

[2] *Astronomical Observatory Zagreb, Opatička 22, 10000 Zagreb, Croatia*

Abstract. Extreme events originating on the Sun induce various processes in the heliosphere, such as shock waves and particle acceleration. In this work, we studied the impact of extreme solar events on the flux of energetic particles measured at Lagrange point L1. In many cases, the enhanced flux of energetic particles can be clearly associated with a specific source and involves a well-known acceleration mechanism. However, in some instances, this connection is not as easily established. We examined and compared structures in energetic proton time series where a clear source is not immediately obvious, with structures clearly related to the concurrent passage of an ICME by analyzing the event-integrated fluence of energetic protons during November 2001 to potentially gain insight into the origin of such events.

Key words: solar energetic particles – solar activity – fluence spectra

1. Introduction

The study of transient phenomena caused by solar activity is of great importance, as these events can affect Earth's magnetosphere, environment, technological infrastructure and systems (Kataoka et al. (2018); Belov et al. (2022); Kolarski et al. (2023) and references therein). With the rising phase of the current Solar cycle 25, a better understanding and study of these transient phenomena are of great importance. Extreme events originating on the Sun, like solar flares (SF) and coronal mass ejections (CME) induce various processes in the heliosphere, such as shock waves and particle acceleration (Waterfall et al., 2023). All these processes can lead to the acceleration of charged particles (both of local and solar origin), resulting in an increased flux of these particles. The enhanced flux of solar energetic particles (SEP) during extreme solar events can be, in many cases, associated with a specific source (i.e., the passage of an interplanetary CME (ICME) related shock in heliosphere). However, this connection can be questionable in some instances. There are two major physical mechanisms of SEP acceleration based on the research conducted during several solar cycles

(Reames, 2013). One of the mechanisms is associated with type II radio bursts from coronal and interplanetary shock waves. It is driven by fast CMEs and it is proton-dominated. This mechanism produces "gradual" SEP events that have high SEP flux intensity near Earth, which can last for days. The second mechanism is predominantly connected to magnetic reconnection with open magnetic field lines and resonant wave–particle interactions in impulsive SFs and jets. It is associated with type III radio bursts produced by streaming electrons and produces "impulsive" SEP events that last for hours. In this work, we compared the features of different structures observed in energetic proton flux time series by analyzing the event-integrated fluences at L1 during November 2001, aiming to gain insight into their origin.

2. Data sets and event overview

2.1. Data sets

For this study we used data measured in-situ at Lagrange point L1 by SOHO and WIND probes. Data from Energetic and Relativistic Nuclei and Electron (ERNE) sensor unit onboard the Solar and Heliospheric Observatory (SOHO) (Torsti et al., 1995) was used to provide hourly data of energetic protons and interplanetary magnetic field and solar wind speed data were provided by the Global Geospace Science WIND spacecraft from OMNIWeb Plus repository (King & Papitashvili, 2005). For event selection, we used online CME, ICME and major SEP events catalogs (CDAW (2024); Richardson & Cane (2024))

2.2. Extreme events during November 2001

During November 2001 there has been a heightening activity of the Sun (Gopalswamy et al. (2010); Falkenberg et al. (2011); Rawat et al. (2006)). Four X-class solar flares have been reported (November 4, 8, 22, 28), along with two strong geomagnetic storms (November 6, 24) and several CME/ICME and SEP events in succession. At the beginning of November a series of three halo CME with most pronounce on November 4, originated from active region 9684 with an initial speed of $1810\,\mathrm{km\,s^{-1}}$ produced ICME. A strong interplanetary shock on November 6, characterized by abrupt increase in solar wind speed and total interplanetary magnetic field (IMF) and proton flux was recorded by WIND and SOHO/ERNE (Fig. 1). Later during November 2001, the activity of the Sun risen again. On 17 November a halo CME was observed with an initial speed of $1379\,\mathrm{km\,s^{-1}}$ and the ensuing ICME was observed at Earth and even Mars two days later. Two halo CMEs were emitted from the Sun on 22 and 23 November with that merged into one ICME at near-Earth location and produce geomagnetic storm and an increase in solar wind parameters, as shown in Fig.1
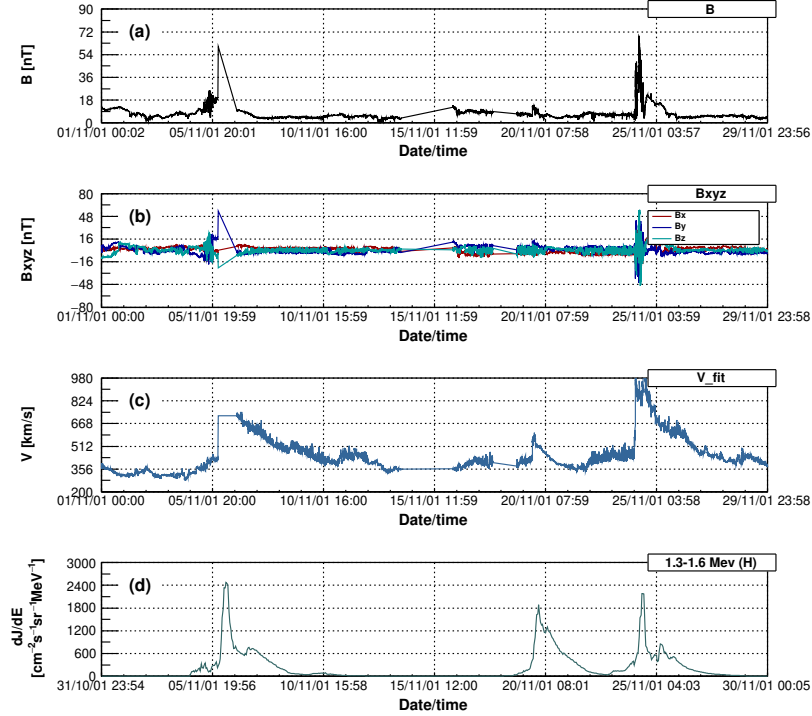
Figure 1. Time series of selected solar wind parameters measured by WIND and SOHO/ERNE proton flux data for November 2001: (a) IMF, (b) IMF components, (c) solar wind speed, and (d) energetic proton flux in the 1.3–1.6 MeV energy channel.

3. Analysis and discussion

The data provided by the instruments onboard the WIND spacecraft were used to establish a link and precise timing between the passage of an ICME and its effects on the onset and duration of the increased energetic proton flux. We found that the most useful parameters for this purpose are the time series of the IMF and the solar wind velocity. As WIND data are missing at the beginning of November, around the time of one of the extreme events, this period has been omitted from the analysis. Instead, the focus is on the second half of November, where all the necessary data are available. During the second half of November 2001, the arrival of the ICME shock is clearly observed in both the time series of IMF data and the flux of energetic protons (Fig. 1). One particularly interesting feature is a significant increase in proton flux that precedes the second ICME shock and cannot be directly associated with any perturbation in the IMF parameters. This structure is interesting because the

measured flux exhibits a different energy dependence compared to the structure directly associated with the shock, which is especially evident in the higher-energy channels (Fig. 2).

Time intervals marking the ICME shock/interaction were determined based on the IMF and CME data. Based on these intervals proton flux was integrated in all SOHO/ERNE energy channels for three enhancements observed in the second half of November. The procedure is illustrated in Fig. 2, where cyan color is used for the two structures that can be more directly associated with concurrent disturbances in IMF and solar wind velocity, while the red is used for the structure mentioned in the previous paragraph where that is not the case.
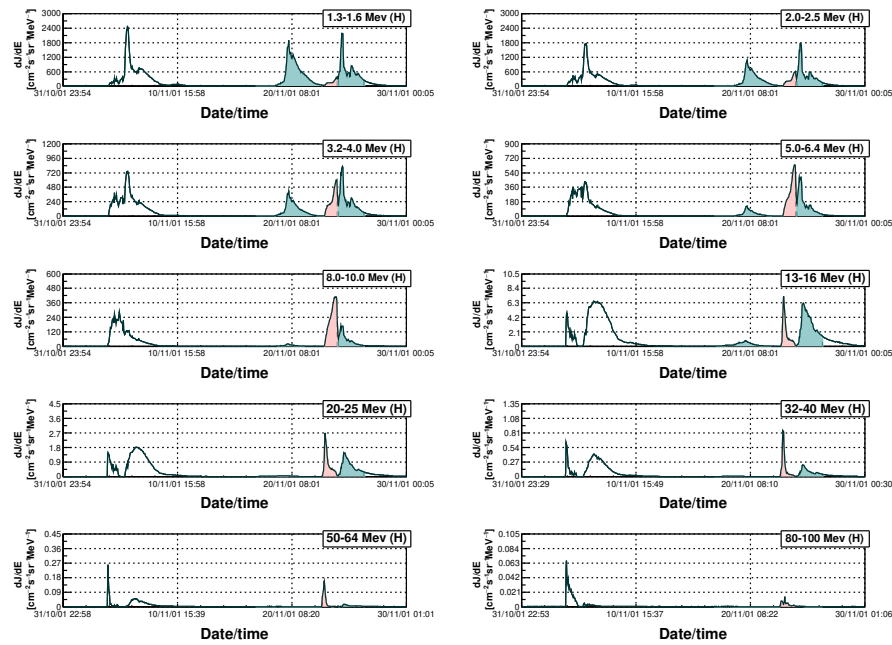
Figure 2. Energetic proton flux in ten selected SOHO/ERNE energy channels for the November 2001 event. The two cyan areas on each graph represent the measured flux during the passage of two ICMEs, while the red area between them represents the measured flux during a non-ICME-related structure.

The obtained values were used to form event-integrated fluence spectra. These spectra, calculated for the three proton flux enhancements occurring in the second half of November 2001, are shown in Fig. 3.
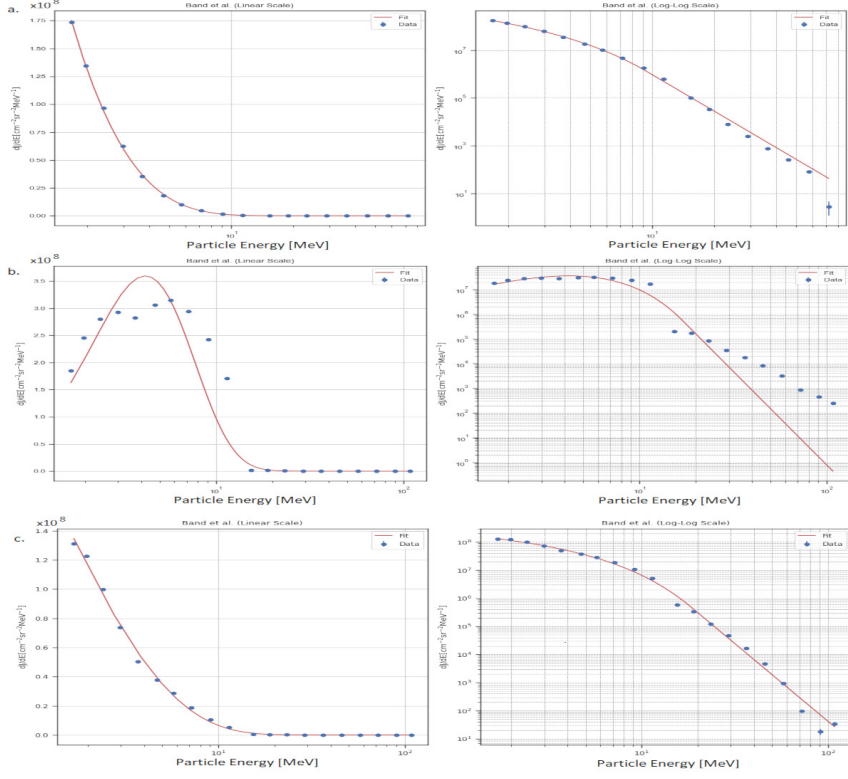
Figure 3. Event-integrated fluence spectra for three analyzed events, presented on a linear scale (left) and a log–log scale (right): (a) ICME on 17 November 2001, (b) SEP event on 22 November 2001, and (c) ICME on 24 November 2001. The red line represents the fit using the Band function.

To characterize the observed flux enhancements, event-integrated fluence spectra were fitted with a function based on the model proposed in (Band et al., 1993), which takes the form of a double power law:

$$\frac{dJ}{dE} = \begin{cases} AE^{\alpha} \exp\left(-\frac{E}{E_B}\right) & E \leq (\alpha - \beta)E_B, \\ AE^{\beta}\left[(\alpha - \beta)E_B\right]^{\alpha - \beta} \exp(\beta - \alpha) & E > (\alpha - \beta)E_B, \end{cases} \quad (1)$$

Here, E represents the particle energy, E_B is the "knee" energy, α is the power-law index characterizing the low-energy part of the spectrum, β is the power-law index characterizing the high-energy part of the fluence spectrum, and A is the spectral coefficient. A more detailed explanation of the procedure is provided in (Savić et al., 2024).

This model effectively describes the spectra of energetic particles accelerated by shocks, whether their origin is solar or due to local acceleration (both phenomena described in more detail in (Desai & Giacalone, 2016)). With this in mind, analyzing the spectra presented in Fig. 3, we observe that the events on 17 November and 24 November, which can be directly associated with the passage of concurrent ICMEs and related disturbances in the WIND data, are well modeled by the Band model. In contrast, the event on 22 November, which shows no observable disturbance in the WIND data, is poorly modeled. This discrepancy suggests that the origin of the flux enhancement on 22 November may not be attributed to shock acceleration.

Additional insights may be gained from the profiles shown in Fig. 4, which further highlight the differences in energy dependence between the observed structures in the energetic proton flux.
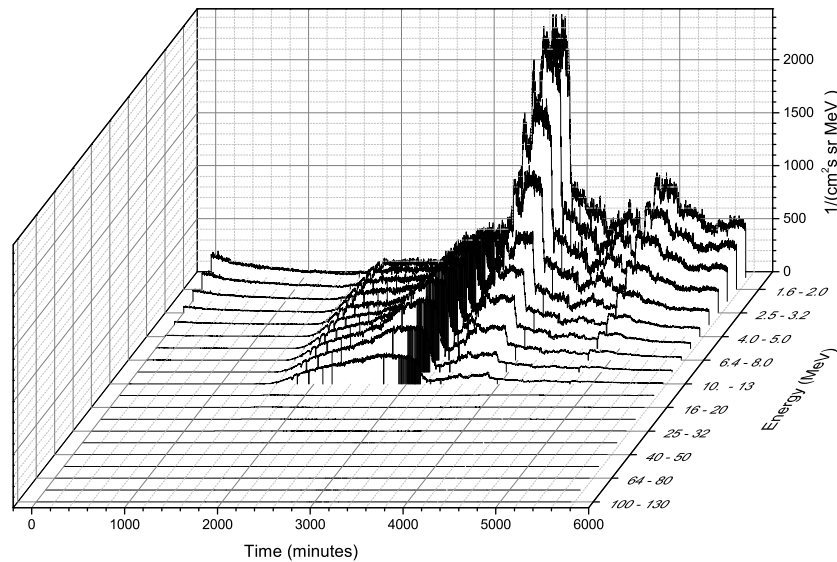
Figure 4. Energetic proton flux in various SOHO/ERNE energy channels during the time interval of 22–25 November 2001.

The analysis of fluence spectra can only indicate that the 22 November event cannot be clearly attributed to the passage of an ICME and shock acceleration, but does not provide a straightforward explanation for the origin or the mechanism responsible for the observed proton flux enhancement. Furthermore, sim-

ilar enhancements of unclear origin have been observed preceding or following other ICME-related SEP events, highlighting the need for additional systematic investigations in the future to better understand their nature.

4. Conclusion

To analyze the nature and impact of CMEs/ICMEs on the near-Earth environment, time series data from twenty different energy channels of proton flux measured by the SOHO/ERNE detector at Lagrange point L1 were used. WIND IMF and solar wind velocity data were used to precisely determine the times of ICME shocks and interactions. Based on this, SOHO/ERNE proton flux time series were integrated to obtain event-integrated fluence spectra. These spectra, corresponding to three apparently separate events, were modeled using the Band function. The two events where proton flux enhancement could be more directly associated with the passage of ICMEs were well modeled, whereas the event for which no concurrent disturbances in the IMF or CME velocity were observed did not fit the model as well. This suggests that the particle acceleration leading to the observed enhancement in this event cannot easily be attributed to interaction with an ICME shock, and alternative sources should be considered. Moreover, numerous similar enhancements observed in the SOHO/ERNE proton flux time series show the need for a more detailed systematic investigation.

References

Band, D., Matteson, J., Ford, L., et al., BATSE Observations of Gamma-Ray Burst Spectra. I. Spectral Diversity. 1993, *Astrophysical Journal*, **413**, 281, DOI:10.1086/172995

Belov, A., Shlyk, N., Abunina, M., et al., Solar Energetic Particle Events and Forbush Decreases Driven by the Same Solar Sources. 2022, *Universe*, **8**, DOI:10.3390/universe8080403

CDAW. 2024, LASCO CME CATALOG and Major SEP Event List, https://cdaw.gsfc.nasa.gov/, last accessed 10 November 2024

Desai, M. & Giacalone, J., Large gradual solar energetic particle events. 2016, *Living Reviews in Solar Physics*, **13**, 3, DOI:10.1007/s41116-016-0002-5

Falkenberg, T. V., Vennerstrom, S., Brain, D. A., Delory, G., & Taktakishvili, A., Multipoint observations of coronal mass ejection and solar energetic particle events on Mars and Earth during November 2001. 2011, *Journal of Geophysical Research: Space Physics*, **116**, DOI:10.1029/2010JA016279

Gopalswamy, N., Yashiro, S., Michalek, G., et al., A Catalog of Halo Coronal Mass Ejections from SOHO. 2010, *Sun and Geosphere*, **5**, 7

Kataoka, R., Sato, T., Miyake, S., Shiota, D., & Kubo, Y., Radiation Dose Nowcast for the Ground Level Enhancement on 10–11 September 2017. 2018, *Space Weather*, **16**, 917, DOI:10.1029/2018SW001874

King, J. H. & Papitashvili, N. E., Solar wind spatial scales in and comparisons of hourly Wind and ACE plasma and magnetic field data. 2005, *Journal of Geophysical Research: Space Physics*, **110**, DOI:10.1029/2004JA010649

Kolarski, A., Veselinović, N., Srećković, V. A., et al., Impacts of Extreme Space Weather Events on September 6th, 2017 on Ionosphere and Primary Cosmic Rays. 2023, *Remote Sensing*, **15**, DOI:10.3390/rs15051403

Rawat, R., Alex, S., & Lakhina, G. S., Low latitude geomagnetic signatures following two major solar energetic particle events at different phases of solar cycle-23. 2006, in *Proceedings of the ILWS Workshop*, ed. N. Gopalswamy & A. Bhattacharyya, 253

Reames, D. V., The Two Sources of Solar Energetic Particles. 2013, *Space Science Reviews*, **175**, 53, DOI:10.1007/s11214-013-9958-9

Richardson, I. & Cane, H. 2024, Near-Earth Interplanetary Coronal Mass Ejections Since January 1996, https://doi.org/10.7910/DVN/C2MHTH, last accessed 10 November 2024

Savić, M., Veselinović, N., Maričić, D., et al., Further Study of the Relationship between Transient Effects in Energetic Proton and Cosmic Ray Fluxes Induced by Coronal Mass Ejections. 2024, *Universe*, **10**, DOI:10.3390/universe10070283

Torsti, J., Valtonen, E., Lumme, M., et al., Energetic particle experiment ERNE. 1995, *Solar Physics*, **162**, 505, DOI:10.1007/BF00733438

Waterfall, C. O. G., Dalla, S., Raukunen, O., et al., High Energy Solar Particle Events and Their Relationship to Associated Flare, CME and GLE Parameters. 2023, *Space Weather*, **21**, e2022SW003334, DOI:10.1029/2022SW003334, e2022SW003334 2022SW003334

On the Stark broadening of O I spectral lines: comparison with experiments

M.S. Dimitrijević[1,2] , **F. Iacob**[3]

and S. Sahal-Bréchot[2]

[1] *Astronomical Observatory, Volgina 7, 11060 Belgrade, Serbia (E-mail:
mdimitrijevic@aob.rs)*

[2] *Sorbonne Université, Observatoire de Paris, Université PSL, CNRS, LUX,
F-92190, Meudon, France*

[3] *Faculty of Physics, West University of Timişoara, 300223 Bulevardul Vasile
Parvan 4, Timişoara, Romania*

Abstract. Stark broadening parameters, line widths, and shifts have been calculated for spectral lines within the neutral oxygen spectrum for experimental conditions of published experiments to compare experiments with results of the semiclassical perturbation method. The obtained data are of particular interest in astrophysics, for instance, for the investigation of stellar spectra but also for laboratory plasma diagnostics and plasma spectra containing lines of neutral oxygen.

Key words: Stark broadening – O I – spectral lines – line profiles

1. Introduction

Data on spectral line widths and shifts broadened by fluctuating electric microfields of surrounding charged particles (Stark broadening) are useful for different topics in astrophysics (see for example Popović et al., 2001), laboratory, (Blagojević et al., 1999), fusion (Iglesias et al., 1997), and laser-produced plasma research (Sorge et al., 2000), plasma in technology (Dimitrijević & Sahal-Bréchot, 2014), laser design and development, (Csillag & Dimitrijević, 2004) etc.

Such data are particularly needed in astrophysics, for example for radiative transfer calculations, abundance determinations, and investigation, stellar spectra analysis, modelling, and synthesis, etc. (see for example Dimitrijević & Christova, 2021). They are especially needed for white dwarfs and hot subdwarfs, e.g., for DO (Dimitrijević et al., 2018), DB (Majlinger et al., 2017, 2018, 2020), DA (Majlinger et al., 2017, 2020) dwarfs and for hot subdwarfs (Hamdi et al., 2017; Chougule et al., 2020). Stark broadening data may be interesting for A and late B type stars (Majlinger et al., 2017, 2020).

Our objective here is to calculate using the semiclassical perturbation method (Sahal-Bréchot, 1969a,b; Sahal-Bréchot, Dimitrijević, & Ben Nessib, 2014), Stark widths and shifts of neutral oxygen spectral lines for plasma conditions corresponding to experimental data from the literature and to compare the obtained results with experiments of Jung (1963); Wiese & Murphy (1963); Morris & Garrison (1969); Miller & Bengtson (1970); Assous (1970); Goly et al. (1983); Goly & Weniger (1987); Sohns & Kock (1992); Mijatović et al. (1995); Gerhard et al. (2014) and Burger & Hermann (2016), to check mutually experimental data and the semiclassical perturbation theory.

2. Theory

We performed a calculation of the Stark broadening parameters of O I spectral lines within the frame of the impact semiclassical perturbation theory (Sahal-Bréchot, 1969a,b; Sahal-Bréchot, Dimitrijević, & Ben Nessib, 2014). Since it has been discussed in detail on many occasions in the references cited above, just basic formulas will be given here. The full width at half maximum (FWHM - W) and shift (d) of an isolated spectral line are given in the case of non-hydrogenic neutral atoms as:

$$W \;=\; N \int v f(v) dv \left(\sum_{i' \neq i} \sigma_{ii'}(v) + \sum_{f' \neq f} \sigma_{ff'}(v) + \sigma_{el} \right)$$

$$d \;=\; N \int v f(v) dv \int_{R_3}^{R_D} 2\pi\rho d\rho \sin(2\varphi_p). \tag{1}$$

where i and f denote the initial and final level of the corresponding transition; i' and f' are perturbing levels; N perturber density; v perturber velocity, and $f(v)$ is the Maxwellian distribution of electron velocities. The inelastic cross sections $\sigma_{kk'}(v)$, $k = i, f$ are presented here by an integration of the transition probability $P_{kk'}(\rho, v)$, over the impact parameter ρ as:

$$\sum_{k' \neq k} \sigma_{kk'}(v) = \frac{1}{2}\pi R_1^2 + \int_{R_1}^{R_D} 2\pi\rho d\rho \sum_{k' \neq k} P_{kk'}(\rho, v). \tag{2}$$

The cross section for elastic collisions is given as:

$$\sigma_{el} = 2\pi R_2^2 + \int_{R_2}^{R_D} 2\pi\rho d\rho \sin^2 \delta,$$

$$\delta = (\varphi_p^2 + \varphi_q^2)^{\frac{1}{2}}. \tag{3}$$

Here, δ denotes the phase shift with components φ_p (r^{-4}) and φ_q (r^{-3}), describing contributions due to polarization and quadrupole potentials, respectively. The method of symmetrization and calculation of cut-off parameters R_1, R_2, R_3, and the Debye cut-off R_D is explained in Sahal-Bréchot (1969b).

3. Results and discussion

To calculate the Stark broadening parameters of O I spectral lines, full width at half intensity maximum (FWHM - W) and shift (d) we used the semiclassical perturbation method (Sahal-Bréchot, 1969a,b; Sahal-Bréchot, Dimitrijević, & Ben Nessib, 2014). For the electron density and temperature, we used the values for considered experiments Jung (1963); Wiese & Murphy (1963); Morris & Garrison (1969); Miller & Bengtson (1970); Assous (1970); Goly et al. (1983); Goly & Weniger (1987); Sohns & Kock (1992); Mijatović et al. (1995); Gerhard et al. (2014) and Burger & Hermann (2016). The needed set of atomic energy levels for neutral oxygen has been taken from Moore (1993). Oscillator strengths have been calculated using the method of Bates & Damgaard (1949) and the tables of Oertel & Shomo (1968).

The results obtained for Stark Full Width at Half intensity Maximum (FWHM - W) have been compared with experimental data of Jung (1963); Wiese & Murphy (1963); Morris & Garrison (1969); Miller & Bengtson (1970); Assous (1970); Goly et al. (1983); Goly & Weniger (1987); Sohns & Kock (1992); Mijatović et al. (1995); Gerhard et al. (2014) and Burger & Hermann (2016) in Table 1 and for shift in Table 2.

We can divide the obtained ratios of experimental and theoretical widths in Table 1 into three groups. The first one with ratios of experimental and theoretical widths from 1.3 up to 1.6, the second from 1.8 up to 2.2, and the third from 0.63 up to 1.22. In the first group are values from Wiese & Murphy (1963); Goly et al. (1983); Goly & Weniger (1987) and Mijatović et al. (1995). One can see that they all have estimated accuracies A, B+, and B, according to critically evaluation in Konjevic & Roberts (1976); Konjević & Wiese (1990); Konjević et al. (2002); Djurović et al. (2023). In the second group are values from Miller & Bengtson (1970); Sohns & Kock (1992); Burger & Hermann (2016). In the mentioned critical reviews, their accuracy is denoted as C+ and D. In the third group are data from Refs. Jung (1963); Morris & Garrison (1969); Assous (1970) and Gerhard et al. (2014) and accuracies are estimated as C+, C, and D. The consistency, that all experiments evaluated as best are within the same group confirms that the evaluation of accuracy in the above mentioned critical reviews is good. The difference in experimental and theoretical values is due to the influence of ion broadening. For the spectral lines in the first group, with the best accuracy, the validity condition of impact approximation is not well satisfied, and the impact semiclassical perturbation theory is not valid for

Table 1. In this Table, present calculations of Stark widths W_{th} (FWHM) are compared with experimental values (W_{exp}. References for experimental values are: 1 - Jung (1963); 2 - Wiese & Murphy (1963); 3 - Morris & Garrison (1969); 4 - Miller & Bengtson (1970); 5 - Assous (1970); 6 - Goly et al. (1983); 7 - Goly & Weniger (1987); 8 - Sohns & Kock (1992); 9 - Mijatović et al. (1995); 10 - Gerhard et al. (2014); 11 - Burger & Hermann (2016). Estimated accuracy is from Konjevic & Roberts (1976); Konjević & Wiese (1990); Konjević et al. (2002); Djurović et al. (2023). For accuracy, the letter code, as in the above-mentioned references (see for example Djurović et al. (2023)), is used: A = uncertainties with 15%; B+ = with 23%; B = with 30%;C+ = with 40%; C = with 50%; D uncertainties larger than 50%.

Transition	λ [Å]	T [K]	N $[10^{17}\,\mathrm{cm}^{-3}]$	W_{exp}	W_{th}	$\frac{W_{exp}}{W_{th}}$	Acc.	Ref.
$2p^4\ ^3P$-$(^4S^o)3s^3S^o$	1303.5	13600	1.32	0.01848	0.0175	1.06	D	3
$2p^4\ ^3P_2$-$(^4S^o)3s^3S_1^o$	1302.17	12500	1	0.0233	0.013	1.79	C+	8
$2p^4\ ^3P_1$-$(^4S^o)3s^3S_1^o$	1304.86	12500	1	0.0233	0.013	1.79	C+	8
$2p^4\ ^3P_0$-$(^4S^o)3s^3S_1^o$	1306.03	12500	1	0.0233	0.013	1.79	C+	8
$3s\ ^5S_2^o$-$(^4S^o)3p^5P_3$	7771.94	11000	1	1.05	0.544	1.93	C+	11
		11200	1	0.64	0.547	1.17	C+	10
$3s\ ^5S_2^o$-$(^4S^o)3p^5P_2$	7774.17	11000	1	1.05	0.544	1.93	C+	11
$3s\ ^5S_2^o$-$(^4S^o)3p^5P_1$	7775.39	11000	1	1.05	0.544	1.93	C+	11
$3s\ ^5S^o$-$(^4S^o)4p^5P$	3947.3	11580	0.397	0.62	0.416	1.49	B+	7
		12080	0.57	0.83	0.606	1.37	B	2
		12500	0.784	1.20	0.842	1.43	B+	7
		13570	0.441	0.64	0.486	1.32	B	7
$3s\ ^3S^o$-$(^4S^o)4p^3P$	4368.3	10100	0.191	0.39	0.249	1.57	B	6
		10600	0.240	0.51	0.317	1.61	A	9
		10960	0.312	0.67	0.416	1.61	A	9
		11580	0.397	0.78	0.539	1.45	B+	7
		11800	0.45	0.59	0.614	0.96	C	1
		12080	0.57	1.08	0.784	1.38	B	2
		12500	0.784	1.44	1.09	1.32	B+	7
		12700	0.713	1.37	0.996	1.38	B	6
		13800	1.11	1.36	1.59	0.86	C	1
$3s\ ^3S^o$-$(^4S^o)5p^3P$	3692.4	12080	0.57	2.72	1.81	1.50	C	2
$3p\ ^5P$-$(^4S^o)4d^5D^o$	6157.3	11000	1	37.2	16.7	2.23	D	4
		11800	0.45	5.05	8.05	0.63	D	1
		13800	1.11	12.2	18.4	0.66	D	1
$4s\ ^5S^o$-$(^4S^o)4p^5P$	27645.2	11200	0.291	22	20.5	1.07	C	5
$4p\ ^5P$-$(^4S^o)4d^5D^o$	26520.4	11200	0.291	107.5	108	0.995	C	5
$4p\ ^3P$-$(^4S^o)4d^3D^o$	30973.0	11200	0.291	185.0	152	1.22	C	5

the ion contribution, so a theory of unified type or a quasistatic method should be used for ions. To approximately estimate this influence, we calculated line widths due to collisions with Ar II ions (working gas in this experiment) for plasma conditions corresponding to the experiment in Mijatović et al. (1995), with the best accuracy, labeled as A, but for transitions $3s\ ^3S^o$-$(^4S^o)3p^5P$ and $3s\ ^5S^o$-$(^4S^o)3p^5P$. We obtained that the widths due to electron impacts should be increased by 30.5% and 29.0% respectively. If we increase the line widths of $3s\ ^3S^o$-$(^4S^o)4p^5P$ for 30%, the ratio of experimental and theoretical values will

Table 2. Same as in Table 1, but for shift d.

Transition	λ [Å]	T [K]	N $[10^{17}\,\mathrm{cm}^{-3}]$	d_{exp}	d_{th}	$\frac{d_{exp}}{d_{th}}$	Acc.	Ref.
3s ^{5}S^o-(^{4}S^o)4p^{5}P	3947.3	11580	0.397	0.05	0.0308	1.62	D	7
		12080	0.57	-0.13	0.0457	-2.84	B	2
		12500	0.784	0.09	0.0645	1.40	D	7
3s ^{5}S$^o_2$-(^{4}S^o)3p^{5}P$_3$	7771.94	11000	1	0.15	0.160	0.94	C	11
		11200	1	0.14	0.159	0.88	C+	10
3s ^{5}S$^o_2$-(^{4}S^o)3p^{5}P$_2$	7774.17	11000	1	0.15	0.160	0.94	C	11
3s ^{5}S$^o_2$-(^{4}S^o)3p^{5}P$_1$	7775.39	11000	1	0.15	0.160	0.94	C	11
3s ^{3}S^o-(^{4}S^o)4p^{3}P	4368.3	10600	0.240	0.10	0.113	0.88	A	9
		10960	0.312	0.13	0.146	0.89	A	9
		11580	0.397	0.12	0.184	0.65	C+	7
		11800	0.45	0.16	0.208	0.77	C	1
		12080	0.57	0.20	0.263	0.76	B	2
		12500	0.784	0.27	0.359	0.75	C+	7
		13800	1.11	0.36	0.528	0.68	C	1
3p ^{5}P-(^{4}S^o)4d^{5}D^o	6157.3	11800	0.45	4.3	2.88	1.49	D	1
		13800	1.11	9.9	6.08	1.63	D	1
3s ^{3}S^o-(^{4}S^o)5p^{3}P	3692.4	12080	0.57	0.18	-0.187	-0.96	C	2
4p ^{5}P-(^{4}S^o)4d^{5}D^o	26520.4	11200	0.291	42.9	37.7	1.14	C	5

be 1.24 instead of 1.61, which is within the errors of experiment and theory. So we can conclude that we recommend the experimental values from the first group and that they are confirmed by our calculation and analysis.

If we look at Table 2, where the experimental and theoretical results for shift are presented, we can notice that shift values are much smaller than the corresponding widths. Namely, as a difference with the width calculations where all contributions are positive, in the case of the shift we have positive and negative contributions, and if there is their mutual cancellation, shifts are smaller. If they are much smaller than the corresponding widths, like in the present case, the accuracy of theoretical calculations is smaller and also, the experiment has more difficulties. The majority of the shifts in Table 2 have values of ratios of experimental and theoretical shifts between 0.68 and 0.95. Only for 3947.3 Å multiplet in Goly & Weniger (1987), 6157.3 Å multiplet in, Jung (1963) and 26520.4 multiplet in Assous (1970) shift ratios have values within the range 1.14 - 1.63. An exception are the results in Wiese & Murphy (1963), who obtained the shift with a different sign from theoretical ones. In the case of 3s ^{5}S^o-(^{4}S^o)4p^{5}P transition, in the experiment of Goly & Weniger (1987) the shift is positive as in the present calculations, but its accuracy is denoted as "D". Since the shift is much smaller than width the new experiments are needed for this transition. The sign of the shift, different from the theoretical one is in Ref. Wiese & Murphy (1963), also for the transition 3s ^{3}S^o-(^{4}S^o)5p^{3}P. However in this case, due to close perturbing atomic energy level 4d^{3}D, which is lower than the level 5p^{3}P, the shift must be negative as it is obtained theoretically, while in the experiment, it is positive. In this case, also, new measurements would be of interest.

4. Conclusion

The Stark broadening parameters, including spectral line FWHM and shifts, have been calculated for O I lines reported in the literature using the impact semiclassical perturbation theory (Sahal-Bréchot, 1969a,b; Sahal-Bréchot et al., 2014). The obtained results were compared with the experimental data, and the corresponding agreement was discussed to further verify the experimental data considered. These results were compared with the experimental data, and the level of agreement was analyzed to further validate the experimental conclusions. Strong broadening data for neutral oxygen spectral lines are valuable for stellar spectrum analysis and synthesis, stellar atmosphere modeling, laboratory plasma diagnostics, and various plasma technological applications.

References

Assous, R., Elargissement et déplacement par effet Stark de raies de l'atome neutre d'oxygène. 1970, *Journal of Quantitiative Spectroscopy and Radiative Transfer*, **10**, 975, `DOI:10.1016/0022-4073(70)90118-4`

Bates, D. R. & Damgaard, A., The Calculation of the Absolute Strengths of Spectral Lines. 1949, *Philosophical Transactions of the Royal Society of London Series A*, **242**, 101, `DOI:10.1098/rsta.1949.0006`

Blagojević, B., Popović, M. V., Konjević, & Dimitrijević, M. S., Stark Broadening Parameters of Analogous Spectral Lines Along the Lithium and Beryllium Isoelectronic Sequences. 1999, *Journal of Quantitiative Spectroscopy and Radiative Transfer*, **61**, 361, `DOI:10.1016/S0022-4073(98)00002-8`

Burger, M. & Hermann, J., Stark broadening measurements in plasmas produced by laser ablation of hydrogen containing compounds. 2016, *Spectrochimica Acta - Part B: Atomic Spectroscopy*, **122**, 118, `DOI:10.1016/j.sab.2016.06.005`

Chougule, A., Przybilla, N., Dimitrijević, M. S., & Schaffenroth, V., The impact of improved Stark-broadening widths on the modeling of double-ionized chromium lines in hot stars. 2020, *Contributions of the Astronomical Observatory Skalnate Pleso*, **50**, 139, `DOI:10.31577/caosp.2020.50.1.139`

Csillag, L. & Dimitrijević, M. S., On the Stark broadening of the 537.8 nm and 441.6 nm Cd^+ lines excited in a hollow cathode laser discharge. 2004, *Applied Physics B: Lasers and Optics*, **78**, 221, `DOI:10.1007/s00340-003-1368-3`

Dimitrijević, M. & Sahal-Bréchot, S., On the Application of Stark Broadening Data Determined with a Semiclassical Perturbation Approach. 2014, *Atoms*, **2**, 357, `DOI:10.3390/atoms2030357`

Dimitrijević, M. S. & Christova, M., Stark widths of Lu II spectral lines. 2021, *European Physical Journal D*, **75**, 172, DOI:10.1140/epjd/s10053-021-00179-4

Dimitrijević, M. S., Simić, Z., Kovačević, A., & Sahal-Bréchot, S., The influence of Stark broadening on Xe VIII spectral lines in DO white dwarfs. 2018, *Astronomical and Astrophysical Transactions*, **30**, 331

Djurović, S., Blagojević, B., & Konjević, N., Experimental and Semiclassical Stark Widths and Shifts for Spectral Lines of Neutral and Ionized Atoms (A Critical Review of Experimental and Semiclassical Data for the Period 2008 Through 2020). 2023, *Journal of Physical and Chemical Reference Data*, **52**, 031503, DOI:10.1063/5.0147933

Gerhard, C., Hermann, J., Mercadier, L., et al., Quantitative analyses of glass via laser-induced breakdown spectroscopy in argon. 2014, *Spectrochimica Acta - Part B: Atomic Spectroscopy*, **101**, 32, DOI:10.1016/j.sab.2014.07.014

Goly, A., Rakotoarijimy, D., & Weniger, S., Experimental Stark parameters for some lines of neutral carbon, oxygen, and sulfur. 1983, *Journal of Quantitiative Spectroscopy and Radiative Transfer*, **30**, 417, DOI:10.1016/0022-4073(83)90105-X

Goly, A. & Weniger, S., Widths and shifts of some plasma-broadened oxygen and carbon multiplets. 1987, *Journal of Quantitiative Spectroscopy and Radiative Transfer*, **38**, 225, DOI:10.1016/0022-4073(87)90090-2

Hamdi, R., Ben Nessib, N., Sahal Bréchot, S., & Dimitrijević, M. S., Stark Widths of Ar II Spectral Lines in the Atmospheres of Subdwarf B Stars. 2017, *Atoms*, **5**, 26, DOI:10.3390/atoms5030026

Iglesias, E., Griem, H., Welch, B., & Weaver, J., UV Line Profiles of B IV from a 10-Ps KrF-Laser-Produced Plasma. 1997, *Astrophysics and Space Science*, **256**, 327, DOI:10.1023/A:1001140202851

Jung, M., Verbreiterung von Spektrallinien des neutralen Sauerstoffs durch Mikrofelder. Mit 5 Textabbildungen. 1963, *Zeitschrift fuer Astrophysik*, **58**, 93

Konjević, N., Lesage, A., Fuhr, J. R., & Wiese, W. L., Experimental Stark Widths and Shifts for Spectral Lines of Neutral and Ionized Atoms (A Critical Review of Selected Data for the Period 1989 Through 2000). 2002, *Journal of Physical and Chemical Reference Data*, **31**, 819, DOI:10.1063/1.1486456

Konjevic, N. & Roberts, J. R., A critical review of the Stark widths and shifts of spectral lines from non-hydrogenic atoms. 1976, *Journal of Physical and Chemical Reference Data*, **5**, 209, DOI:10.1063/1.555532

Konjević, N. & Wiese, W. L., Experimental Stark widths and shifts for spectral lines of neutral and ionized atoms. 1990, *Journal of Physical and Chemical Reference Data*, **19**, 1307, DOI:10.1063/1.555847

Majlinger, Z., Dimitrijevic, M. S., & Simic, Z., On the Stark broadening of Co II spectral lines. 2018, *Astronomical and Astrophysical Transactions*, **30**, 323

Majlinger, Z., Dimitrijević, M. S., & Srećković, V. A., Stark broadening of Co II spectral lines in hot stars and white dwarf spectra. 2020, *Monthly Notices of the RAS*, **496**, 5584, DOI:10.1093/mnras/staa1947

Majlinger, Z., Simić, Z., & Dimitrijević, M. S., Stark broadening of Zr IV spectral lines in the atmospheres of chemically peculiar stars. 2017, *Monthly Notices of the RAS*, **470**, 1911, `DOI:10.1093/mnras/stx1321`

Mijatović, Z., Konjević, N., Kobilarov, R., & Djurović, S., Search for ion dynamics effects on the shift and width of plasma-broadened C I and O I spectral lines. 1995, *Physical Review E*, **51**, 613, `DOI:10.1103/PhysRevE.51.613`

Miller, M. H. & Bengtson, R. D., Measured Stark Widths and Shifts for Neutral Atomic Lines. 1970, *Physical Review A: General Physics*, **1**, 983, `DOI:10.1103/PhysRevA.1.983`

Moore, C. E. 1993, *Tables of Spectra of Hydrogen, Carbon, Nitrogen, and Oxygen Atoms and Ions*

Morris, J. C. & Garrison, R. L., Measurement of the Radiation Emitted f Values and Stark Half-Widths for the Strong Vacuum Ultraviolet Lines of O I and N I. 1969, *Physical Review*, **188**, 112, `DOI:10.1103/PhysRev.188.112`

Oertel, G. K. & Shomo, L. P., Tables for the Calculation of Radial Multipole Matrix Elements by the Coulomb Approximation. 1968, *Astrophys. J., Suppl. Ser.*, **16**, 175, `DOI:10.1086/190173`

Popović, L. Č., Simić, S., Milovanović, N., & Dimitrijević, M. S., Stark Broadening Effect in Stellar Atmospheres: Nd II Lines. 2001, *Astrophys. J., Suppl. Ser.*, **135**, 109, `DOI:10.1086/321778`

Sahal-Bréchot, S., Impact Theory of the Broadening and Shift of Spectral Lines due to Electrons and Ions in a Plasma. 1969a, *Astronomy and Astrophysics*, **1**, 91

Sahal-Bréchot, S., Impact Theory of the Broadening and Shift of Spectral Lines due to Electrons and Ions in a Plasma (Continued). 1969b, *Astronomy and Astrophysics*, **2**, 322

Sahal-Bréchot, S., Dimitrijević, M., & Ben Nessib, N., Widths and Shifts of Isolated Lines of Neutral and Ionized Atoms Perturbed by Collisions With Electrons and Ions: An Outline of the Semiclassical Perturbation (SCP) Method and of the Approximations Used for the Calculations. 2014, *Atoms*, **2**, 225, `DOI:10.3390/atoms2020225`

Sohns, E. & Kock, M., Plasma diagnostics based on self-reversed lines. II. Application to nitrogen, carbon and oxygen arc measurements in the vacuum ultraviolet. 1992, *Journal of Quantitiative Spectroscopy and Radiative Transfer*, **47**, 335, `DOI:10.1016/0022-4073(92)90035-3`

Sorge, S., Wierling, A., Röpke, G., et al., Diagnostics of a laser-induced dense plasma by hydrogen-like carbon spectra. 2000, *Journal of Physics B Atomic Molecular Physics*, **33**, 2983, `DOI:10.1088/0953-4075/33/16/304`

Wiese, W. L. & Murphy, P. W., Shifts and Widths of Some Stark-Broadened Oxygen Lines in an Arc Plasma. 1963, *Physical Review*, **131**, 2108, `DOI:10.1103/PhysRev.131.2108`